DESIGN AND EVALUATION OF HIGH POWER DENSITY BRUSHLESS DC PERMANENT MAGNET MACHINES

MD NAZRI BIN OTHMAN

Thesis submitted to the University of Nottingham
for the degree of Doctor of Philosophy

Department of Electrical and Electronic Engineering
SEPTEMBER 2010

Abstract

Permanent Magnet brushless DC motors are now competing with many other types of motors in the world industries application. However, for low and medium power applications, brushless DC motors are often the main option due to its recognized advantage such as having no commutator, more efficient, need less maintenance, smaller in size and can operate at higher speeds than conventional motors. The overall objective of this project is to produce an improved prototype BLDC motor with concentrated winding concept for an aircraft actuator application. Specifically, the aim is to extract the maximum power density and torque per kilograms by utilizing high switching frequencies, high pole numbers and minimizing magnetic material content.

In this work, the research has focused on developing a procedure to design the BLDC motor by selecting several parameters and analysing their effects on the overall performance. Therefore, this research involved software and hardware methods which are broken down into field and circuit modeling, calculation of basic dimensions, magnetic circuit calculations, stator slot design, winding design, performance and loss calculation and lastly prototyping. Magnet software for finite-element method (FEM) analysis and analysis programs based on standard software are used to optimize the overall performances. The proposed methods are verified by actual experimental result on the developed prototype. The performance of the prototyped machine is evaluated by using a high speed 150kw, 20,000 rpm test rig and data capturing equipment.

Acknowledgement

I wish to express my sincere gratitude to my supervisor, Dr. Chris Gerada, for his guidance, encouragement and support during my graduate studies. His impressive knowledge, technical skills and human qualities have been a source of inspiration and a model for me to follow.

I'm also grateful to my previous supervisor, Professor Dr Keith Bradley, for his help, guidance and support during my studies at University of Nottingham. I'm thankful to be a member of the Power Electronic Machine and Control (PEMC) Group which is one of the leading research groups in the UK in the field of power electronics, machine design and motor drives. It has been memorable experience, both professionally and personally.

I would also like to acknowledge PEMC students and staffs for providing an enjoyable educational atmosphere. Especially, I would like to thank to Liliana, Fidy, Sudarat and Mustapha for endless discussions, all the technicians especially Colin, Kevin and Mat for sharing me their rich practical experience and all others who made my work and my stay in PEMC more valuable.

With much love, I thank my parents for their loving care and their unconditional support. This dissertation is their accomplishment as much as it is mine. Most importantly, I want to thank my wife, Norhayati and all my children, Kakak, Kakcik, Hud and Dhia for your love, patience and support during all these years. Without your understanding and devotion, this work presented will not be possible. Finally, I would like to acknowledge Universiti Teknikal Malaysia Melaka and Public Service Department (PSD) of Malaysia for generously sponsor my study.

Contents

List of Tables

List of Figures

Acronym and Symbol

AC	Alternative Current
BLAC	Brushless AC
BLDC	Brushless DC
CFD	Computational fluid dynamic
DC	Direct Current
EDM	Electrical Discharge Machining
EMF	Electromotive Force
FE	Finite-element
FEA	Finite-element analysis
FEM	Finite-element method
MEA	More Electric Aircraft
MMF	Magnetomotive Force
NdFeB	Neodymium-iron-boron
PEMC	Power Electronics, Machines and Control
PBW	Power-by-wire
PM	Permanent Magnet
PMSM	Permanent Magnet Synchronous Motor
Q24P16	24 Slots 16 Poles Motor
Q24P20	24 Slots 20 Poles Motor
Q24P24	24 Slots 24 Poles Motor
$SmCo_2$	Samarium-Cobalt
THD	Total Harmonic Distortion

VSI	Voltage Source Inverter
A_m	The cross-sectional areas of the permanent magnet
A_{ag}	The cross-sectional areas of the air gap
A_{slcnr}	The area at the slot corner
A_{slot}	The slot area
A_{cu}	The conductor cross-sectional area in mm^2
B_r	Magnet remanent flux density
B_m	Magnet working flux density
d_{slot}	The tooth tip thickness
d_2	The dimension of the opposite side of the right triangle at tooth tip
e_t	The induced back EMF in one conductor
E_{ph}	The phase back EMF
EndWdg	End winding length of the conductor
F_{mag}	The centrifugal force of the magnets on the rotor
h_{slot}	The slot height
H_m	The magnetic field intensities of the permanent magnet
H_{ag}	The magnetic field intensities of the air gap
i_a	Phase currents in ampere, A
i_{sc}	The short circuit current
k_{dn}	The distribution factor
k_{pn}	The Pitch factor
k_w	The winding distribution
k_h	The hysteresis constant
l_m	The lengths of the magnetic paths in the permanent magnet

l_{ag}	The lengths of the magnetic paths in the air gap
m_{mag}	The mass of the magnet material
L_a	Self inductances of each phase in henry, H
L_{ab}	Mutual inductances of between phases in henry, H
L_{cu}	Total length of the stator winding
L_{mot}	The axial length of the stator core
Nturn	The number of conductor turns
Ph	The number of phases
P_{cu}	The copper loss
P_{iron}	The iron loss
P_h	The hysteresis loss
P_e	The eddy current loss
$P_{windage}$	The windage loss
$P_{bearing}$	The bearing loss
P_{mag}	The pressure of the magnets
P_{adh}	The peel strength of the adhesive
P_{res}	The residual pressure
N_{slot}	The number of slot
r_{mag}	The average radius of the magnets
r_m	The average radius of the magnets
R_a	Winding Resistances of each phase in ohm, Ω
R_{si}	The inner radius of the stator
R_{slo}	The outer radius of the stator
Str	The number of strand of the conductor

T_e	The electromagnetic torque
T_w	The tooth width
T_{sc}	The braking torque
V_a	Phase voltages on motor winding in volt, V
ν	The linear mechanical speed at the stator bore
ω_{rm}	Electrical angular speed
ω_{rm}	Mechanical angular speed
W_{slo}	The slot width at outer radius of slot area
W_{sli}	The slot width at inner radius of slot area
Z_{ph}	The total number of conductors per phase
Z_t	A number of conductor per tooth
β	The Steinmetz constant
ρ_m	The mass density of the magnet material,
σ	Winding conductor conductivity in $\frac{1}{\Omega.mm}$
μ_{rec}	Magnet recoil permeability
ϕ	The effective flux
ψ_a	Flux linkages of each phase in weber, Wb
ψ_{am}	Flux linked with each phase due to the permanent magnet
θ_{rm}	Mechanical rotor displacement
θ_{re}	Electrical rotor displacement

Chapter 1

Introduction

Brushless DC (BLDC) motors are now competing with many other types of motors in the world industries application. However, for low and medium power applications, brushless DC motors are often the main option. Brushless motors are generally recognized as being superior for a number of reasons. They have no commutator, are more efficient, need less maintenance, are smaller in size and can operate at higher speeds than conventional dc motors [1]. Due to its high efficiency, small size and price competitiveness, BLDC motors are now becoming important for military, aircraft, and automotive applications, and for portable instruments and communications equipment [1]. The small size reflects high torque output/kg and high power density which is significantly important to both markets.

Nowadays, electric motor manufacturers and researchers are continuously exploring methods for increasing the motor's efficiency which means producing more motor shaft power while using less input power. Motor efficiency improvements will save on energy costs, extend the operation time of battery-powered products and reduce the amount of heat which will increase reliability and can reduce the machine's scheduled maintenance costs [2]. Higher power efficiency also means lower internal power losses and greater power density since power loss defines temperature rise of the motor which is the ultimate performance limitation. Below are the lists of motor losses for any improvement consideration [3].

i. Copper winding (copper losses in the resistance of the stator coils)

ii. Coulomb friction (brushes, bearings and shaft seals, etc.)

iii. Viscous friction (bearing lubrication, certain materials damping characteristic as a function of speed)

iv. Hysteresis losses in magnetic materials

v. Eddy currents (losses in soft and hard magnetic materials related to caused by material type and thickness of eventual laminations)

vi. Windage (aerodynamic effects due to motor geometry and speed)

1.1 Research Objectives

The overall objective of this project is to theoretically and practically investigate an improved permanent magnet brushless motor with concentrated winding concept for an aircraft actuator application with the specific aim to extract the maximum power and torque density per kg. This can be achieved by utilising high switching frequencies, high pole numbers and minimising the amount of magnetic material used. The specific objectives are as follows:

1) To obtain the optimum design parameters to achieve low losses and high performance brushless motors.
2) To compare the torque producing capability of brushless DC and AC motors.
3) To investigate the practical implications of designing and constructing such machines through setting up and performing extensive testing.

1.2 Significance and Benefits of Research

This research will be of interest to those in the aircraft, automotive and manufacturing industries, particularly where actuator systems are used extensively. The direct beneficiaries of this research will be the aerospace industries and manufacturing industries especially in the automotive industries and machinery fields. This research is specifically dedicated for the usage of the actuator in the More Electric Aircraft (MEA) frame. The concept of a More Electric Aircraft (MEA) is the replacement of all hydraulic (oil) and pneumatic (air) actuators by local electrically driven actuators.

Work on the More Electric Aircraft began around the late 1970's. The ultimate objective is to replace all currently existing mechanical subsystems (hydraulic and pneumatic) by electrical systems. In today's commercial aircrafts the bulk of actuation functions is accomplished using hydraulics. The next logical step in the MEA advancement is to totally eliminate the central hydraulic systems. This can be accomplished by using power-by-wire (PBW). PBW actuation systems can be made far more fault tolerant than those depending on a central hydraulic supply. There are several advantages in implementing a More Electric Aircraft approach. Thus by removing the hydraulic packs, we would obtain the following benefits may be obtained

i. a reduced system weight
ii. less demanding maintenance
iii. improved efficiency

iv. less breakdown and jamming issues

v. cleaner and safer environment

From the above it can be concluded that having a lower overall aircraft weight, would inherently lead to less operating costs since there would be reduction in fuel consumption which as a result will reduce the environmental impact and greener solution.

1.3 Research Methodology

The proposed research consists of the following phases:

1) Phase one consists of a literature survey to determine the characteristics of BLDC motor and identify the main parameters and techniques that should be optimized in order to achieve high performance motor. A review of the potential of silicon carbide devices and of the supply converter topologies such as the matrix converter will also be carried out and liaison with research assistant who is developing a universal power electronic system
2) Phase two consists of the fundamental research into the BLDC motor which is broken down into field-based and circuit-based modeling, preliminary design, magnetic circuit calculations, stator slot design, winding design, and performance and loss calculation [8]. In this stage, two different approaches are used in predicting and analysing the finding through analytical and simulated models which are referred as mathematical algorithms and finite-element method (FEM) analysis respectively. Both general purpose analysis programs based on standard software for analytical model and Infolytica,

Magnet software for finite-element method (FEM) analysis will be used together to compare and optimize overall performance.

3) Phase three is aimed at the detailed design of stator slot and winding characteristics in obtaining the optimum concentrated winding that would give excellent performance of the motor. This will include the analysis of practical techniques to increase the slot fill factor.
4) Phase four is aimed at the development process for producing a prototype machine using the Electrical Discharge Machining (EDM) technology to produce stator and rotor assemblies together and to cut and magnetize the magnets.
5) Phase five is on evaluation of machine capability using the high speed 150kw, 20,000 rpm test rig and data capturing equipment available at the University of Nottingham. This experimental result will obviously be used to validate the finding in phase two.

1.4 Expected Results

The results of this research activity will provide a deeper understanding of the optimum relation between the concentrated winding and the shaft output power of a BLDC motor. A significant improvement in torque per kilograms and specific power density is expected. This research is also aimed to produce a prototype BLDC motor that will be used in conjunction with an integrated aircraft actuator. From the supervisor's experience, recent work in this area suggests that meeting the specification is achievable, but challenging.

1.5 Literature Research

A great deal of study has been devoted to having a simple winding structure and increasing the performance of the BLDC motor. The interest in concentrated windings is growing due to their simple structure which enables a cost effective manufacturing process [6]. Moreover, the concentrated winding machines have potentially more compact designs compared to the conventional machine designs with distributed windings, due to shorter end-windings and axial build [7].

The performances of the machines with concentrated windings may result higher than the performances of the traditional machines because of the minimization of both copper volume and Joule losses [6]. Such solution also will reduce the manufacturing costs and improve the output characteristics. The industrial development of these structures should increase in the near future and it will not be restricted only to low power applications.

However, BLDC machines with concentrated windings usually have a poor fundamental winding factor of typically around 0.833 [5]. According to Freddy Magnussen and Chandur Sadarangani, the winding factor is proportional to the electromagnetic torque [6]. An electrical machine with a low winding factor needs to compensate its lower torque with higher current or a greater number of turns, which both are inversely proportional to the winding factor. In comparison to an ideal machine with unity winding factor, which is found in distributed windings, the resistive losses will increase. For a comparison example, a machine with concentrated windings has to increase its current density percentage more than to a

machine equipped with the distributed winding in order to reach a similar required torque by assuming that the machines have equal slot fill factors, comparable magnetic design and that the end windings are neglected. Freddy noted that a machine with a winding factor of 0.866 will have 15.5 percent higher current density and 33.3 percent higher Joule losses compared to the distributed machine for the same torque [6]. In view of those drawbacks, few studies were carried in producing high winding factor and low Joule losses by selecting appropriate combinations of the pole and slot numbers [6-8].

Another problem of concentration winding machines is a relevant cogging torque. A study by J.Cros and P.Viarouge shows that it is possible to minimize the cogging torque without skewing the slots [9]. This increases the power density for the machine. Some coils can also be removed to maximize the winding coefficient of the fundamental component. The study is about comparing the cogging torque patterns of an original three-phase machine with 45 slots and 8 poles with a winding coefficient of the fundamental component equal to 0.99 with a machine with 6 concentrated coils, 8 poles and irregular distribution of slots with 3 different widths [10]. The result shows that the cogging torque of the concentrated machine is weak and electromagnetic produced torque is flat. Thus, a machine with concentrated and balanced winding is feasible and will present excellent performance.

Chapter 2

Operating Principles of Radial PM Machines

Nowadays there are several different topologies of rotating electrical machines. Most rotating machines are normally distinguished according to their direction of the flux field such as radial, axial, and transversal. The majority of machines are still designed basing on the inner-rotor-radial-flux layout, as it is the most established in design, analysis, and production. The radial permanent magnet motor is maintaining approximately the same torque density and the same outer dimensions as its counterpart machines. For an example, a PM synchronous machine (PMSM) requires a rotor flux field from permanent magnet and a stator carries stator windings flux when supplied with alternating currents. Its counterpart machines however, the rotor flux field is generated by a field winding. This rotor flux passes the airgap, encircles the stator windings and passes the airgap again back to the rotor backiron where thereby providing the magnetic flux linkage. The flux flows about radially in the machine airgap while the current flow about in the axial direction in the main region of the machine.

The radial permanent magnet motor is being increasingly used in industries such as aerospace application, consumer, medical, automotive industries, industrial automation etc [11]. This motor does not use any brushes for commutation; instead,

it is electronically commutated and thus it is well known as a brushless permanent magnet motor. This motor exists in single phase and multiphase but the 3-phase motors are most popular and widely used.

Typically the stator of a brushless machine consists of a three phase winding similar to that of induction machine hosted inside the slots of a cylindrical ferromagnetic core. The rotor of the motor includes permanent magnets and a ferromagnetic core that may feature different shapes. The motor characteristics depend on the stator winding and the way magnets are located on the rotor. The PMSM are traditionally classified into two variants basing on the waveform of the back EMFs which reflects the design peculiarities of the machine.

2.1 Sinusoidal Back-EMF motors

In this machine variant, typically the stator winding is distributed and the magnets and rotor core are designed to get sinusoidal back EMF waveform. In this type of motor, sinusoidal stator current is ideally needed to produce a ripple free electromagnetic torque. This type of brushless permanent magnet motor is commonly known as Permanent Magnet Synchronous Motor (PMSM) or Brushless AC Motor (BLAC).

2.2 Trapezoidal Back-EMF motors

In this version of the brushless PM motor, the back-EMF waveform is ideally trapezoidal. By changing the arrangement of magnet and the stator profile, the shape

of trapezoidal back-EMF waveform can also be adjusted. This type of brushless PM motor is commonly known as Brushless DC (BLDC) because the ideal waveform of stator current is 6-steps similarly to an elementary DC machine. The differences between these two motors are summarised in the following Table 2-1.

Parameters	PMSM	BLDC
Flux Linkage	Sinusoidal	Non-sinusoidal
Back EMF	Sinusoidal	Trapezoidal
Stator current	Sinusoidal	six-steps
Energised phases	Three phases all time	Two phases at any time
Output torque	Low Ripple	High Ripple

Table 2-1: PMSM and BLDC Comparison of Ideal Characteristics Machines

Throughout this thesis the following two motors have been designed and evaluated for their respective performances, adopting similar features in order to make significant comparisons. The general specification of the examined motors is shown in Table 2-2.

Parameters	PMSM/BLAC	BLDC
Motor Name	Q24P20	Q24P16
Slot Number	24	24
Pole Number	20	16
Length	100 mm	100 mm
External Radius	67 mm	67 mm
Rotor Radius	42 mm	42 mm
Nominal Torque Density	28.5 kN/m^3	28.5 kN/m^3

Table 2-2: General Specification of the Examined Motors

2.3 BLAC operation

The symmetrical 3-phase armature winding of the motor is connected to a 3-phase AC supply and the sinusoidal balanced stator currents produce a rotating magnetic field, as in 3-phase induction machines. The magnetic field of the permanent magnet is steady with respect to the rotor. To produce a steady torque, these two magnetic fields should rotate in the synchronous speed. This is quite similar to the DC motor operation in which the armature and excitation fields are synchronous but stationary for all operating speeds. The steady state operation of the PM synchronous motor ideally requires the supply frequency is directly related to the rotor speed, so that the MMF wave due to armature currents always moves at the same speed as the rotor. The PMSM requires a very accurate measurement of rotor speed and position and the

very precise adjustment of the stator frequency. One of the approaches in controlling the PM synchronous motor is by means of vector-controlled drive.

2.4 Mathematical Model of BLAC motor

BLAC is essentially a three-phase AC motor with sinusoidal back EMF driven by a DC source, which is converted to three-phase alternating currents supplying to the three stator windings of a BLAC by a controller unit such as a vector controlled drive. In order to drive a BLAC smoothly, a controller shall be designed such that the stator current space vector, which is the sum of the three phase currents, shall be always in the quadrature direction with respect to the rotor and has constant magnitude, irrespective of rotation speed and back EMF frequency. This results in maximum torque and minimum torque ripple and such model is valid for any instantaneous variation of voltage and current and adequately describes the performance of the machine under both steady-state and transient operation.

The operation of vector-controlled drive of any AC supplied motor such as PM synchronous motor is to imitate one of DC motor where the torque and flux are independently controlled by armature and field currents. The idea of the space vector permits to work with two variables instead of three and the motor can be considered a 2-phase machine. This technique is based on projections which transform a three phase time and speed dependent system into a two d-q axis coordinates (direct and quadrature) time invariant system known as field oriented frame which reduces the number of equations and simplifies the control design [12]. This field orientated frame controlled machines need two constants as input references: the torque

component (q coordinate) and the flux component (d coordinate). The transformation of the three-phase stationary coordinate system to the field oriented frame is made in two steps:

1) a transformation from the three-phase stationary coordinate system to the two-phase stationary coordinate system and
2) a transformation from the the two-phase stationary coordinate system to the d-q rotating coordinate system.

These direct and quadrature components are obtained from the three phases variables; a,b and c, through the Park transformation as below [13].

$$\begin{bmatrix} i_q \\ i_d \\ i_o \end{bmatrix} = 2/3 \begin{bmatrix} \cos(\theta) & \cos(\theta - 2\pi/3) & c\cos(\theta + 2\pi/3) \\ \sin(\theta) & \sin(\theta - 2\pi/3) & \sin(\theta + 2\pi/3) \\ 1/2 & 1/2 & 1/2 \end{bmatrix} \begin{bmatrix} i_a \\ i_b \\ i_c \end{bmatrix} \qquad (2.1)$$

Vice versa, the a,b, and c components are obtained from the direct and quadrature variables through the inverse of the Park transformation as defined below:

$$\begin{bmatrix} i_a \\ i_b \\ i_c \end{bmatrix} = \begin{bmatrix} \cos(\theta) & \sin(\theta) & 1 \\ \cos(\theta - 2\pi/3) & \sin(\theta - 2\pi/3) & 1 \\ c\cos(\theta + 2\pi/3) & \sin(\theta + 2\pi/3) & 1 \end{bmatrix} \begin{bmatrix} i_q \\ i_d \\ i_o \end{bmatrix} \qquad (2.2)$$

The principal operation of PMSM is similar to the traditional synchronous motor operation. The different is that the electrically excited field winding is replaced by the permanent magnets. A schematic representation of a synchronous motor and an equivalent circuit per phase are shown below in Figure 2-1.

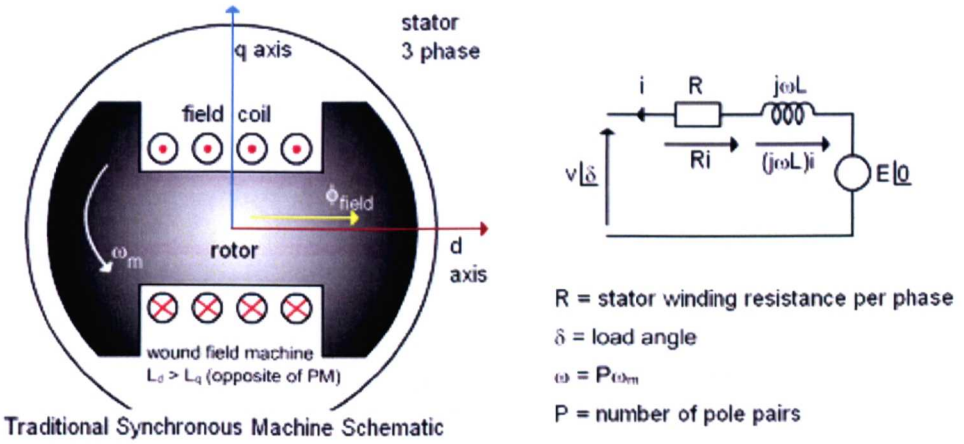

Figure 2-1: Synchronous motor schematic and equivalent circuit per phase

The representation of the machine in d and q axis is developed by analysing the armature winding on the stator and the permanent magnet rotor. Each winding coil and the magnet are considered to produce flux density distribution in the air gap, which are perfectly sinusoidal functions at the space angle θ. By considering the simple cross section of the two poles machine in simplified form where each equivalent winding d and q can be represented schematically by two conductors as shown in Figure 2-2. The direct axis component of the armature flux, ϕ_{ad} is produced by i_d and has the same direction as the magnet flux ϕ_m whereas the quadrature component of the armature flux ϕ_{aq} is produced by i_q.

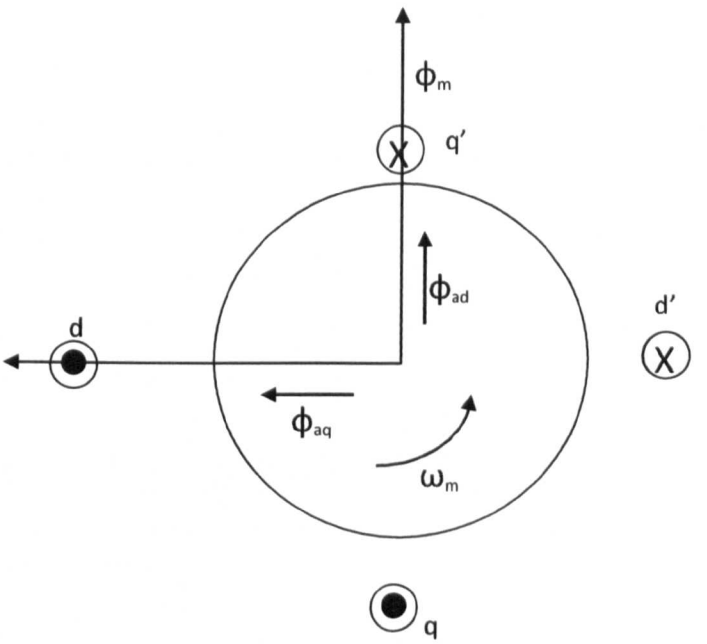

Figure 2-2: Two poles machine and two conductors schematic

For the above motor, the direction of id and iq are determined by an external voltage supplies, Vd and Vq respectively which supplies to the q and d coils. Basing on the above schematic, the machine equivalent model for the direct and quadrature axis is reported below in Figure 2-3 and Figure 2-4 accordingly [14].

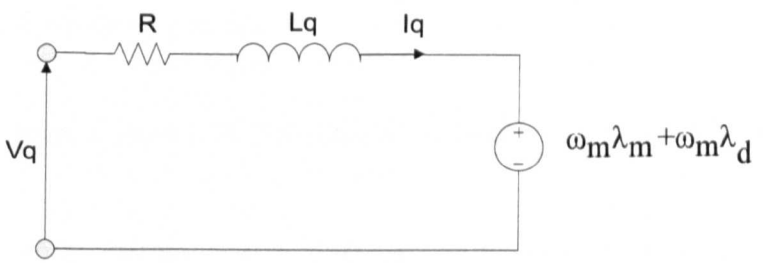

Figure 2-3: Equivalent circuit for quadrature axis

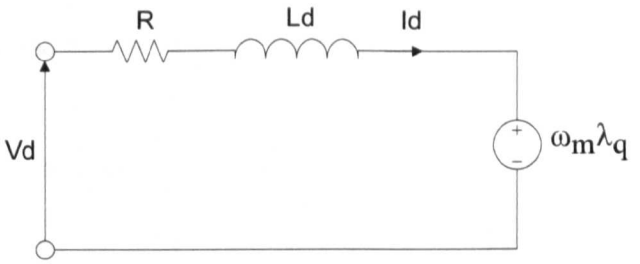

Figure 2-4: Equivalent circuit per phase for direct axis

The voltage equation for the quadrature and direct axis can be written as;

$$V_q = Ri_q + \frac{d\lambda_q}{dt} + \omega_e\lambda_m + \omega_e\lambda_d \tag{2.3}$$

$$V_d = Ri_d + \frac{d\lambda_d}{dt} - \omega_e\lambda_q \tag{2.4}$$

Where,

V_d and V_q : the d and q axis voltages

λ_d and λ_q : the d and q axis armature flux linkages

λ_m : the flux linkage due to the permanent magnet rotor linking the stator

i_d and i_q : the d and q axis armature current

R : the stator resistance

ω_e : the electrical angular frequency

The term $\frac{d\lambda_q}{dt}$ simply represents the induced voltage associated with quadrature inductance L_q, which has equivalent equation relationship as $\frac{d\lambda_q}{dt} = \frac{dL_q}{dt} \times i_q$. The term $\omega_m\lambda_m$ is the motional EMF induced by the magnet flux normally referred to as E and the term $\omega_m\lambda_d$ is the speed EMF induced by the armature in the d axis flux. Thus,

$$V_q=Ri_q+\frac{d\lambda_q}{dt}+E+\omega_m\lambda_d \text{ by substituting } \omega_m\lambda_m=E \quad (2.5)$$

The term $\frac{d\lambda_d}{dt}$ simply represents the induced voltage associated with direct axis inductance L_d, which has equivalent equation relationship, $\frac{d\lambda_d}{dt}=\frac{dL_d}{dt}\times i_d$. However, all the components $\frac{d\lambda}{dt}$ represent transient terms only and during the steady state condition, $\frac{d\lambda}{dt}=0$, and the above equations can be simplified as below:

$$V_q=Ri_q+E+\omega_e\lambda_d \quad (2.6)$$

$$V_d=Ri_d-\omega_e\lambda_q \quad (2.7)$$

Where, V is the resultant voltage, $V=\sqrt{V_d^2+V_q^2}$ (2.8)

And i is the resultant current, $i=\sqrt{i_d^2+i_q^2}$ (2.9)

The electromagnetic torque can be found directly from the total input power to the machine,P_{in}, in the a,b and c components as shown in the equations below [13]:

$$P_{in}=V_ai_a+V_bi_b+V_ci_c \quad (2.10)$$

While in direct and quadrature components, the total input power will be

$$P_{in}=3(V_d i_d+V_q i_q)/2 \quad (2.11)$$

By substituting the V_d and V_q equations into Equation (2.11) respectively,

$$P_{in}=3[(Ri_d-\omega_e\lambda_q)i_d+(Ri_q+E+\omega_e\lambda_d)i_q]/2 \quad (2.12)$$

By assuming that the voltage across resistance is small compare to the E and voltage produced from the flux linkage value, the equation shall be simplified as below:

$$P_{in}=3(Ei_q-\omega_e\lambda_q i_d+\omega_e\lambda_d i_q)/2 \quad (2.13)$$

Finally, the total electromagnetic torque is defined as the total input power to the machine divided by the motor's mechanical speed which is, $T_e=\frac{P_{in}}{\omega_m}$. Thus, the total electromagnetic torque equation is as below where rotor mechanical speed ω_m and electrical angular frequency ω_e is related as $\omega_e=P\omega_m$ with number of pole pairs, P.

$$T_e=3\left(\frac{Ei_q}{\omega_m}-P\lambda_q i_d+P\lambda_d i_q\right)\Big/2 \quad (2.14)$$

By substituting the $\lambda_d=L_d i_d$ and $\lambda_q=L_q i_q$ into the total electromagnetic torque equation,

$$T_e=3\left(\frac{Ei_q}{\omega_m}-PL_q i_q i_d+PL_d i_d i_q\right)\Big/2 \quad (2.15)$$

As i_d is set to be zero, then

$$T_e=3\left(\frac{Ei_q}{\omega_m}\right)\Big/2 \tag{2.16}$$

$$\text{Or } T_e=3\,P\left(\frac{Ei_q}{\omega_e}\right)\Big/2 \tag{2.17}$$

Since $\frac{E}{\omega_m}$ is equivalent to the magnetic flux linkage which is a constant waveform with respect to the rotor position, thus, the torque is directly dependent to the quadrature axis current. Then, the above shall be represented as

$$T_e=K_t i_q \tag{2.18}$$

$$\text{Where, } K_t=3\,P\left(\frac{E}{\omega_e}\right)\Big/2 \text{ is the torque constant.} \tag{2.19}$$

The electromagnetic torque value also appears in the mechanical equation of the machine. We also need to consider the impact of the mechanical system on the performance of the drive. The mechanical torque dynamics equation form is:

$$T_e=J\frac{d\omega_m}{dt}+B\omega_m+T_L \tag{2.20}$$

Where,T_L is the external load torque, J is the motor shaft inertia and B is the damping coefficient of viscous friction.

Basing on the above equations, a block diagram model of PMSM was created and analyzed in the Simulink Matlab environment and the results will be discussed at the end of this chapter.

2.5 BLDC operation

A BLDC motor rotates as a result of the interaction of its permanent magnet field at the rotor with a magnetic field generated when a DC voltage is connected across a set of its stator coils. To maintain rotation, the orientation of the stator magnetic field in the stator has to be rotated sequentially. Moreover, in order to deliver a higher power and torque which is ideally free from ripple, the desired rectangular AC wave back EMF and current would be preferred. Each phase current should be switched corresponding to machine back EMF as a function of the rotor position. At each rotor position, a constant current multiplies the constant part of the back EMF which the sum of the product produces the output power of the machine. Thus, in order to maintain synchronization with the rotating stator magnetic field and identify the commutation sequence for the above purpose, the rotor position must be known at fixed angular intervals.

The rotor position could be identified by the use of position sensors such as encoder, resolver or Hall sensors which could detect the position of the rotor field, and hence the position of the rotor shaft. The current commutation from one phase to the other phase corresponding to that particular state of the back EMF is synchronized by these position sensors. For Hall position sensors, three sensors are used to determine each back EMF and hence the position of the rotor field. These particular Hall position

sensors generate a logic high signal that goes low when the corresponding back EMF starts falling and remains low till that back EMF starts rising.

A conventional BLDC drive is illustrated in Figure 2-5 which consists of a dc link capacitor for energy storage that supplied by a rectifier, a 6-transistor inverter bridge and finally the three-phase output of the inverter to the motor.

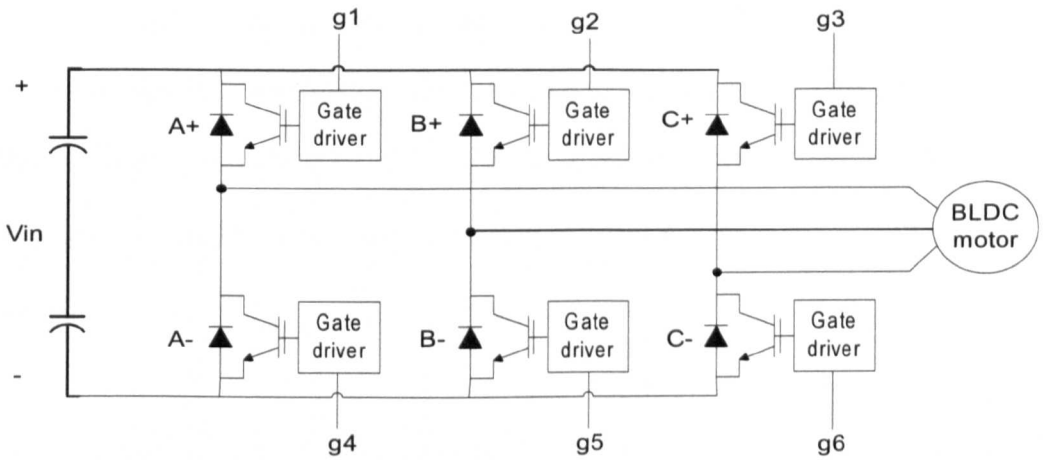

Figure 2-5: 6-transistor Inverter Bridge

Sequence number	Hall Sensor Input			Switching interval	Gate No. closed		Phase Current		
	A	B	C				A	B	C
1	1	1	1	0° - 60°	g1	g5	A+	B-	Off
2	1	1	0	60° - 120°	g1	g6	A+	off	C-
3	1	0	0	120° - 180°	g2	g6	off	B+	C-
4	0	0	0	180° - 240°	g2	g4	A-	B+	Off
5	0	0	1	240° - 300°	g3	g4	A-	off	C+
6	0	1	1	300° - 360°	g3	g5	off	B-	C+

Table 2-3: Switching Sequence of the 6-transistor Inverter Bridge

In order to drive the BLDC motor, the DC bus voltage is connected across two stator phases at any given time and the desired current profile are achieved by turning on one upper and one lower transistor pair for any 60 electrical degrees rotation. For a six-element bridge, there will be six distinct switching configurations as shown on the Table 2-3 above. This means that only two phases are conducting at any instant, with current entering one of the phases and leaving through the other. The BLDC motor will rotate 360 electrical degrees if the six switching configurations are changed sequentially at 60-degree intervals in synchronization with the rotor position. After completing the six steps, the sequence is repeated. This method is called the 120-degree method because every switching element is turned on for 120 electrical degrees.

In the 120-degree method, the commutation patterns are changed so that the angle between the magnetic pole of the rotor and rotating magnetic field of the stator is in a range of 60 to 120 degrees (the direction of the stator flux depends on how the coils are wound). Several techniques can be used to control the phase current of the BLDC motor. In this simulation, a hysteresis current controller is used by comparing the actual current with a trapezoidal shape reference current as shown in Figure 2-6 [15].

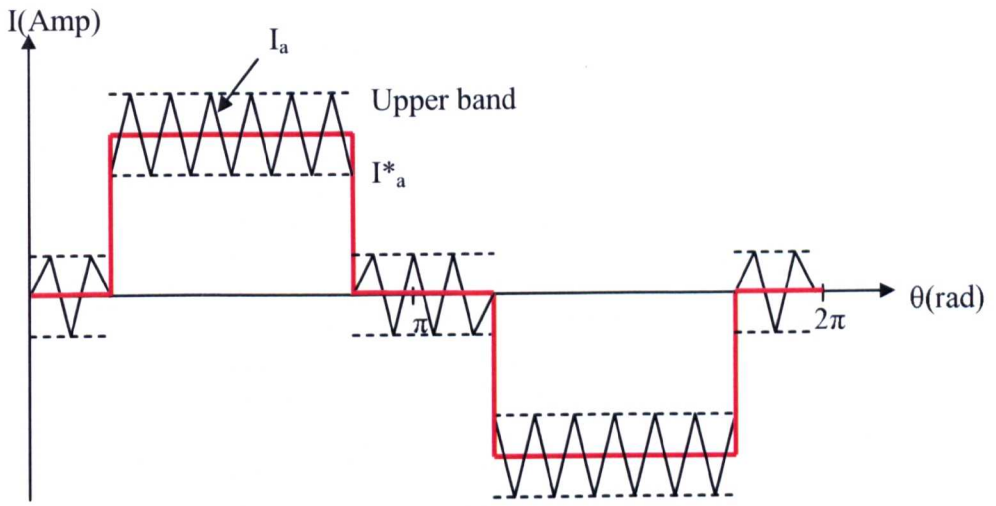

Figure 2-6: Hysteresis Current Control

2.6 Mathematical Model of BLDC motor

A simple three-phase two-pole star connected BLDC motors and a 1-phase equivalent circuit schematic is shown in Figure 2-7:

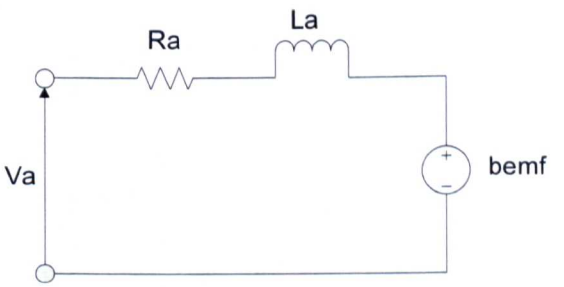

Figure 2-7: BLDC 1-phase equivalent circuit schematic

The circuit equations of the three windings in phases are [16]

$$V_a = R_a i_a + \frac{d\psi_a}{dt} \qquad (2.21)$$

$$V_b = R_b i_b + \frac{d\psi_b}{dt} \tag{2.22}$$

$$V_c = R_c i_c + \frac{d\psi_c}{dt} \tag{2.23}$$

Where

R_a, R_b, R_c: Winding Resistances of each phase in ohm, Ω

V_a, V_b, V_c: Phase voltages on motor winding in volt, V

i_a, i_b, i_c: Phase currents in ampere, A

ψ_a, ψ_b, ψ_c: Flux linkages of each phase in weber, Wb

The flux linkages for each phase are defined as

$$\psi_a = L_a i_a + L_{ab} i_b + L_{ac} i_c + \psi_{am} \tag{2.24}$$

$$\psi_b = L_b i_b + L_{ba} i_a + L_{bc} i_c + \psi_{bm} \tag{2.25}$$

$$\psi_c = L_c i_c + L_{ca} i_a + L_{cb} i_b + \psi_{cm} \tag{2.26}$$

Where

L_a, L_b, L_c: Self inductances of each phase in henry, H

L_{ab}, L_{ac}, L_{ba}, L_{bc}, L_{ca}, L_{cb}: Mutual inductances of between phases in henry, H

ψ_{am}, ψ_{bm}, ψ_{cm}: Flux linked with each phase due to the permanent magnet at each phase in weber, Wb

From the above two series of equation, the matrix form shall be written as

$$\begin{bmatrix} V_a \\ V_b \\ V_c \end{bmatrix} = \begin{bmatrix} R_a & 0 & 0 \\ 0 & R_b & 0 \\ 0 & 0 & R_c \end{bmatrix} \begin{bmatrix} i_a \\ i_b \\ i_c \end{bmatrix} + \frac{d}{dt} \begin{bmatrix} L_a & L_{ab} & L_{ac} \\ L_{ba} & L_b & L_{bc} \\ L_{ca} & L_{cb} & L_c \end{bmatrix} \begin{bmatrix} i_a \\ i_b \\ i_c \end{bmatrix} + \frac{d}{dt} \begin{bmatrix} \psi_{am} \\ \psi_{bm} \\ \psi_{cm} \end{bmatrix} \tag{2.27}$$

The rate of change of the flux linkages established by the permanent magnet at each phase is equal to the induced back EMF in the winding. By assuming that there is no change in the rotor reluctances, then the self and mutual inductances of every phase will be similar respectively. It is also assumed that the winding resistances are equal. Hence the above equation shall be written as

$$\begin{bmatrix} V_a \\ V_b \\ V_c \end{bmatrix} = \begin{bmatrix} R & 0 & 0 \\ 0 & R & 0 \\ 0 & 0 & R \end{bmatrix} \begin{bmatrix} i_a \\ i_b \\ i_c \end{bmatrix} + \frac{d}{dt} \begin{bmatrix} L & M & M \\ M & L & M \\ M & M & L \end{bmatrix} \begin{bmatrix} i_a \\ i_b \\ i_c \end{bmatrix} + \begin{bmatrix} e_a \\ e_b \\ e_c \end{bmatrix} \qquad (2.28)$$

When the 3 phases are wye-connected without neutral, the sum of the three phases currents is zero.

$i_a = -i_b - i_c$

Therefore, the equation 2.28 may be written as

$$L\frac{di_a}{dt} + M\frac{di_b}{dt} + M\frac{di_c}{dt} = L\frac{di_a}{dt} + M\left(\frac{di_b}{dt} + \frac{di_c}{dt}\right)$$

$$= L\frac{di_a}{dt} + M\left(-\frac{di_a}{dt}\right)$$

$$= (L-M)\frac{di_a}{dt}$$

And similarly

$$\begin{bmatrix} V_a \\ V_b \\ V_c \end{bmatrix} = \begin{bmatrix} R & 0 & 0 \\ 0 & R & 0 \\ 0 & 0 & R \end{bmatrix} \begin{bmatrix} i_a \\ i_b \\ i_c \end{bmatrix} + \frac{d}{dt} \begin{bmatrix} L-M & 0 & 0 \\ 0 & L-M & 0 \\ 0 & 0 & L-M \end{bmatrix} \begin{bmatrix} i_a \\ i_b \\ i_c \end{bmatrix} + \begin{bmatrix} e_a \\ e_b \\ e_c \end{bmatrix} \qquad (2.29)$$

The above differential equation may be put in canonical form by multiplying by the inverse inductance matrix, L^{-1}

$$\frac{d}{dt}\begin{bmatrix} i_a \\ i_b \\ i_c \end{bmatrix} = -L^{-1}R\begin{bmatrix} 1 & 0 & 0 \\ 0 & 1 & 0 \\ 0 & 0 & 1 \end{bmatrix} + -L^{-1}\begin{bmatrix} V_a \\ V_b \\ V_c \end{bmatrix} + -L^{-1}\begin{bmatrix} e_a \\ e_b \\ e_c \end{bmatrix} \tag{2.30}$$

The electromagnetic torque is given by

$$T_e = \frac{e_a i_a + e_b i_b + e_c i_c}{\omega_{rm}} \tag{2.31}$$

Or by using the expression of coenergy [16]

$$T_e = \frac{P}{2}\frac{\partial W_c(\theta_{re})}{\partial \theta_r} \tag{2.32}$$

where P, W_c and θ_{re} are the number of poles, coenergy and electrical rotor position respectively.

$$W_c(\theta_{re}) = \frac{1}{2}\begin{bmatrix} i_a & i_b & i_c \end{bmatrix} L \begin{bmatrix} i_a \\ i_b \\ i_c \end{bmatrix} + \begin{bmatrix} i_a & i_b & i_c \end{bmatrix} \begin{bmatrix} \psi_m \sin\theta_{re} \\ \psi_m \sin(\theta_{re} - 2\pi/3) \\ \psi_m \sin(\theta_{re} + 2\pi/3) \end{bmatrix} + W_{pm} \tag{2.33}$$

For surface-mounted PM machines, the direct and quadrature axis inductances are approximately equal, thus the inductance matrix, L and the energy stored in the permanent magnet, W_{pm} are not functions of θ_r [17]. Therefore,

$$T_e = \frac{P}{2}\frac{\partial W_c(\theta_{re})}{\partial \theta_{re}} = \frac{P}{2}\begin{bmatrix} i_a & i_b & i_c \end{bmatrix} \frac{\partial}{\partial \theta_r} \begin{bmatrix} \psi_m \sin\theta_{re} \\ \psi_m \sin(\theta_{re} - 2\pi/3) \\ \psi_m \sin(\theta_{re} + 2\pi/3) \end{bmatrix}$$

$$T_e = \frac{P}{2}\frac{\partial W_c(\theta_{re})}{\partial \theta_{re}} = \frac{P\psi_m}{2}\left[i_a \cos\theta_{re} + i_b \cos(\theta_{re} - 2\pi/3) + i_c \cos(\theta_{re} + 2\pi/3)\right] \tag{2.34}$$

The mechanical equation is as below:

$$T_e = J\frac{d\omega_{rm}}{dt} + B\omega_{rm} + T_L \tag{2.35}$$

The mechanical differential equations shall be derived by equating the above two equations (2.34) and (2.35)

$$\begin{aligned} T_e &= \frac{P}{2}\frac{\partial W_c(\theta_{re})}{\partial \theta_{re}} = J\frac{d\omega_{rm}}{dt} + B\omega_{rm} + T_L \\ \frac{d\omega_{rm}}{dt} &= \frac{P}{2J}\frac{\partial W_c(\theta_{re})}{\partial \theta_{re}} - \frac{B}{J}\omega_{rm} - \frac{1}{J}T_L \\ \frac{d\theta_{rm}}{dt} &= \omega_{rm} \end{aligned} \qquad (2.36)$$

By using the conversion of electrical-mechanical angular speed and displacement relationship as below, the mechanical differential equations are described as

$$\omega_{rm} = \frac{2}{P}\omega_{re} \quad \text{and} \quad \theta_{rm} = \frac{2}{P}\theta_{re}$$

$$\begin{aligned} \frac{2}{P}\frac{d\omega_{re}}{dt} &= \frac{P}{2J}\frac{\partial W_c}{\partial \theta_{re}} - \frac{B}{J}\frac{2}{P}\omega_{rm} - \frac{1}{J}T_L \\ \frac{d\omega_{re}}{dt} &= \frac{P^2}{4J}\frac{\partial W_c}{\partial \theta_{re}} - \frac{B}{J}\omega_{rm} - \frac{P}{2J}T_L \\ \frac{d\theta_{re}}{dt} &= \omega_{re} \end{aligned} \qquad (2.37)$$

2.7 Measurement of the Motor Parameters

Before the mathematical model of a PM machine could be applied into a computer program for the simulation, it is necessary to determine the motor parameters. The basic motor parameters that are required for the model are the stator winding resistance, stator winding inductances and the mechanical dynamic coefficients such as the inertia and the friction.

2.8 Stator winding resistance measurement

The resistance shall be determined in two methods; experimental and analytical. In experimental method, a DC source is supplied into the winding and the resistance is the ratio of the voltage to the current across it. The following digital micro-ohmmeter *Valhalla Scientific 4300B* is capable in providing the measurement and produces the result on the screen. In analytical method, the winding resistance is calculated basing on the actual geometry of the motor and the winding property. The geometry of the BLDC motor considered is shown in Figure 2-8. The total length of the winding conductor can be estimated as below.

$$L_{cu}=\left[L_{mot}+2.EndWdg+T_w+\left(\frac{W_{slo}+W_{sli}}{2}\right)\right].2.str.Nturn.N_{slot} \qquad (2.38)$$

Where

L_{cu}: Total length of the stator winding

L_{mot} : The axial length of the stator core

EndWdg : End winding length of the conductor

T_w : The tooth width

W_{slo} and W_{sli}: The slot width at inner and outer radius of slot area respectively

str : The number of stranded conductor per turn

Nturn : The number of conductor turn per tooth

N_{slot} : The total number of stator slot

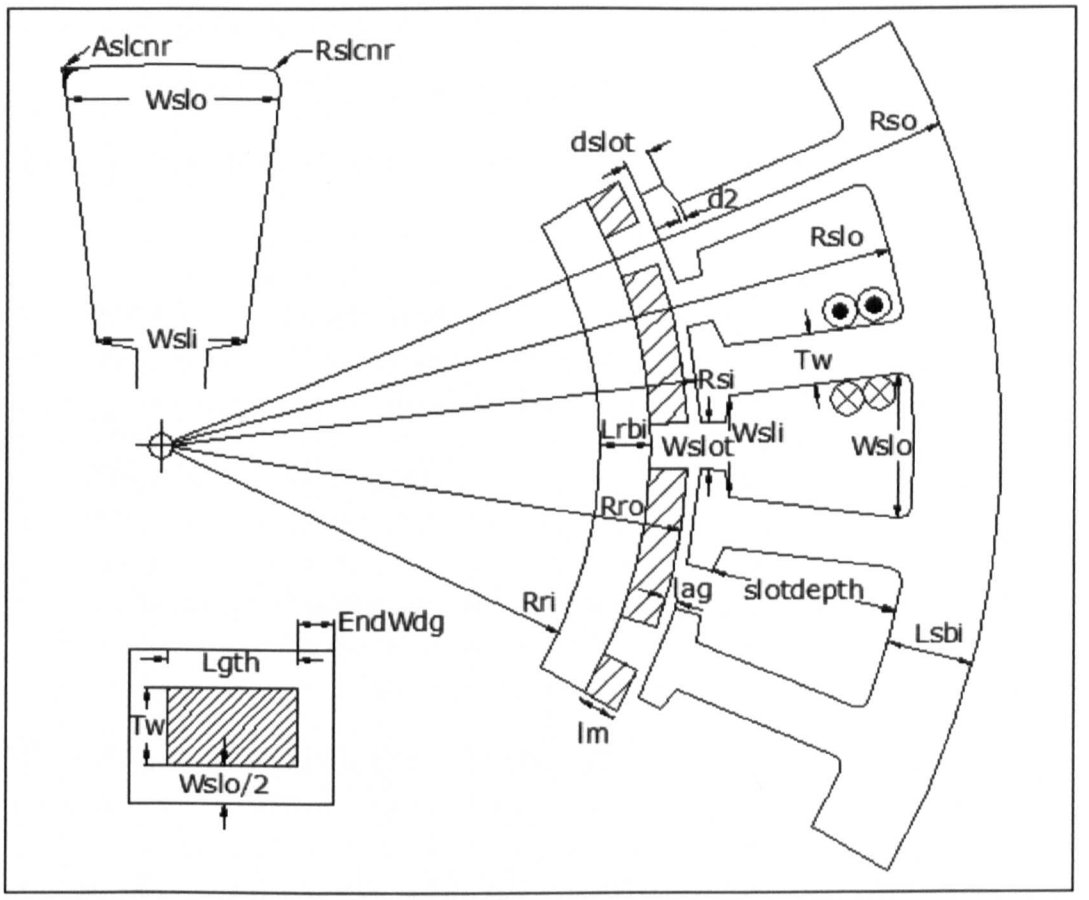

Figure 2-8: Motor Slot Geometry

The stator winding resistance for each phase are defined as

$$R_a = \frac{L_{cu}.str}{\sigma.A_{cu}.str^2.Ph} \tag{2.39}$$

Where

R_a : Winding Resistances of each phase in ohm, Ω

σ : Winding conductor conductivity in $\frac{1}{\Omega.mm}$

A_{cu} : Winding Conductor area in mm^2

Ph : The number of phases.

A detail analytical calculation on the winding resistance is done in ***MathCAD*** program and Table 2-4 below is the comparison results between experimental and analytical which are very similar.

Resistance	Experimental(Ω)	Analytical(Ω)	Different (%)
Phase a	1.60	1.52	4.73
Phase b	1.60	1.52	4.64
Phase c	1.60	1.52	4.82

Table 2-4: Comparison of BLDC's Winding Resistance Results

2.9 Stator Winding Inductance Measurement

The inductance matrix consists of two types of elements; self and mutual inductances. They are related to the effects of leakage and magnetizing flux tubes. In the case of salient pole machines, the inductances vary with the rotor position because the effective air gap length is not constant along the circumferential direction [16]. The differential inductances may be determined using finite element analysis for given rotor position and current loading as shown in Figure 2-9 [18]. A phase self inductance can be determined by imposing a small change in the current of the selected phase and keeping the other phase currents to zero. The selected phase self inductance is given by the ratio of the change of flux linkage by the change of current in that phase according to in the equation below.

$$L_a = \frac{\Delta \psi_a}{\Delta i_a} \qquad (2.40)$$

The mutual inductance vs. a second phase is calculated as the ratio of the change of flux linkage in the other phase by the change of current in the abovementioned phase. The results may depend on motor position, and in case of non-linear materials such procedure should be repeated per each significant operation condition.

$$M_{ab} = \frac{\Delta\psi_b}{\Delta i_a} \tag{2.41}$$

$$M_{ac} = \frac{\Delta\psi_c}{\Delta i_a} \tag{2.42}$$

In Figure 2-9 are reported the results obtained for self and mutual inductance of BLDC motor.

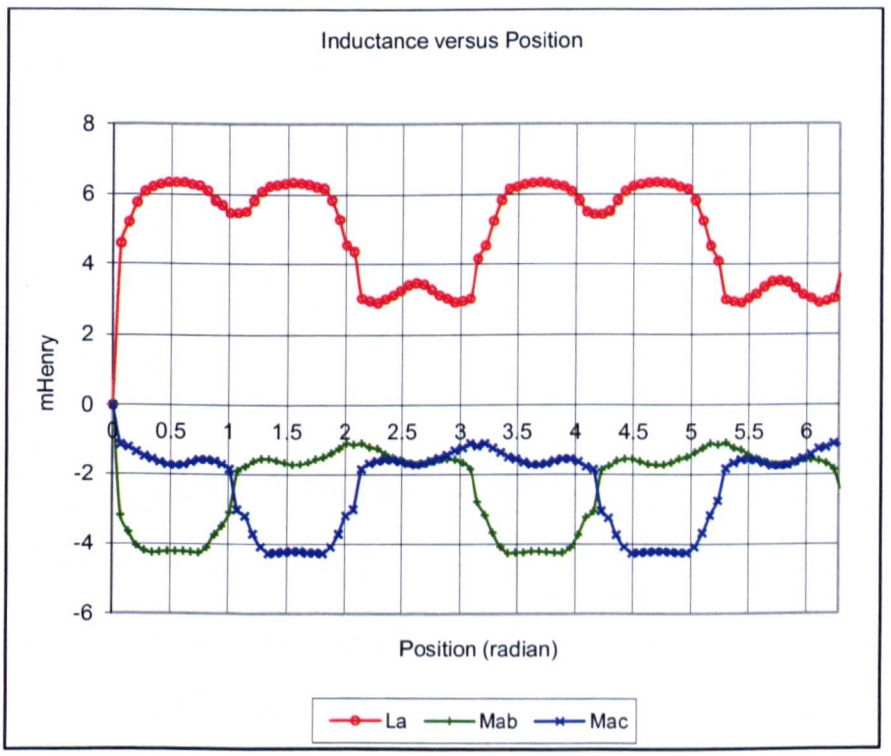

Figure 2-9: Self and Mutual Inductance of BLDC motor

2.10 Simulation of Motor Operation

The simulation of the PMSM and BLDC motors as described earlier in Table 2.2 was done using the software package MATLAB/SIMULINK. Basing on the above equations, the overall structure of the BLAC and BLDC models were created as shown in Figure 2-10 and Figure 2-13 respectively. The actual waveforms of the flux linkage and cogging torque obtained from the finite element analysis at null currents of the both motors were fed into the models in order to generate the expected back EMF waveforms and electromagnetic torque respectively.

In this simulation, the PMSM motor was simulated with vector current controller and PI speed regulator. However, the BLDC motor was driven with hysteresis current controller and PI speed regulator and the effectiveness of those controllers were discussed. After running the simulation, the current, back EMF, speed and electromagnetic torque waveforms were recorded and analyzed as shown in Figure 2-16 and Figure 2-17.

The phase currents for the PMSM are a sinusoidal wave which is similar to its back EMF and contrarily for the BLDC, the waveform are trapezoidal for both the current and the back EMF. However, the phase current and back EMF waveforms are distorted from the square wave shape due to the inductance and slotting effect. The final steady state speed of 800 rpm is reached for the both motors with no overshot. As expected, the load torque is a constant straight line of 20 N-m with some torque ripples. Table 2-5 below shows the summary of the results for the both motors at the steady state condition.

Parameters	PMSM	BLDC
Load Torque	40 N-m	40 N-m
Reference Speed	800 rpm	800 rpm
RMS Voltage	100.17 V	250.00 V
RMS Current	16.96 A	10.78 A
RMS BEMF	73.79 V	106.98 V
Steady-state Speed	800.21 rpm	799.46 rpm
Average Torque	40.04N-m	40.02 N-m
Ripple Torque	1.50 %	50.37%
K_t	2.386	3.711
Copper loss	431.46 watt	350.95 watt
Iron loss	24.18 watt	20.42 watt
Efficiency	65.81%	62.15%

Table 2-5: Summary of the simulation results

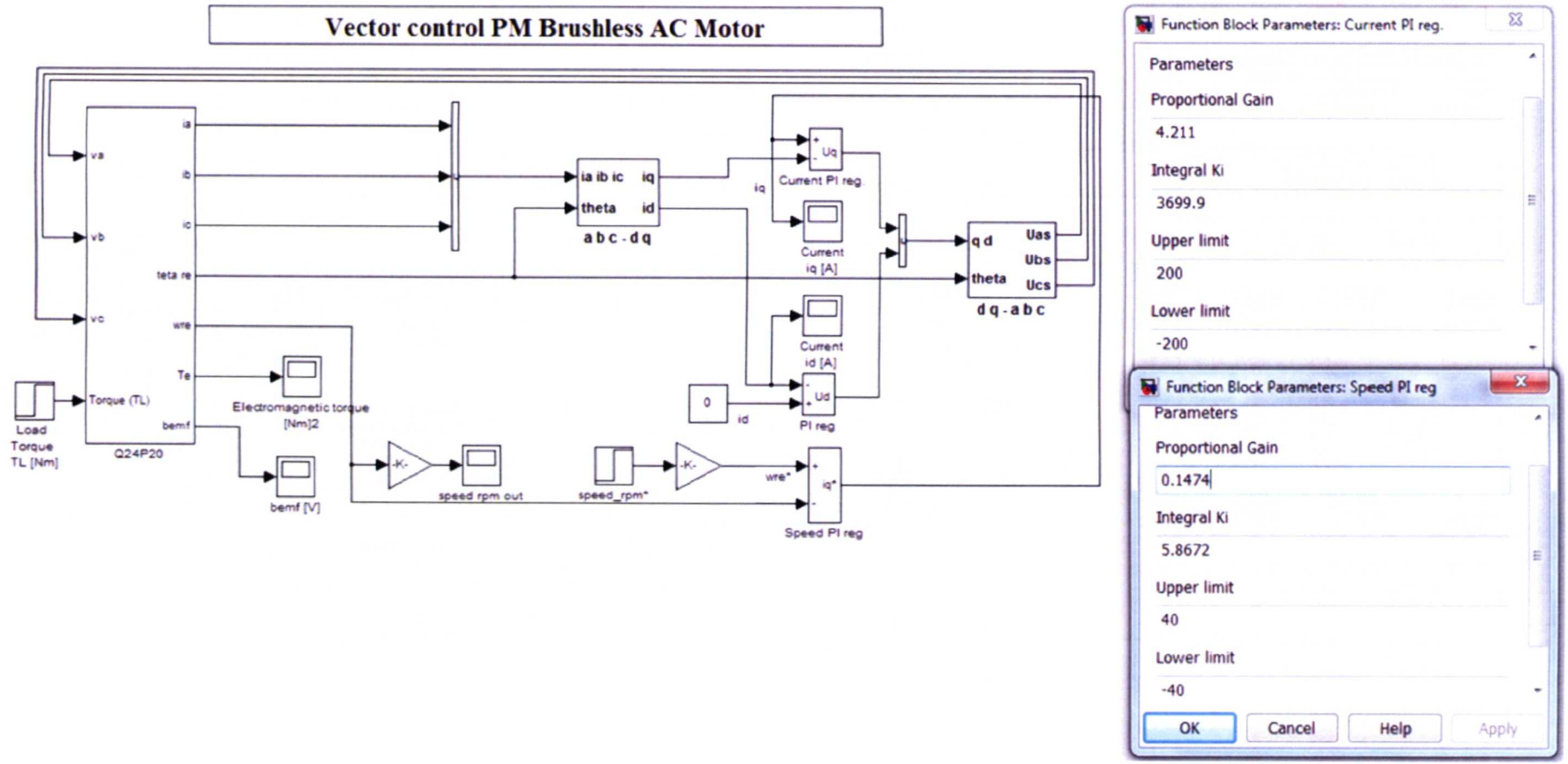

Figure 2-10: Block Diagram of PMSM Operation and the Controllers' Parameters

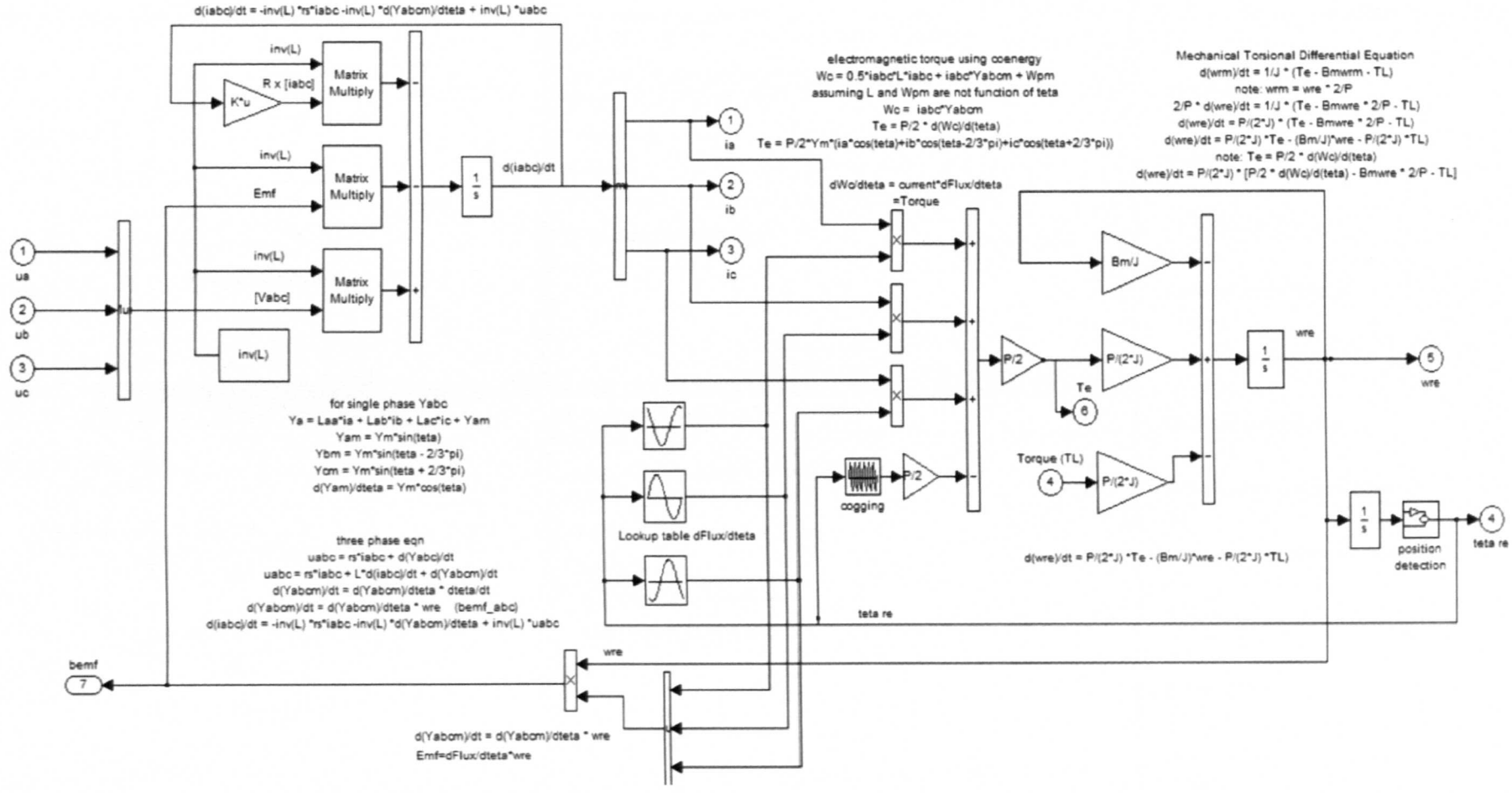

Figure 2-11: Block Diagram behind Subsystem Q24P20 Shown in Figure 2-10

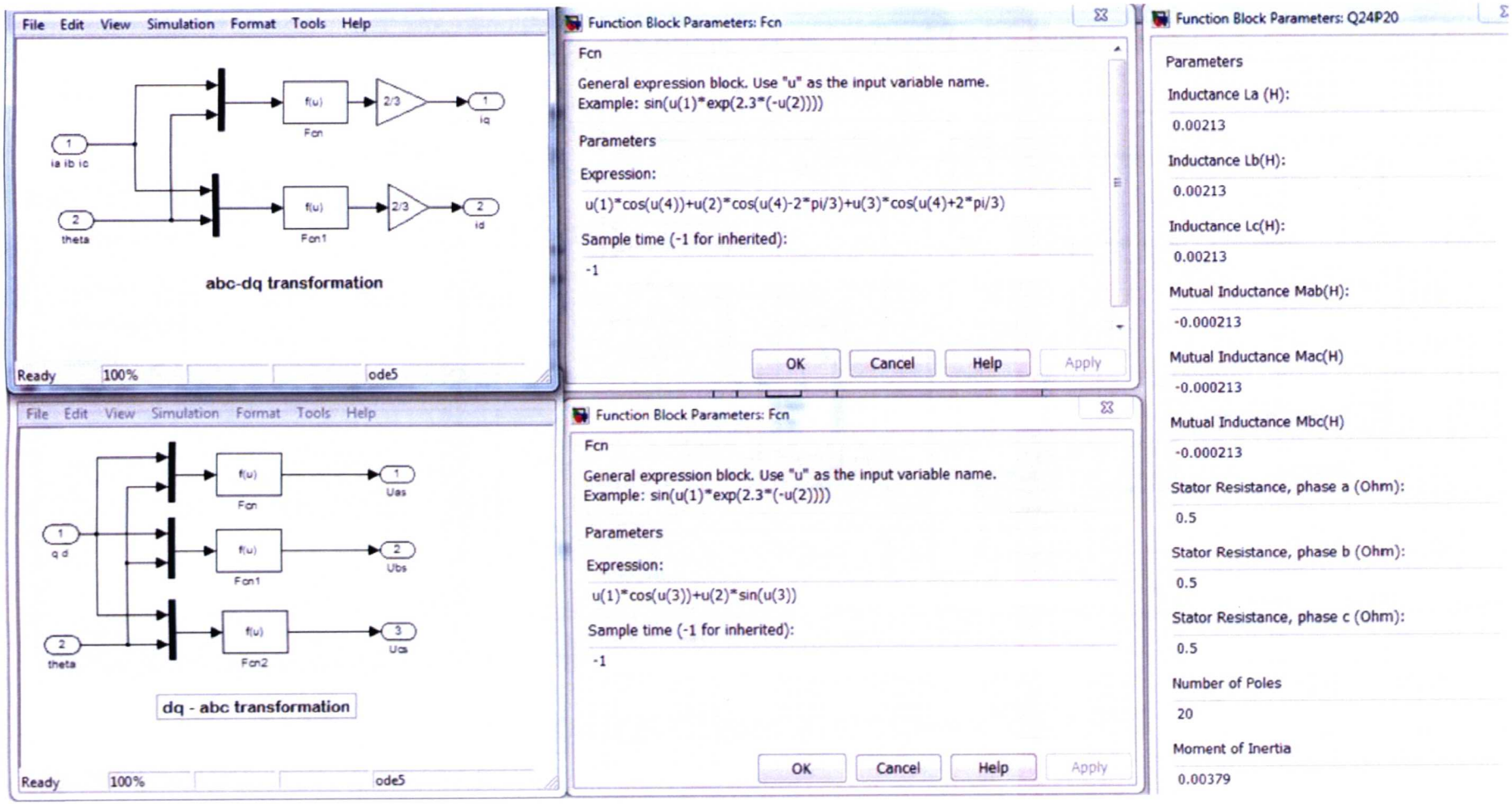

Figure 2-12: Machine's Parameters and D-Q Transformation Blocks

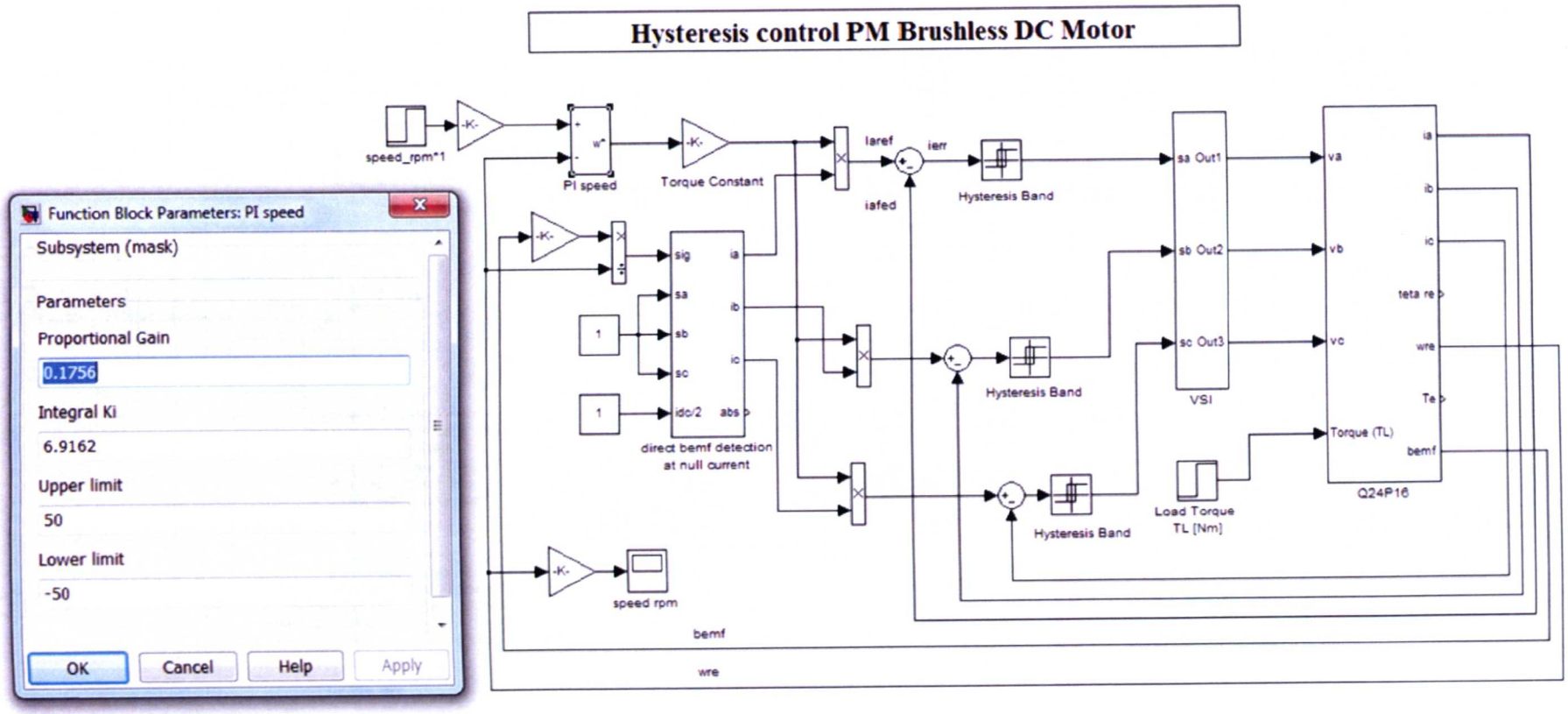

Figure 2-13: Block Diagram of BLDC Operation and the Machine's Parameters

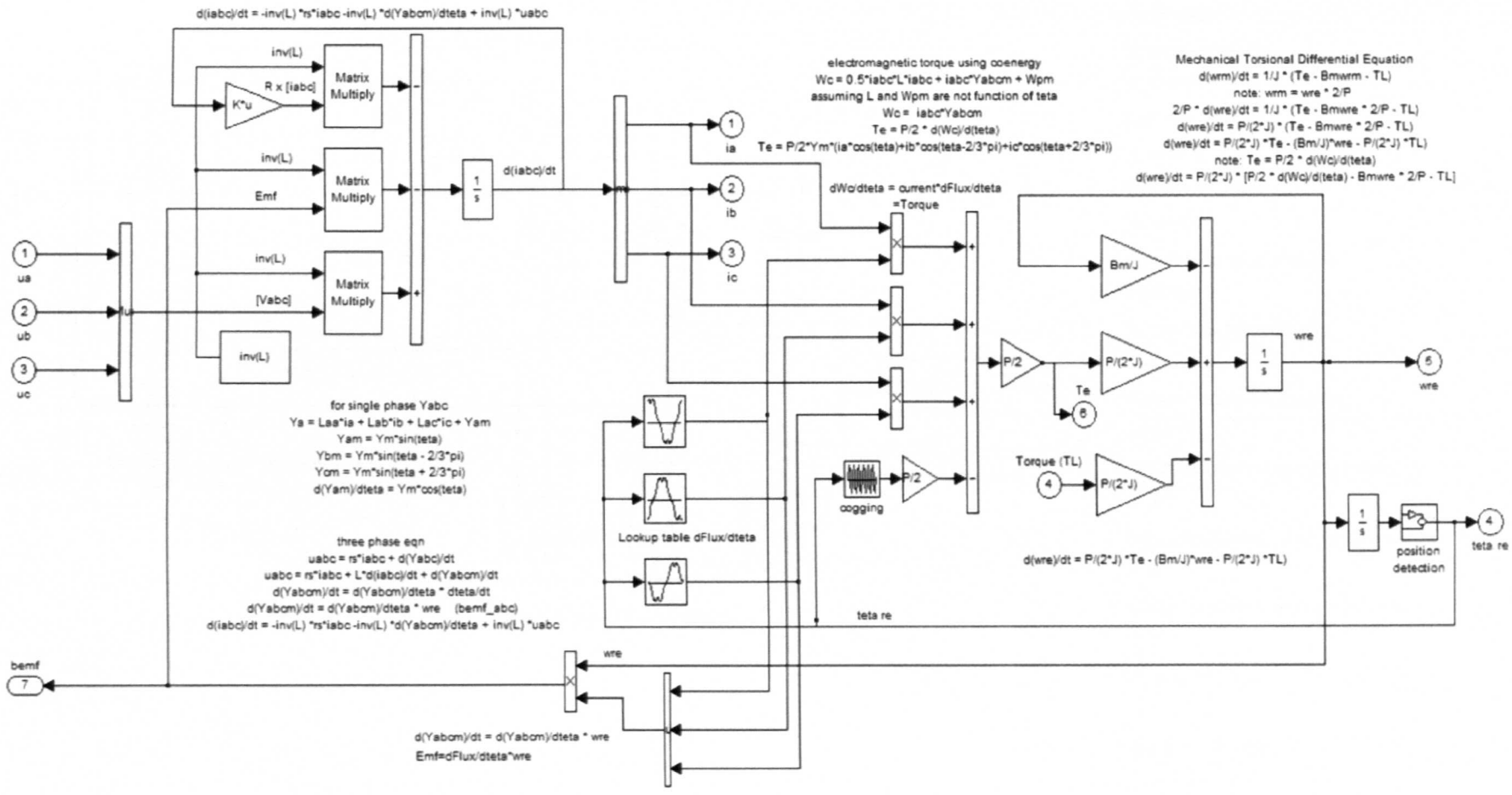

Figure 2-14: Block Diagram behind Subsystem Q24P16 Shown in Figure 2-13

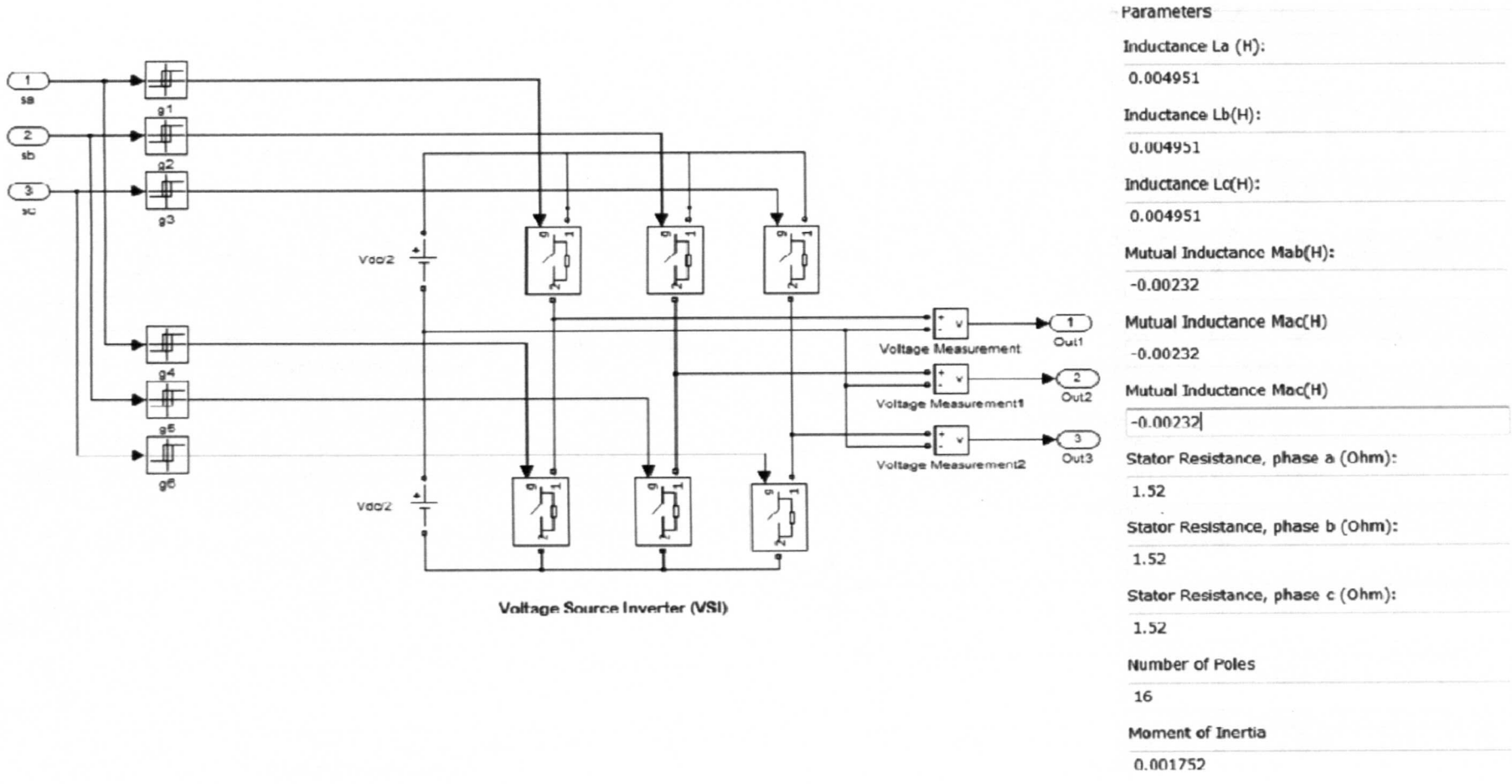

Figure 2-15 : Machine's Parameters and VSI Block

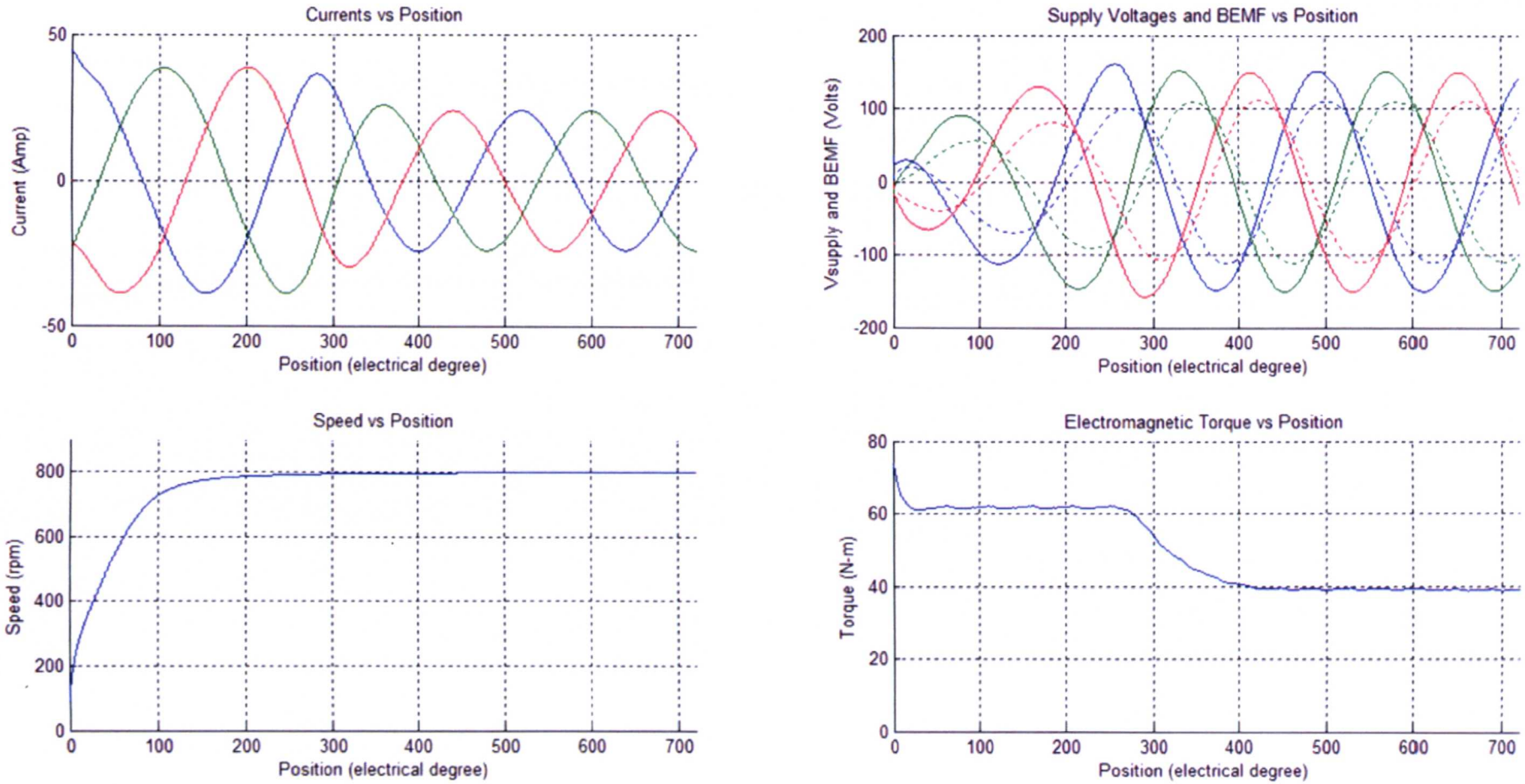

Figure 2-16: Waveforms Obtained from PMSM Operation

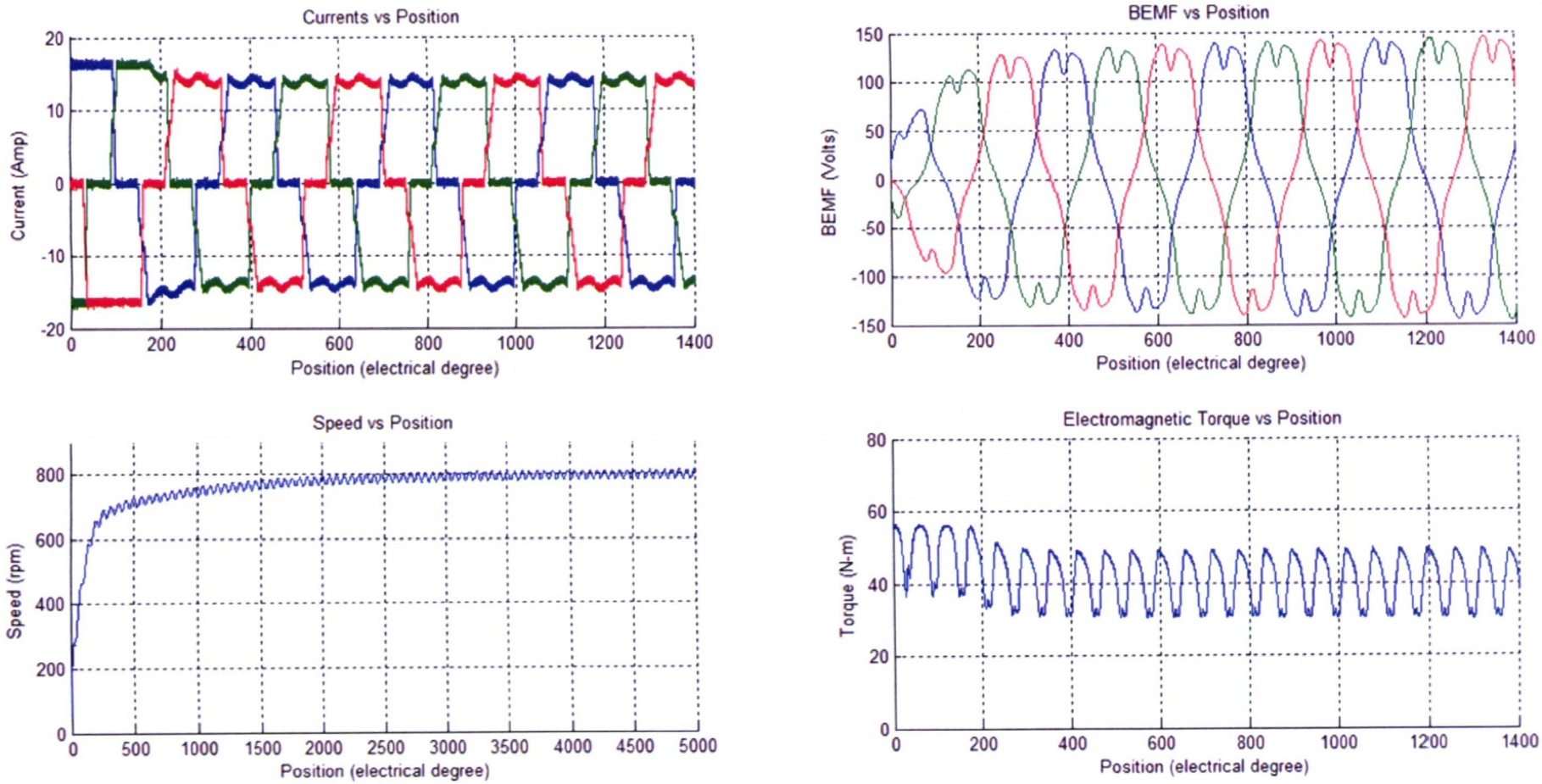

Figure 2-17: Waveforms Obtained from BLDC Operation

Chapter 3

PM Machines Design Procedure and Analysis

This work deals with the design of radial flux BLDC/AC interior rotor motor topology. The design of a BLDC motor will be mostly detailed but considerations for BLAC machines will also be highlighted. The design procedure for this motor will be discussed in this chapter and the detail on the design sequences is shown in Appendix A, whereas the parameters calculation is performed using ***Mathcad*** software programming in Appendix B and is optimised by finite element analysis software, Magnet.

3.1 Finite Element Analysis

Magnet is the software used for the finite element method. The results are used to verify the analytical calculations. The machine geometry is drawn and the different machine parts are assigned a specific material as shown in Figure 3-1. In a magnetic simulation, the non-magnetic materials are represented by vacuum. The magnet material is created in order to describe the required remanence flux density. The suggested iron material is available in the material database.

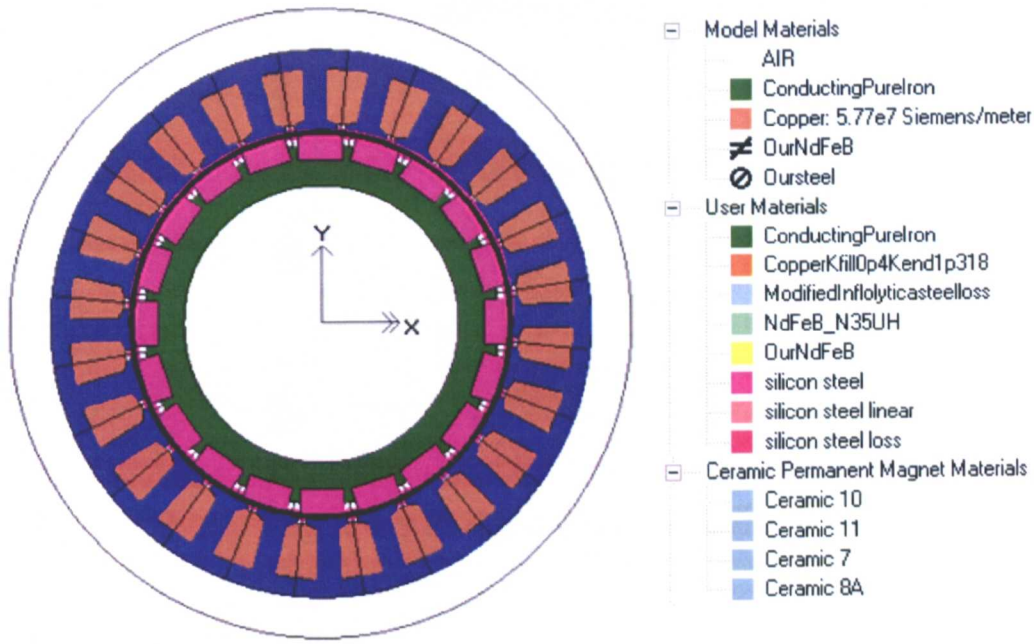

Figure 3-1: Finite element geometry of the motor

There are two types of simulations namely:

1) magneto-static, used for calculation of the flux density created by the magnets
2) transient magnetic, used for calculations of the torque and the iron losses at rated speed

For the transient magnetic simulation, a circuit is used in order to impose the rated currents. This circuit is shown in Figure 3-2: Electrical circuit with load

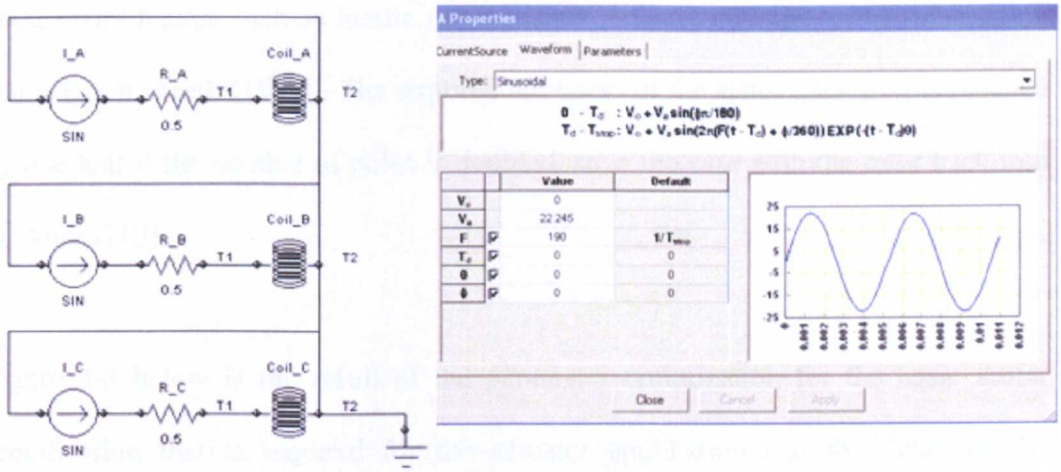

Figure 3-2: Electrical circuit with load

The corresponding current sources are assigned to the stator winding which phase shifted by 120 degrees for a three phase system. The coils A+ and A- represent one slot of the positive and the negative phase A and contain the number of conductors per slot as shown in Figure 5-11 which will be explained in Chapter 5. The resistance of each coil is calculated from the phase resistance which represents the total resistance of one phase.

In general, for an application that requires a rapid acceleration and deceleration of the load, it is desirable that the torque/inertia ratio is as high as possible [19]. In this case, the interior-rotor designs with high energy magnets are preferred. The BLDC motor presented in this thesis is an interior-rotor design and 3 types of motor with different poles combination will be analyzed.

The number of phases, poles, stator slots as well as winding configuration must be selected based on the application requirements. The choice of pole number depends

upon many factors such as inertia requirements, magnet material, effect of cogging and rotation speed. [19,20]. The required thickness of the stator back iron is reduced by one half if the number of poles is doubled, so is the case with the rotor back iron thickness [19].

Figure 3-3 below is the result of the parameter optimization for the basic motor specification that is required for the actuator application and the detail of the parameters determination will be specifically presented.

No of Pole : 16

No of Slot : 24

Length : 100mm

Radius : 67mm

Magnet Thickness : 3mm

Magnet Span : 140^{o}

Airgap Length : 1mm

Slot Tooth ratio : 2.5

Slot Opening : 3.6mm

Current Density : $10Arms/mm^2$

Rated Torque : 40 N-m

Speed : 800 rpm

Nominal Torque Density : $28.5\ kN/m^3$

Torque Rotor Volume (TRV) : $72kN/m^3$

Weight : 6.2kg

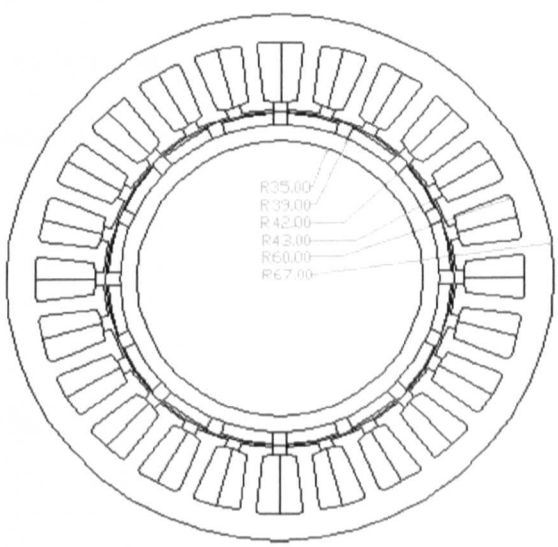

Figure 3-3: Basic specifications and parameters

3.2 Number of Phases

The choice of number of phases depends upon several reasons and factors. Single phase motors are easy to wind and low cost and require only one or two power switches. However, they have poor conductor utilization, high torque ripple, and are difficult to start [22]. Two-phase motors also have poor conductor utilization, but the torque ripple is greatly reduced, and the cost is higher because a minimum of four power switches are required. In a contrast, a three phase motors have better conductor utilization, no starting problems, and greatly reduced torque ripple. They can get by with as few as three power switches, but they generally cost more to wind the motors. Increasing the number of phases to four or greater realizes small gains in copper utilization and torque ripple, but the costs of winding and power switches usually outweigh the gains in small medium machines [22].

3.3 Number of Poles

Some general rules of thumb to consider when selecting the number of poles are explained below [22]

i) Increase in poles number will reduce the requirement for rotor and stator back iron since the total flux is spread over more poles reducing the density and as a result more space is available for windings and allowing for a reduction in copper losses.

ii) Increase in poles number will raise the number of parts and consequently cost more money for the same amount of material.

iii) Increase in poles number will increase in electrical frequency for given mechanical speed, affecting specific iron and copper losses and possibly lowering overall efficiency.

3.4 Rotor Radius

For a given torque, magnetic and electric loading, and the machine length the overall machine rotor diameter can be determined as follows [21].

$$T = \frac{\pi}{2} \cdot B \cdot \Delta I \cdot L \cdot (2R)^2 \qquad (3.1)$$

where B is called magnetic loading (T) , ΔI is called electrical loading (A/m) , L is motor length and R is rotor radius. Therefore the radius of the machine rotor is then,

$$R_r = \sqrt{\frac{T}{2\pi \cdot B \cdot \Delta I \cdot L}} \qquad (3.2)$$

3.5 Magnet Thickness

Permanent magnet used in PM motors is magnetized and has a remaining remanent flux density and responds to a normal hysteresis characteristic. The useful portion of a magnet in PM operation is in the second quadrant of the hysteresis loop and is usually called the demagnetization curve of the magnet. It represents the relationship between B and H of the magnet once it has been magnetized. Typical demagnetization curve for permanent magnet is shown in Figure 3-4 .

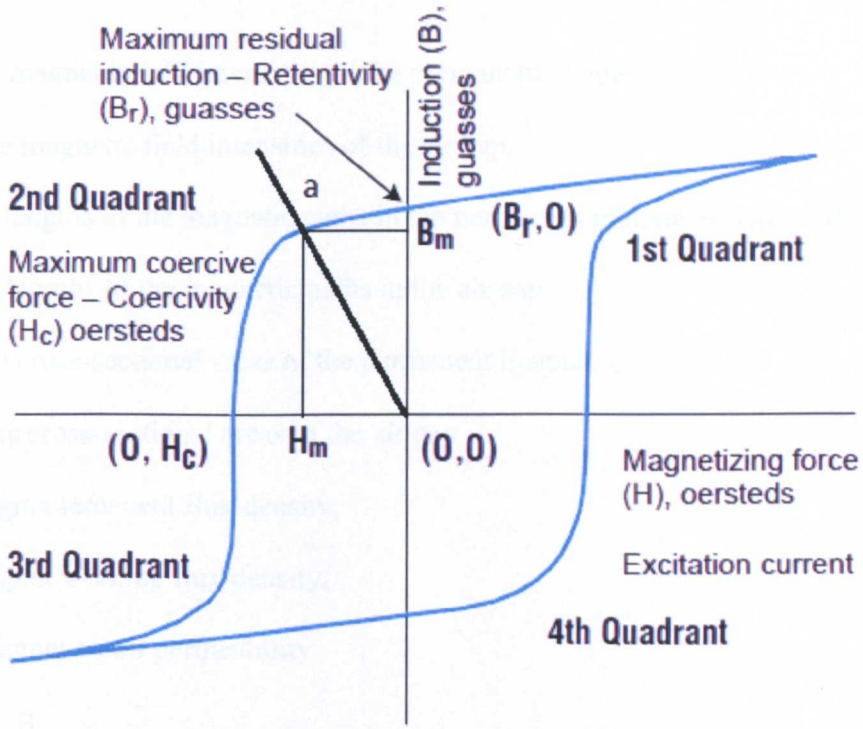

Figure 3-4: Typical demagnetization curves for permanent magnets [50]

In this Figure 3-4, Br is the remanent flux density and Hc is the coercive force. PM motor shall be presented as a series of magnetic circuit in which a permanent magnet, an air gap, and magnetic material of rotor and stator backiron are introduced into a closed magnetic circuit. In the linear magnetic circuit analysis, the flux leakage and fringing are neglected, the permeability of the backiron is assumed to be infinite. The cross-sectional area of the magnet and of the air gap are similar, $A_m = A_{ag}$, meaning that the flux density across such parts are about equivalent, $B_m = B_{ag}$ [5]. With a certain desired airgap flux density B_{ag} at null currents, the magnet radial thickness selected can be calculated by Ampere's circuit law as follows.

$$H_m \cdot l_m + H_{ag} \cdot l_{ag} = 0 \qquad (3.3)$$

Where

H_m: The magnetic field intensities of the permanent magnet

H_{ag} : The magnetic field intensities of the air gap.

l_m : The lengths of the magnetic paths in the permanent magnet or magnet thickness

l_{ag} : The lengths of the magnetic paths in the air gap

A_m : The cross-sectional areas of the permanent magnet

A_{ag} : The cross-sectional areas of the air gap

B_r : Magnet remanent flux density,

B_m : Magnet working flux density,

μ_{rec}, : Magnet recoil permeability

$$H_m \cdot l_m + \frac{B_m}{\mu_o} \cdot l_{ag} = 0 \tag{3.4}$$

$$H_m = -\frac{B_m}{\mu_o} \cdot \frac{l_{ag}}{l_m} \tag{3.5}$$

The equation for the linear section at the second quadrant of the B and H characteristic is

$$B_m = \mu_o \mu_{rec} \cdot H_m + B_r \tag{3.6}$$

$$B_m = -\frac{\mu_o \mu_{rec}}{\mu_o} \cdot \frac{l_{ag}}{l_m} \cdot B_m + B_r \tag{3.7}$$

$$B_r = B_m \cdot (1 + \frac{\mu_o \cdot \mu_{rec} \cdot l_{ag}}{\mu_o \cdot l_m}) \tag{3.8}$$

Rearranging the above equations, it gives that the length of magnet thickness as,

$$l_m \approx \frac{B_{ag} \cdot l_{ag} \cdot \mu_{rec}}{B_r - B_{ag}} \tag{3.9}$$

A graph in Figure 3-5 shows the result for the non-linear magnetic circuit analysis simulated for different magnet thickness at various air gap lengths and flux density which takes into consideration the saturation level of B and H characteristic of the magnetic materials. For an example, a required flux density of 0.7 Tesla at the center of 1mm air gap will need 3mm thickness of permanent magnet. The summary of the linear and non-linear magnetic circuit analysis is tabulated in Table 3-1.

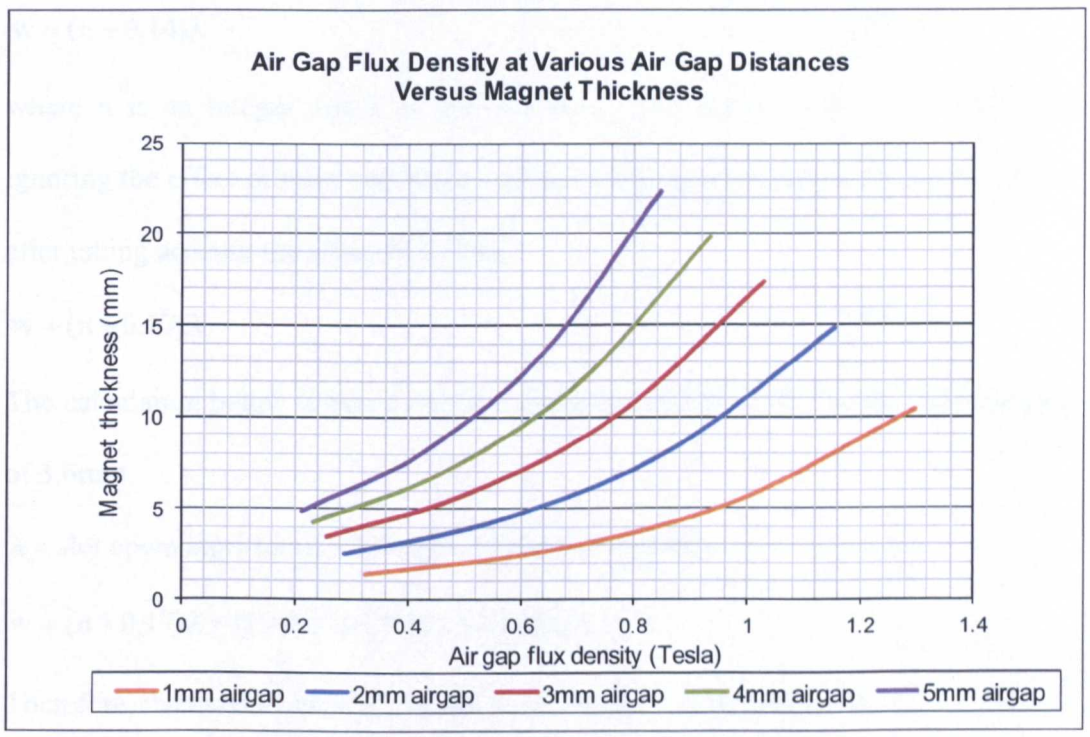

Figure 3-5: Magnet Length for Various Airgap Flux Density

Airgap Length in mm	Magnet Length in mm required for Flux Density of 0.7 Tesla	
	Linear Analysis	Non-linear Analysis
1	2.26	3.0
2	4.51	6.2
3	6.77	9.3
4	9.03	12.2
5	11.00	15.9

Table 3-1: Magnet Length on Linear and Nonlinear Analysis

3.6 Magnet Span

The selection of the magnet span or width is also important in ensuring that the cogging torque level would be minimized [23,25]. Slemon showed that the fundamental sinusoidal component of the cogging torque can be effectively eliminated by an appropriate choice of the magnet width, w, is given as,

$$w = (n + 0.14)\lambda \tag{3.10}$$

where n is an integer and λ is the slot pitch. The above analysis was made by ignoring the effect of rotor curvature and the below equation shows the improvement after taking account the effect of it. [26]

$$w = (n + 0.17)\lambda \tag{3.11}$$

The calculation below is based on the inner stator radius of 43mm and slot opening of 3.6mm.

$$\lambda = \text{slot openning} + \text{tooth} = 3.6\text{mm} + 7.66\text{mm} = 11.26\text{mm}$$

$$w = (n + 0.17)\lambda = (1 + 0.17) \cdot 11.26 = 13.174\text{mm}$$

Therefore, the magnet span, θ_{ms} in electrical degree will be as follows

$$\theta_{ms} = \frac{w \cdot P}{2 \cdot \pi \cdot R_{si}} \cdot 360 \tag{3.12}$$

Where

P : the pair pole number

R_{si} : the inner radius of the motor stator

$$\theta_{ms} = \frac{13.17 \cdot 8}{2 \cdot \pi \cdot 43} \cdot 360 = 140.4^{\circ}$$

The graph in Figure 3-6 shows the result from finite element analysis about the effect of increasing the magnet span with respect to the percentage changed in the produced

average torque. It clearly shows that the produced torque increases less than linearly with the magnet span. This relationship is supported that the fact that the flux density is not increasing with the increase in the magnet span as shown in Figure 3-7.

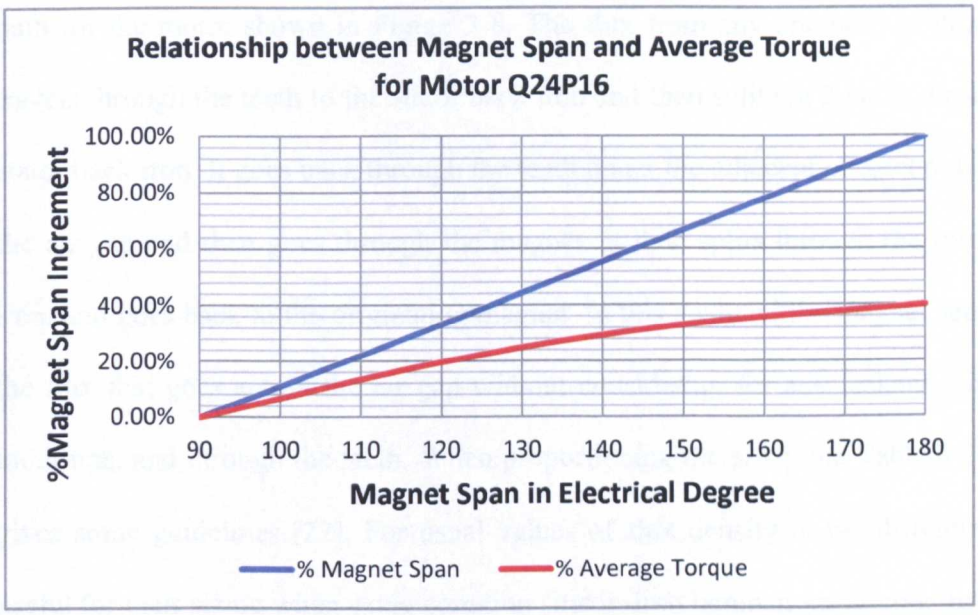

Figure 3-6: The Relationship of Average Torque and Magnet Span

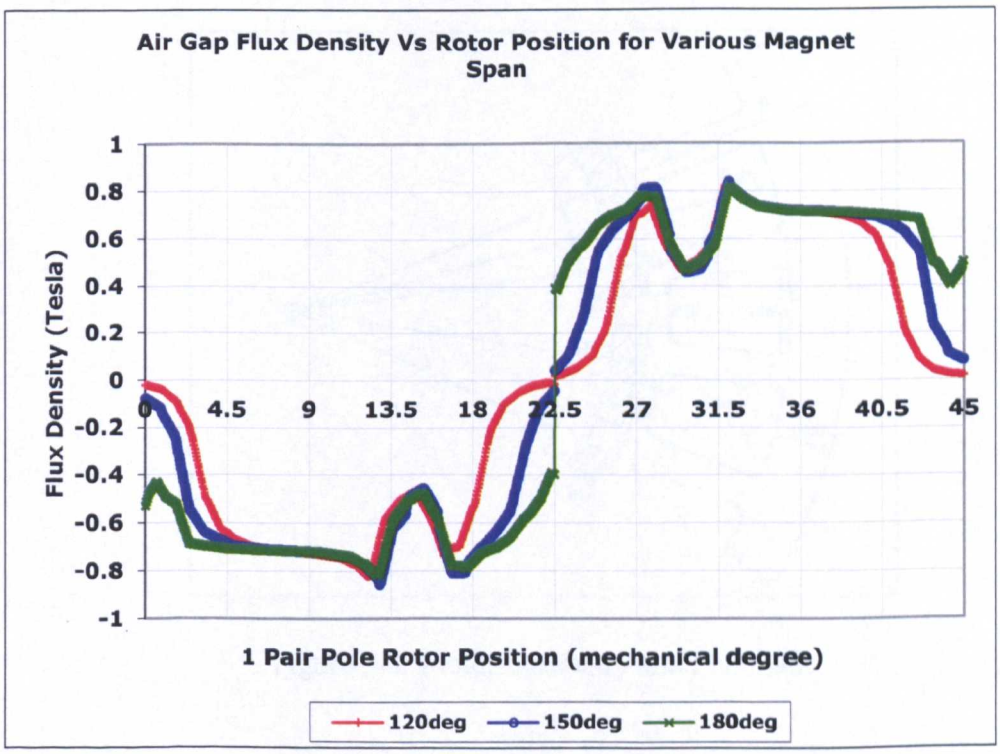

Figure 3-7: Flux Density Distribution at Various Magnet Spans

3.7 Core Geometry

In estimating the size of the respective components, it is necessary to analyze the flux path for the motor shown in Figure 3-8. The flux from any one pole of this motor travels through the teeth to the stator back iron and then splits in 2 paths through the stator back iron. It goes back through the teeth under the adjacent magnet pole across the air gap and then goes through the magnet. It then splits through the rotor back iron, and goes back to the originating magnet. In this analogy, the magnet sets up all the flux that goes across the air gap without considering for any leakages, into the tooth tips, and through the teeth. When proportioning the sizes, the Table 3-2 below gives some guidelines [22]. For usual values of flux density in the different parts, useful for their sizing when using common silicon-iron laminations as core material

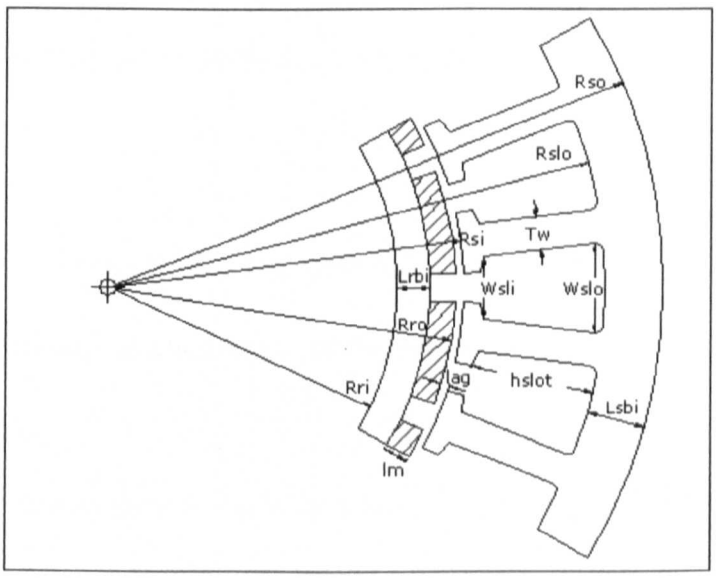

Figure 3-8: Motor Geometry and Flux Path

Magnetic components	Design flux density in Tesla
Stator back iron, Bsbi	1.2
Stator Tooth, Bteeth	1.8
Tooth tip, Bttip	0.9
Rotor back iron, Brbi	1.4

Table 3-2: Guideline for Flux Density Distribution

Note that the flux density is smaller in the stator than in the rotor yoke. This is because the short path of flux in rotor can afford a higher density without resulting in too much MMF drop. Since the flux density is inversely proportional to the area ($B = \frac{\phi}{A}$), and the area is equal to the width of the magnetic-circuit component times the length of the core, the widths may be ratio directly according to the flux density [22]. Below is a sample calculation of the width of the magnetic components of the motor. The width of the stator teeth, T_w, is found by using

$$T_w = \frac{B_{ttip}}{B_{teeth}} \cdot T_{tw} \qquad (3.13)$$

where T_{tw} is the tooth tip width. The tooth tip width, T_{tw}, can be found with certain selected slot opening, slot pitch angle and the radius of the rotor.

$$T_{tw} = \theta_s \cdot R - \cdot w_{slot} \qquad (3.14)$$

where θ_s is slot pitch angle and w_{slot} is the selected slot opening. The stator and rotor back iron are determined as,

$$L_{sbi} = \frac{B_{teeth}}{B_{sbi}} \cdot T_w \qquad (3.15)$$

$$L_{rbi} = \frac{B_{teeth}}{B_{rbi}} \cdot T_w \qquad (3.16)$$

3.8 Number of conductors per slot

In order to decide the number of conductors per slot, the required back EMF induced in the coil shall be determined. The back EMF in a single conductor in the slot shall be determined by two methods. The first method is by determining the rate of flux change versus time i.e Faraday's Law. Alternatively it also can be found by applying Lorentz's force equation [21,24].

method 1: $$e_t = \frac{d\phi}{dt} \qquad (3.17)$$

where

e_t : the induced back EMF in one conductor

ϕ : the effective flux

The above equation will produce the phase back EMF, E_{ph} by multiplying it with the number of turn per phase and the winding factor which will be explained in the next section.

$$E_{ph} = \frac{d\lambda}{dt} = Z_{ph} \frac{d\phi}{dt}$$

Another expression can also be derived for the voltage induced in a conductor moving in a magnetic field. If a conductor of length, L moves at a linear speed v in a magnetic field B, the induced voltage in the conductor is

method 2: $$e = B \cdot L \cdot v = B \cdot L \cdot R \cdot \omega_m \qquad (3.18)$$

where $v = R \cdot \omega_m$ is the linear mechanical speed at the stator bore.

Therefore, the total number of conductors per phase, Z_{ph} shall be determined as follows

$$Z_{ph} = \frac{E_{ph}}{e_t} \quad \text{where } E_{ph} \text{ is the back EMF per phase.} \tag{3.19}$$

and for a slot or a number of conductor per tooth, Z_t will be

$$Z_t = 3 \cdot \frac{Z_{ph}}{N_{slot}} \quad \text{where } N_{slot} \text{ is the total number of slots.} \tag{3.20}$$

since for a phase in a 3-phase system, it will occupy one third of the total number of slots.

3.9 Slot height

Slot area is required to place the coils. Gaps exist between wire turns and the nonuniform shape of the slot will limit the possibility to fill the slot entirely. As a result of this constraint, it is convenient to introduce the slot fill factor as the ratio between conductor cross-sectional area and the slot area [19]. The estimated slot area shall be calculated after knowing the total number of conductors, the conductor cross-sectional area and the expected fill factor.

$$A_{slot} = \frac{A_{cu}}{\text{fill factor}} \tag{3.21}$$

Therefore, by reference to the motor geometry in Appendix C, the slot height is calculated by equating the geometry of the slot area as below,

$$A_{slot} = \left[\frac{\pi}{N_{slot}} (R_{si} + d_{slot} + d_2 + h_{slot})^2 - (R_{si} + d_{slot} + d_2)^2 \right] - T_w \times h_{slot} - A_{slcnt} \tag{3.22}$$

Where,

$\mathbf{A_{slot}}$: the slot area,

$\mathbf{R_{si}}$: the inner radius of the stator

$\mathbf{d_{slot}}$: the tooth tip thickness

$\mathbf{d_2}$: the dimension of the opposite side of the right triangle at tooth tip

$\mathbf{T_w}$: the tooth width

$\mathbf{h_{slot}}$: the slot height

$\mathbf{A_{slcnr}}$: the area at the slot corner

By representing the term $R_{si}+d_{slot}+d_2=\chi$ and rearranging equation 3.22 as a second order quadratic equation,

$$\left[\frac{\pi}{N_{slot}}(\chi+h_{slot})^2-\chi^2\right]-T_w\times h_{slot}-A_{slcnr}-A_{slot}=0 \qquad (3.23)$$

$$\frac{\pi}{N_{slot}}(\chi^2+2\chi h_{slot}+h_{slot}{}^2-\chi^2)-T_w\times h_{slot}-A_{slcnr}-A_{slot}=0 \qquad (3.24)$$

$$\frac{\pi}{N_{slot}}\cdot h_{slot}{}^2+(\frac{2\pi}{N_{slot}}\chi-T_w)\cdot h_{slot}-A_{slcnr}-A_{slot}=0 \qquad (3.25)$$

$$\frac{\pi}{N_{slot}}\cdot h_{slot}{}^2+\left[\frac{2\pi}{N_{slot}}(R_{si}+d_{slot}+d_2)-T_w\right]\cdot h_{slot}-A_{slcnr}-A_{slot}=0 \qquad (3.26)$$

Solve the second order equation and get the solution for the slot height, h_{slot}. Knowing the slot height, the actual available slot area and the winding resistance per phase shall be determined as illustrated in Appendix C.

3.10 Stator winding

The layout of winding in an electric machine affects the MMF distribution and the motor performance. There are an infinite number of possibilities for pole and slot combination as well as for winding layout. Many papers have been reported on describing a procedure for the placement of windings in a motor [22,26-28]. To limit the scope and simplify the choice of winding configuration, the following assumptions are made.

i) The motor is 3-phase

ii) Double layer concentrated winding per slot is used

Below is the basic procedure in selecting the optimum winding layout based on the above assumption [29].

i) Step 1: Mark the coil vectors based on the coil EMF in mechanical degree

ii) Step 2: Rearrange the coil vectors in electrical degree (mechanical degree times pair pole)

iii) Step 3: Group all the coil vectors which are 180 electrical degree phase shift and mark the opposite direction vectors with apostrophe (')

iv) Step 4: Group the vectors into phases (3-phase is 120 degree apart)

Figure 3-9, Figure 3-10 and Figure 3-11 below are the examples of laying and grouping the coil vectors for 3 types of motors.

1) 24 Slots/ 16 Poles (Q24P16)

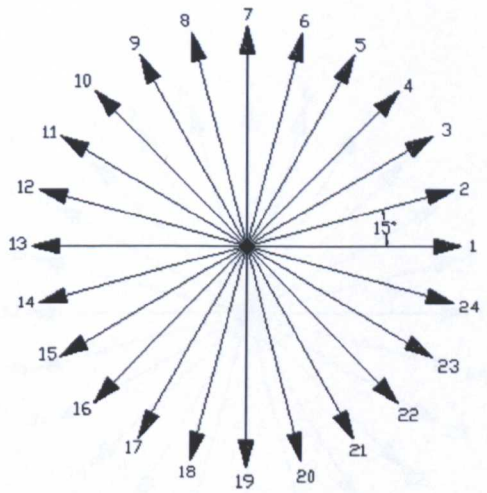

Step 1: Stator coil in mechanical degree

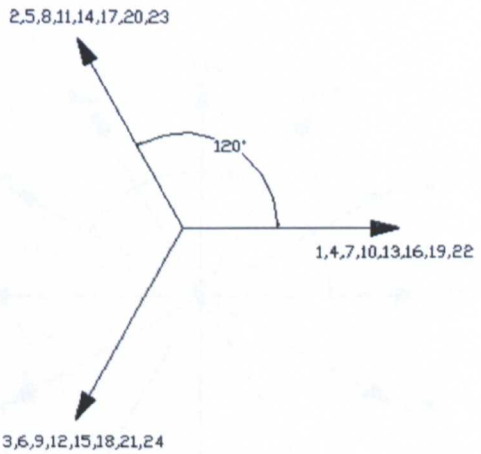

Step 2: Each coil emf in electrical degree

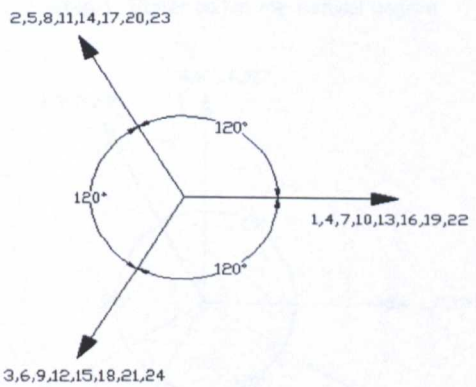

Step 3: Group coils with 180deg phase shift with star configuration

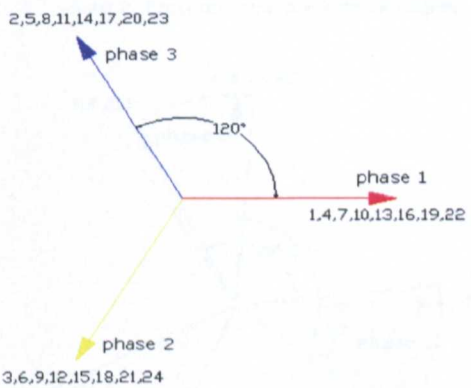

Step 4: Group coils into phases (3-phase 120deg apart)

Figure 3-9: Winding Layout for Q24P16 motor

2) 24 Slots/ 20 Poles (Q24P20)

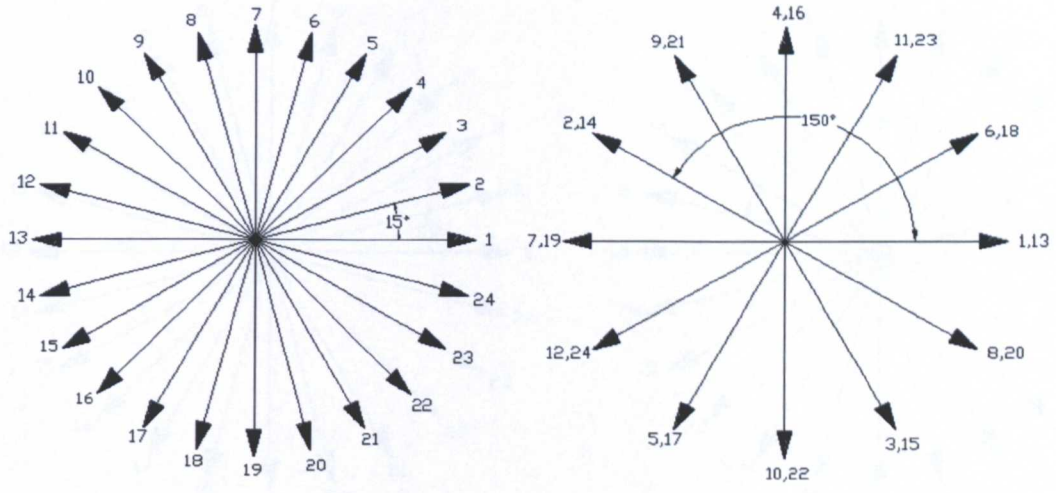

Step 1: Stator coil in mechanical degree

Step 2: Each coil emf in electrical degree

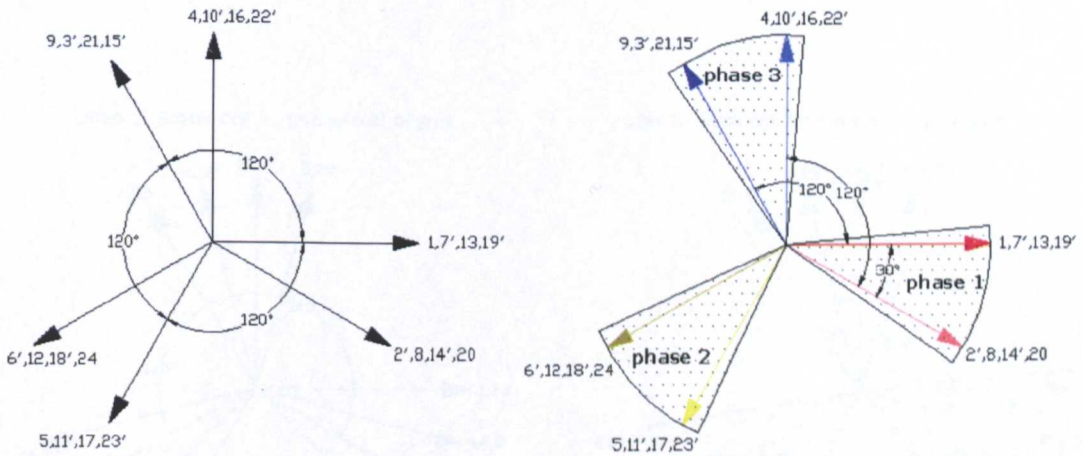

Step 3: Group coils with 180deg phase shift with star configuration

Step 4: Group coils into phases (3-phase 120deg apart)

Figure 3-10: Winding Layout for Q24P20 motor

3) 24 Slots/ 22 Poles (Q24P22)

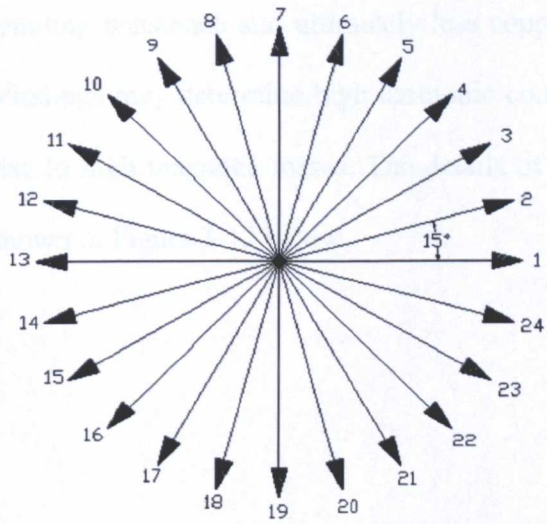

Step 1: Stator coil in mechanical degree

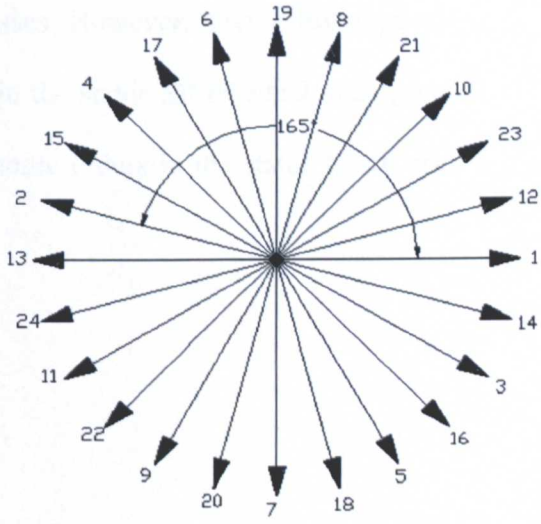

Step 2: Each coil emf in electrical degree

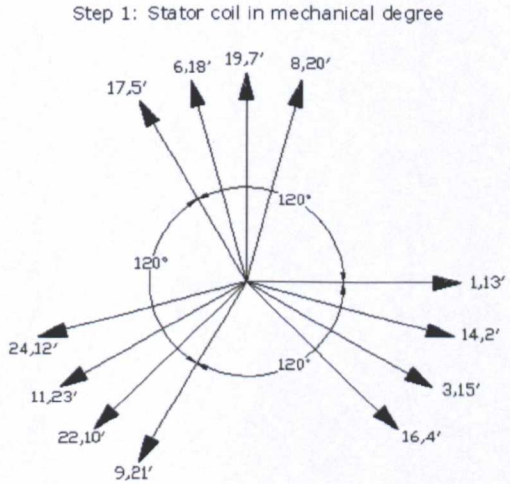

Step 3: Group coils with 180deg phase shift with star configuration

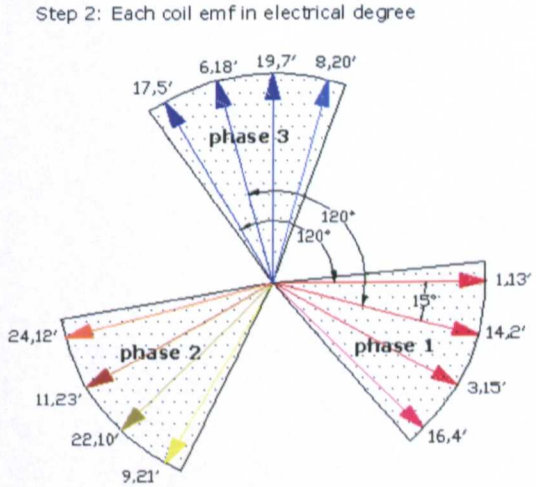

Step 4: Group coils into phases (3-phase 120deg apart)

Figure 3-11: Winding Layout for Q24P22 motor

There are a number of advantages in using concentrated wound which would increase slot fill factor with short end winding length. As a result, it will reduce winding resistance and ultimately less copper losses. However, having this type of windings may determine high harmonic content in the stator MMF which may give rise to high magnetic losses. The details of harmonic orders in the stator MMF are shown in Figure 3-12 below.

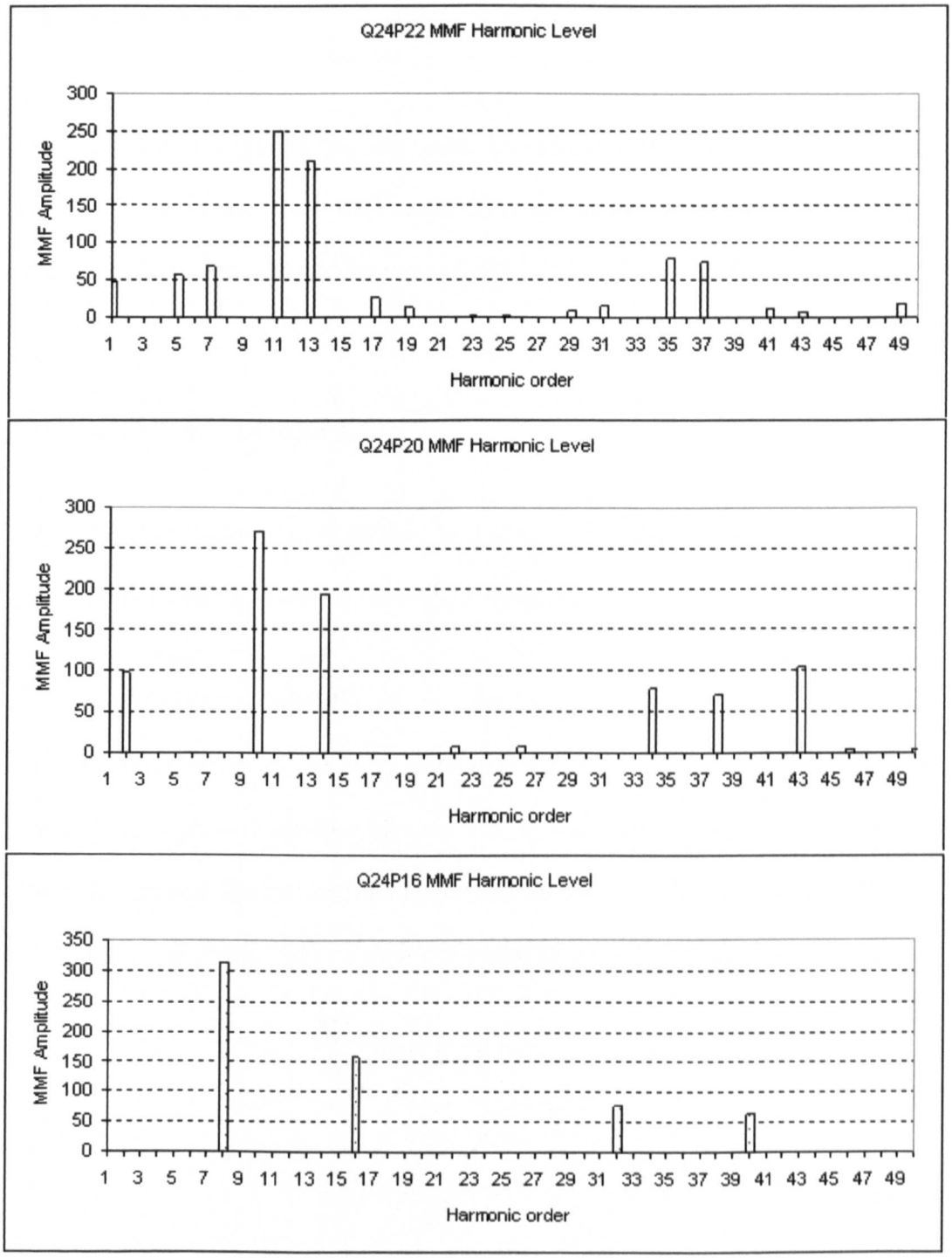

Figure 3-12: Spatial Harmonics Due to Winding Distribution

3.11 Winding Factor

Winding factor consists of two elements, the distribution and pitch factors. Both factors will affect the back EMF induced in the coils [30]. The winding factor calculation illustrated below is for motor Q24P22 (22 poles with 24 slots).

3.11.1 Distribution factor k_{dn}

The distribution factor, k_{dn}, is defined as a ratio of the phasor sum of the coil back EMF with the arithmetic sum of the coil back EMF.

$$k_{dn} = \frac{\text{phasor sum of coil emf}}{\text{arithmetic sum of coil emf}} \tag{3.27}$$

The distribution factor will be unity if the back EMF induced in the coils is in phase such that the angle between two adjacent slots is zero. The distribution factor can be determined graphically by constructing the phasor diagram of the coil back EMF. Let consider the case for the above mentioned motor as shown in Figure 3-13.

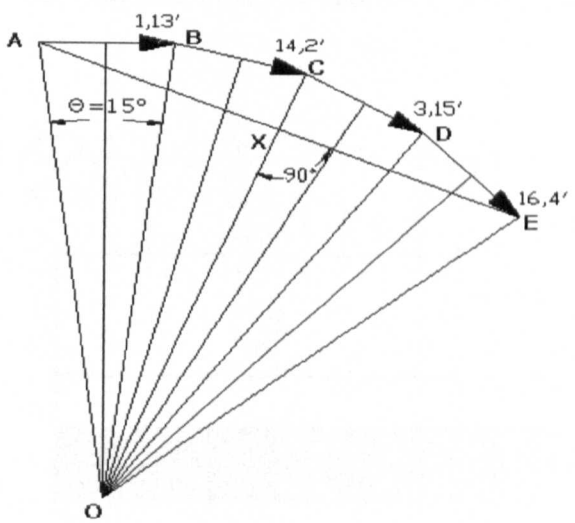

Figure 3-13: Coil EMF Vectors

$$k_{dn} = \frac{AE}{4 \cdot AB} = \frac{2 \cdot AX}{4 \cdot AB}$$

$$= \frac{2 \cdot OA \cdot \sin 4 \cdot \frac{\theta}{2}}{4 \cdot 2 \cdot OA \cdot \sin 4 \cdot \frac{\theta}{2}} = \frac{\sin 4 \cdot \frac{\theta}{2}}{4 \cdot OA \cdot \sin 4 \cdot \frac{\theta}{2}}$$

$$= \frac{\sin 4 \cdot \frac{15}{2}}{4 \cdot OA \cdot \sin 4 \cdot \frac{15}{2}} = \frac{0.5}{0.522} = 0.9577$$

3.11.2 **Pitch factor k_{pn}**

The Pitch factor, k_{pn}, is defined as a ratio of the back EMF induced in an actual coil with the back EMF induced in a full-pitch coil. A coil is called short-pitch when the coil span or slot pitch is less than pole-pitch and as a result the amplitude of the voltage induced is different (typically less) compared with the full-pitch coil. Normally pitch angle is expressed in electrical radians [30].

$$k_{pn} = \frac{\text{back emf in short} - \text{pitch coil}}{\text{back emf in full} - \text{pitch coil}} \tag{3.28}$$

The vector sum of the induced EMF on both of coil sides can be represented as below.

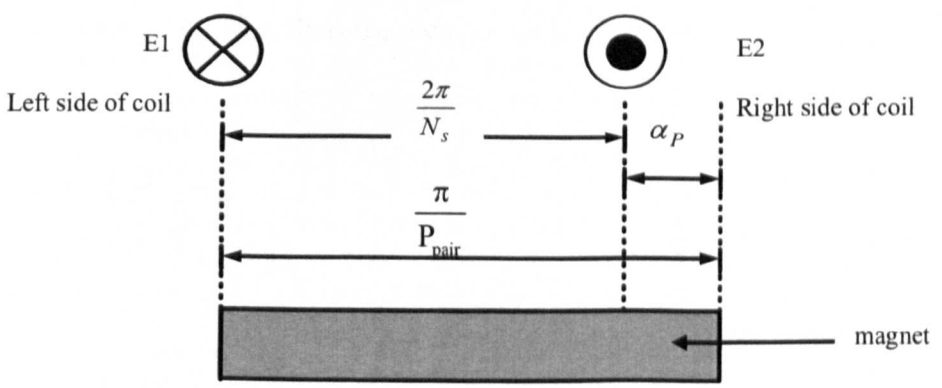

Figure 3-14: Slot Pitch and Pole Span

where $\frac{2\pi}{N_s}$ is Slot pitch and $\frac{\pi}{P_{pair}}$ is pole-pitch/span and by referring to the Figure 3-13 above,

$$\alpha_P = \frac{\pi}{P_{pair}} - \frac{2\pi}{N_S} \tag{3.29}$$

It is clear that the resultant EMF is influenced by the pitch angle, α_P which is defined as the ratio of the resultant vector E_R to the algebraic sum of the individual vectors E_1 and E_2.

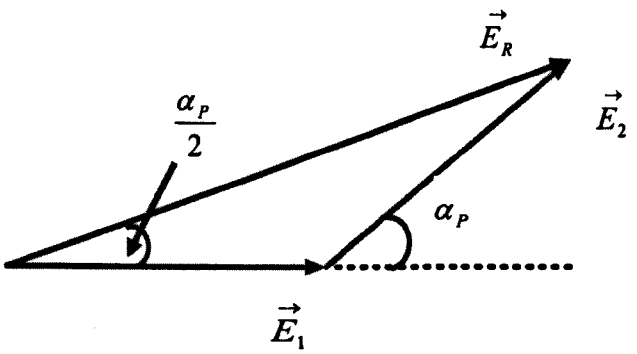

Figure 3-15: EMF Vectors and Resultant

In full-pitch coil the magnitude and phase of vector $\vec{E}_1$ and $\vec{E}_2$ are similar, then the magnitude of $\vec{E}_1 = \vec{E}_2 = E$. Thus the pitch factor is given by:

$$k_{pn} = \frac{\left|\vec{E}_R\right|}{\left|\vec{E}_1\right| + \left|\vec{E}_2\right|} \tag{3.30}$$

$$= \frac{2 \cdot E \cos\frac{\alpha_p}{2}}{2 \cdot E}$$

$$= \cos P_{pair} \cdot \frac{\alpha_p}{2} \text{ (in electrical radian)}$$

$$= \cos(11 \cdot \frac{16.364^\circ - 15^\circ}{2}) = 0.9914$$

Finally the winding distribution is determined as

$$k_w = k_{dn} \cdot k_{pn} \tag{3.31}$$

$$= 0.9577 \cdot 0.9914$$

$$= 0.9495$$

The summary of the winding factor for the analyzed motors are tabulated inTable 3-3.

Motor	Poles	Slots	k_{dn}	k_{pn}	k_w
Q24P16	16	24	1	0.866	0.866
Q24P20	20	24	0.966	0.966	0.933
Q24P22	22	24	0.9577	0.9914	0.9495

Table 3-3: Winding Factor

3.12 Back EMF and Predicted Torque

Once all the parameters have been determined, all the motors are analyzed and simulated using the general purpose analysis programming software and the finite element software, ***Magnet***, in order to predict the magnetic field distribution which will deduce the induced back EMF and the produced electromagnetic torque. Numerous authors have published papers concerning analytical technique in

predicting the open circuit magnetic field distribution in brushless permanent magnet motors with surface mount magnet [31-32]. A detail analysis example for motor Q24P20 is shown in Appendix D with assumptions that the stator is smooth, slotting effect is not taken into account, iron has an infinite permeability, the relative permeability of the magnet is assumed to be unity when computing the field due to the winding, magnets have radial edges and polar coordinates are used.

The Figure 3-16, Figure 3-17 and Figure 3-18 below show all the back EMF induced per coil when the motors are simulated in open circuit. All the 3 motors are producing the 120 degree phase shift on the induced back EMF, however only a motor with 16 poles combination is producing the waveform that match the trapezoidal back EMF. The type of current waveform will significantly increase the machine average torque when three phase current waveforms matching in full the trapezoidal back EMF are supplied [34]. However, the value of the induced back EMF of the above mentioned motor is directly affected by the winding factor of the motor [30]. The results for the average predicted and cogging torques are presented in Figure 3-19 and Figure 3-20. In general, the predicted torque produced in all analyzed motor are close to the specification, however further analysis on losses is necessary in order to gain the optimum parameters.

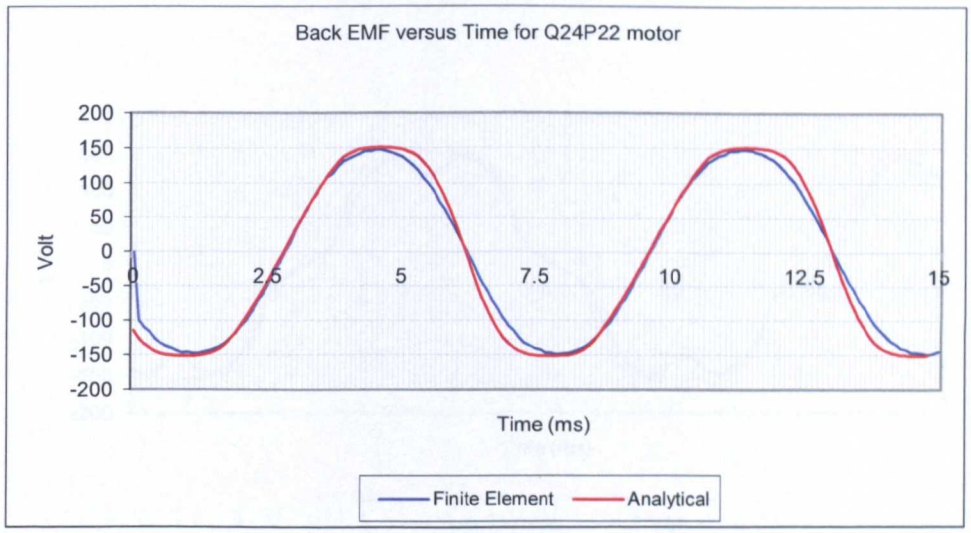

Figure 3-16: Back EMF for Q24P22

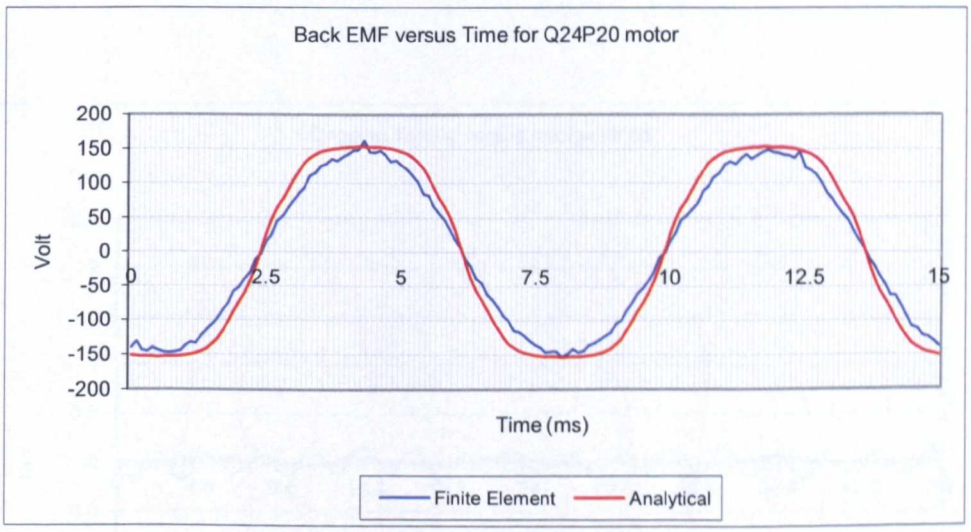

Figure 3-17: Back EMF for Q24P20

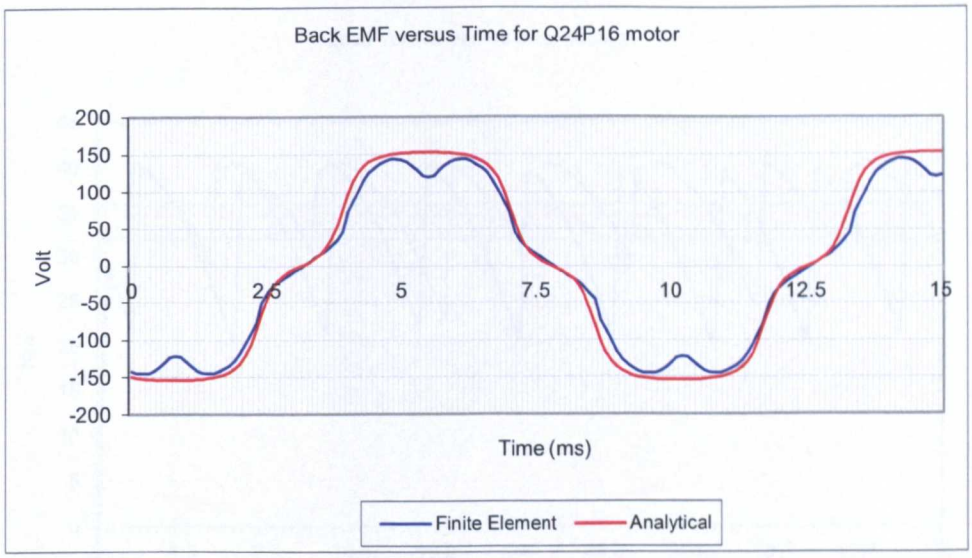

Figure 3-18: Back EMF for Q24P16

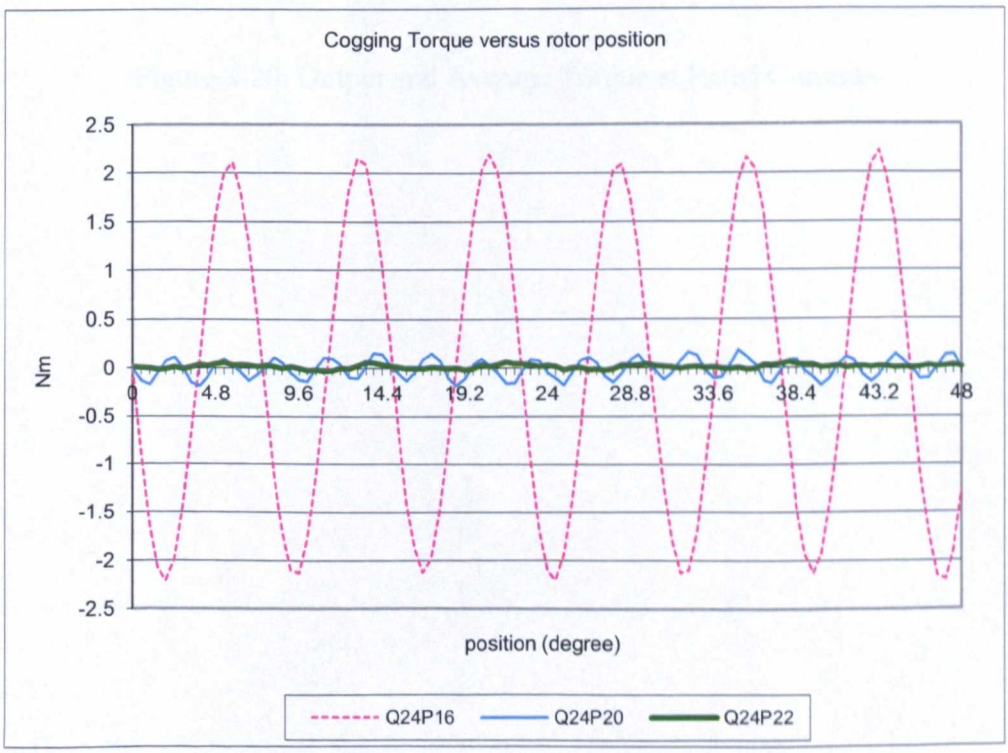

Figure 3-19: Cogging Torque at Null Currents

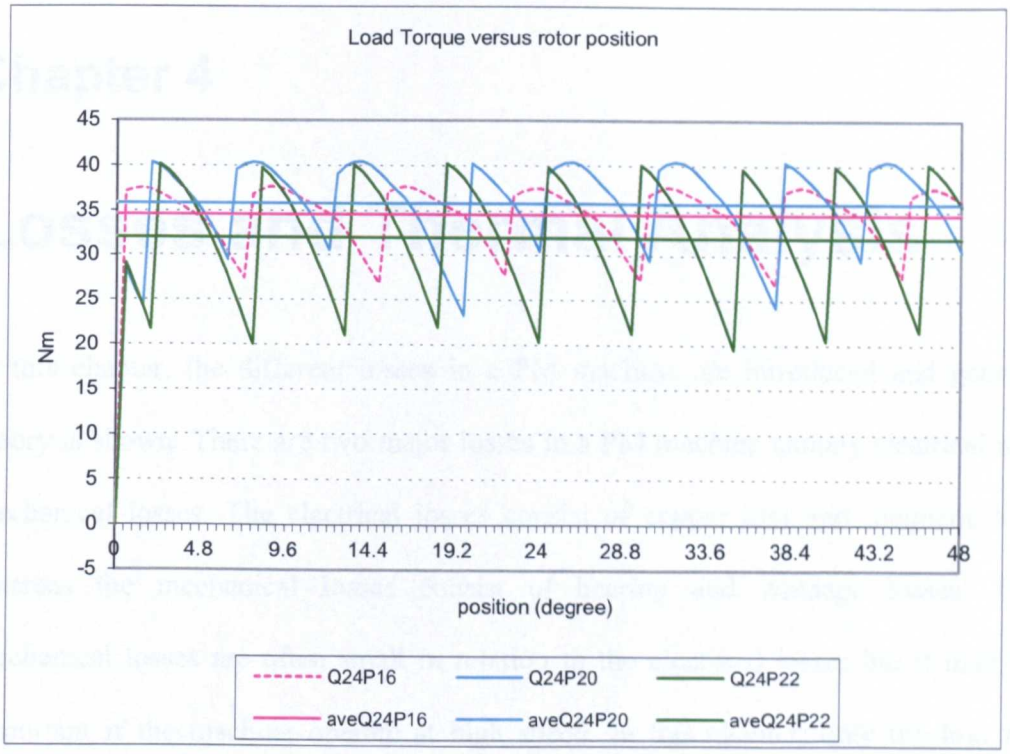

Figure 3-20: Output and Average Torque at Rated Currents

Chapter 4

Losses and Thermal Analysis

In this chapter, the different losses in a PM machine are introduced and general theory is shown. There are two major losses in a PM machine namely electrical and mechanical losses. The electrical losses consist of copper loss and magnetic loss whereas the mechanical losses consist of bearing and windage losses. The mechanical losses are often small in relation to the electrical losses but it may be important if the machine operate at high speed. In this chapter, only the loss for PMSM is analysed and compared with experimental results as the drive for BLDC is still under construction.

4.1 Copper loss

The copper loss often contributes the largest portion of the total losses in a PM machine. The copper loss in a 3 phase PM machine is calculated as follows:

$$P_{cu} = 3 \cdot I^2 \cdot R_a \qquad (4.1)$$

where R_a is the winding resistance of one phase and I is the rms value of the stator current. The winding resistance per phase is depending on the total length of conductor per phase and conductor area as shown in Equation 2.39. The conductor area is a product of the slot area, A_{slot}, and the slot fill factor, S_{ff}, as shown in Equation 4.2. A high slot fill factor will consequently reduce the copper loss.

$$R_a = \frac{L_{cu}}{\sigma \cdot S_{ff} \cdot A_{slot} \cdot str \cdot Ph} \quad (4.2)$$

Below is the comparison between the simulated and experimental results which varied substantially as the load torque is increasing. Any increase on the load torque will require higher current which will definitely contribute on the thermal loss on the winding. This thermal loss will increase the value of the winding resistance and as a result will proportionally increase the amount of the copper loss.

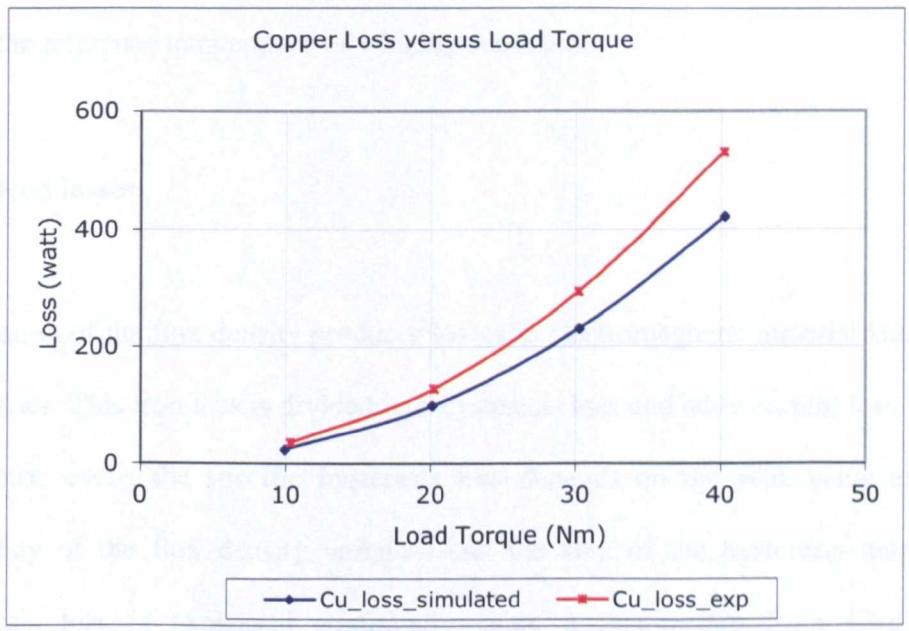

Figure 4-1: Copper losses at various torque level for PMSM

The thermal loss will generate heat and increase both the temperature of the motor winding and its resistance. The value of the winding resistance at any temperature other than the standard temperature (usually specified at 20 Celsius winding conductors) shall be determined through the following equation.

$$R = R_{ref}[1 + \alpha(T - T_{ref})] \quad (4.3)$$

Where,

R: the winding conductor resistance at temperature in Celcius,

Rref: the winding conductor resistance at reference temperature which is usually 20°C.

The alpha constant, **α**: is the temperature coefficient of winding conductor material expressing the resistance change factor per degree of temperature change. The material used is copper and has a temperature coefficient value of 0.00393/°C.

T: the winding conductor temperature in degree Celcius and

Tref; the reference temperature of winding conductor

4.2 Iron losses

A variation of the flux density produces losses in electromagnetic material known as iron losses. This iron loss is divided into hysteresis loss and eddy current loss. In the symmetric cycle, the specific hysteresis loss depends on the peak value and the frequency of the flux density variation and the area of the hysteresis loop. The hysteresis loss is expressed empirically using a relationship from Charles P. Steinmetz as:

$$P_h = k_h \cdot B^{\beta} \cdot f \qquad (4.4)$$

Where k_h is hysteresis constant, β is the Steinmetz constant which depends on the magnetic material used.

The eddy currents loss depends on the time rate of change of the flux density [24]. The eddy currents are circulating currents that are induced in the iron core by the magnetic field around the turns of the coil. For any given core, this loss is proportional to the frequency, the maximum flux density, and the conductivity of the core. The dependence of eddy current loss on flux density and frequency is expressed as below.

$$P_e = k_e \cdot B^2 \cdot f^2 \qquad (4.5)$$

Measurements of iron losses in magnetic material are traditionally made under sinusoidal flux density, varying frequency and magnitude. The total volumetric iron losses are commonly expressed in the following form for sinusoidally varying magnetic flux density.

$$P_{iron} = P_h + P_e = k_h \cdot B^{\beta} \cdot f + k_e \cdot B^2 \cdot f^2 \qquad (4.6)$$

All constants depend on the magnetic material. Typical values for grades of silicone iron laminations used in small and medium machines with the frequency in radians per second are in the ranges as below [24]; k_h = 40-55, β= 1.8-2.2 and k_e = 0.04-0.07

4.3 Verification of the iron losses

The machine geometry is exported from AutoCAD into finite element software, Magnet. In Magnet, the different machine parts are assigned a specific material. In a magnetic simulation, the non-magnetic materials are represented as air. The magnet material is created in order to describe the required remanence flux density. The selected iron material is created in the material database. There are two types of simulations namely magneto-static and transient analysis. Magneto-static is used for calculation of the flux density created by the magnets and transient analysis is used for calculations of the torque and the iron losses at rated speed.

For the transient simulation, a circuit is used in order to impose the currents waveforms for a specific torque as shown in Figure 4-2.

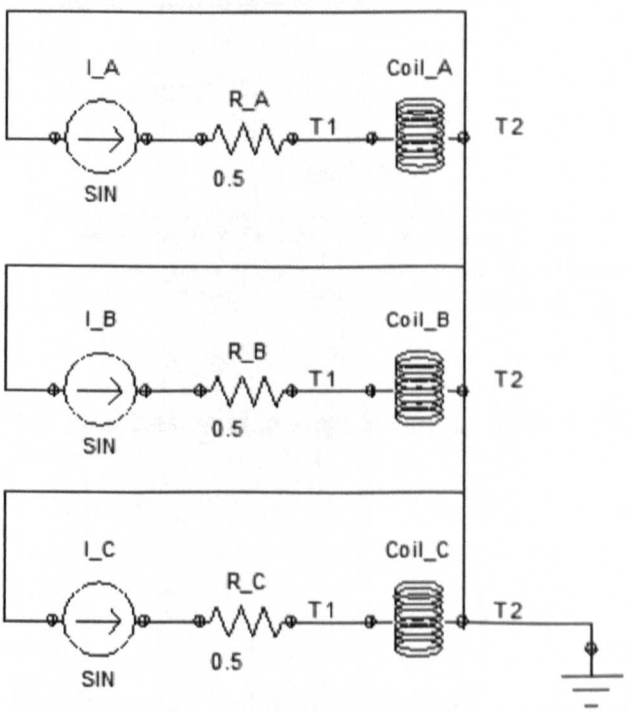

Figure 4-2: Circuit schematic for Transient Analysis for PMSM

The resistance of each coil is calculated from the phase resistance which represents the total resistance of one phase. The coil resistances are therefore given by the phase resistance divided by the pole number. Note that this is valid only for this specific winding arrangement.

The machine is simulated at rated speed and torque. The FE model is used to calculate the iron losses in the stator and the rotor core. The results obtained by the FE model used during the design process and the FEM calculations are presented in Figure 4-3. As expected, the rotor core losses are very small.

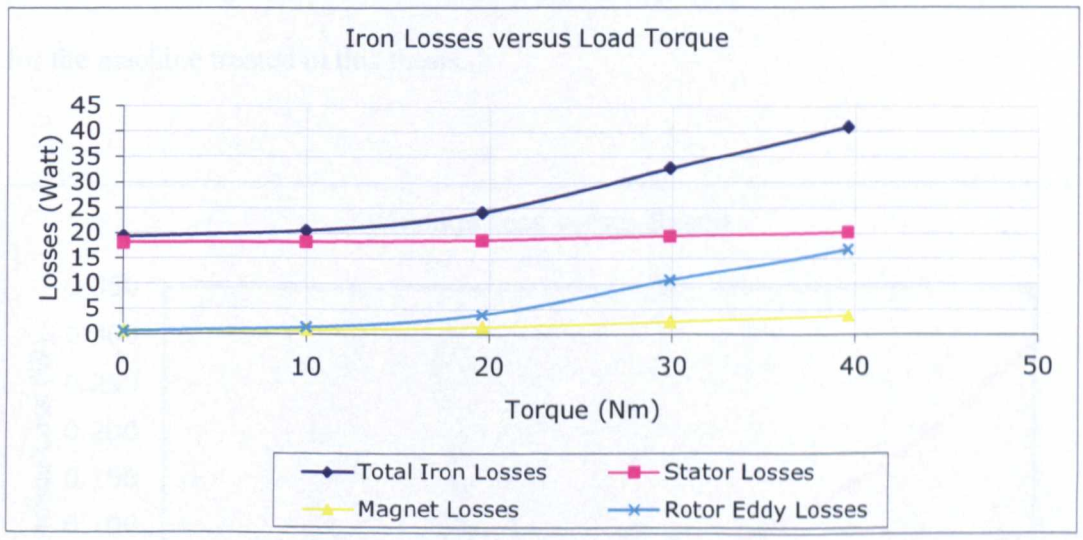

Figure 4-3: Iron losses component at various loads for PMSM

4.4 Windage

Windage loss is a loss due to friction between the air and the rotor surface. If the rotor surface area is small, this loss is negligible at moderate rotational speeds.

Gieras and Wang provide an analytical equation for the windage loss in a small machine that doesn't have an internal fan as below [25].

$$P_{windage}=2\times D_{ro}^{3}\times L\times N^{3}\times 10^{-18} \quad (4.7)$$

Where, D_{ro} is the outside rotor diameter (mm), L is the length of rotor core (mm) and N is the motor rotational speed (revs/min).

The above relationship gives a good indication of the approximate expected loss and is described in Figure 4-4. It is noted that the windage loss can be consider negligible for the machine treated in this thesis.

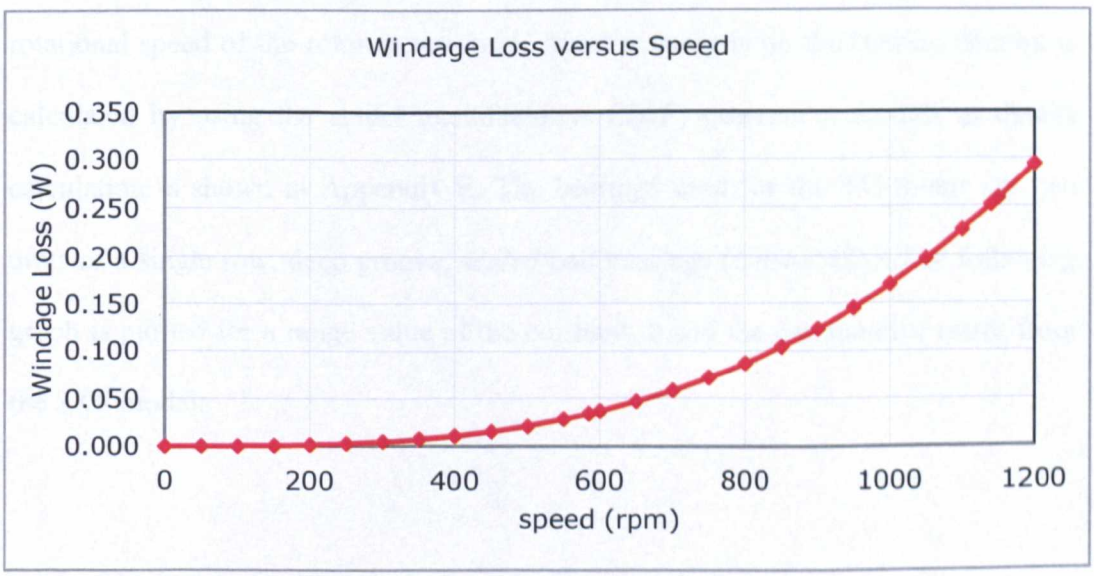

Figure 4-4: Windage losses at various speeds for PMSM

4.5 Bearing

The bearing loss is depending on many factors, such as bearing type, lubrication, shaft load and rotor speed. The friction torque of a bearing is quite complex to calculate if high accuracy is required, but for an estimation it can be done rather easily. In literature, different formulas can be found of varying complexity, for example, Gieras and Wing provide an analytical equation for the expected bearing losses [25]:

$$P_{bearing} = \frac{k \cdot M_{rot} \cdot N}{1000} \tag{4.8}$$

where, k is a constant between 1 and 3, M_{rot} is a mass of rotor in kg and N is the rotational speed of the rotor in revs/min. Another analysis on the bearing friction is calculated by using the actual manufacturers (***SKF***) power-loss models as details calculation is shown in Appendix E. The bearings used for the PM motor are two units of a single row, deep groove, *sealed* ball bearings (*6004-2RSL*). The following graph is plotted for a range value of the constant, k and the comparative result from the SKF model.

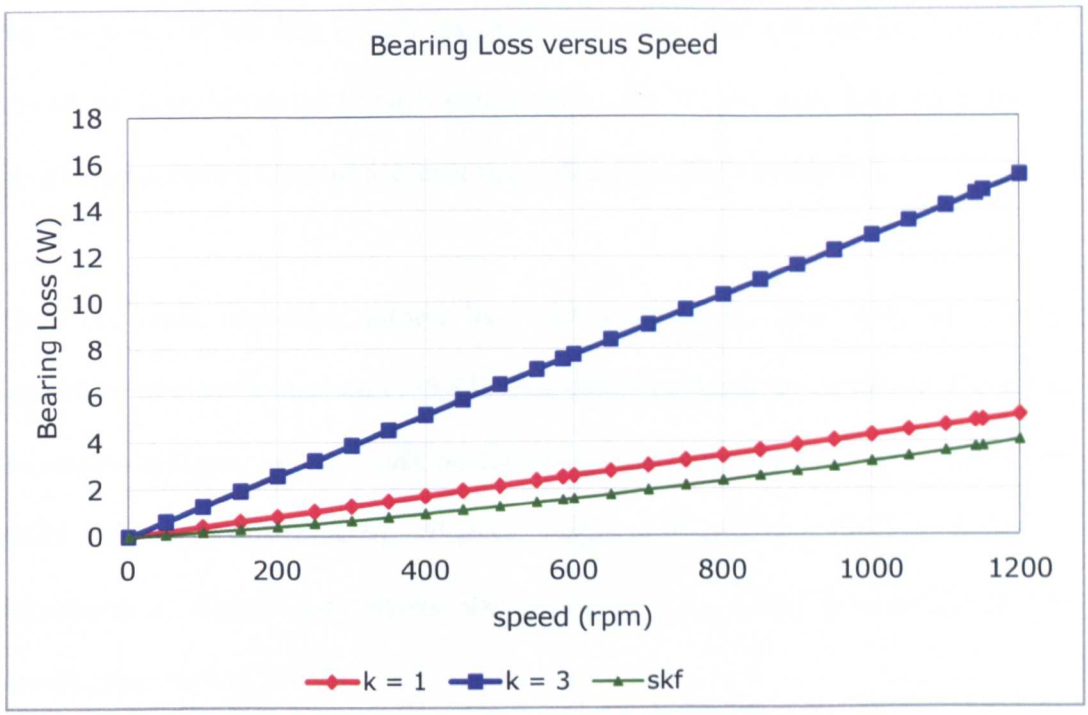

Figure 4-5: Bearing Losses as predicted by Gieras and Wing

From Figure 4-5 above, it can be noticed that there is a great discrepancy in predicting the bearing losses between the analytical equation and the actual manufacturer power-loss model. Gieras and Wing's analytical equation is significantly over predicted and there is no recommendation of a suitable "k" value should be used. Thus, the prediction loss from the manufacturer, SKF, will be obviously used throughout this thesis.

4.6 Thermal Model and Analysis

The main objective of performing detailed thermal analysis of a motor is to predict and determine the individual motor component temperatures, both under steady state and transient conditions. An accurate determination of temperatures, in particular, for

the magnets and winding is very important since the efficiency and life time of the motor are directly related to such temperatures. In this research, such temperatures should not exceed the permitted level that will be reported in chapter 6.

Over the years, numerous authors have published papers concerning the thermal modelling of electric machines [35-43]. The thermal analysis of an electric motor can be carried out using two methods; analytical lumped parameters analysis or FEM and CFD analysis. In this research, a thermal design package Motor-CAD is used in the investigation. Figure 4-6 shows the geometry and actual parameters of the investigated motor Q24P20.

Radial XSect | Axial XSect | Winding | Input Data

Housing:	Axial Fins (Rd)	Mounting:	Flange
Slot Type:	Parallel Tooth	BPM Rotor:	Surface Radial
Stator Ducts:	None	Rotor Ducts:	Shaft Spoke

Stator Dims.	Data	Rotor Dims.	Data
Slot Number	24	Pole Number	20
Housing Dia	154	Magnet Thickness	5.99
Stator Lam Dia	134	Magnet Arc (ED)	136.5
Stator Bore	95	Magnet Segments	1
Tooth Width	5.62	Airgap	1
Slot Depth	15	Banding Thickness	0
Slot Corner Radius	2	Shaft Dia	25
Slot Opening	2.5	Shaft Hole Diameter	6
Tooth Tip Depth	2	Number Shaft Spokes	5
Tooth Tip Angle	15	Spoke Radial Depth	17
Sleeve Thickness	0	Spoke Thickness	6
Fin Extension	15		
Fin Thickness	3		
Fin Pitch/Thick	4		
Fin Pitch [Calc]	12		
Corner Cutout [%]	0		
Plate Height	170		
Plate Width	170		

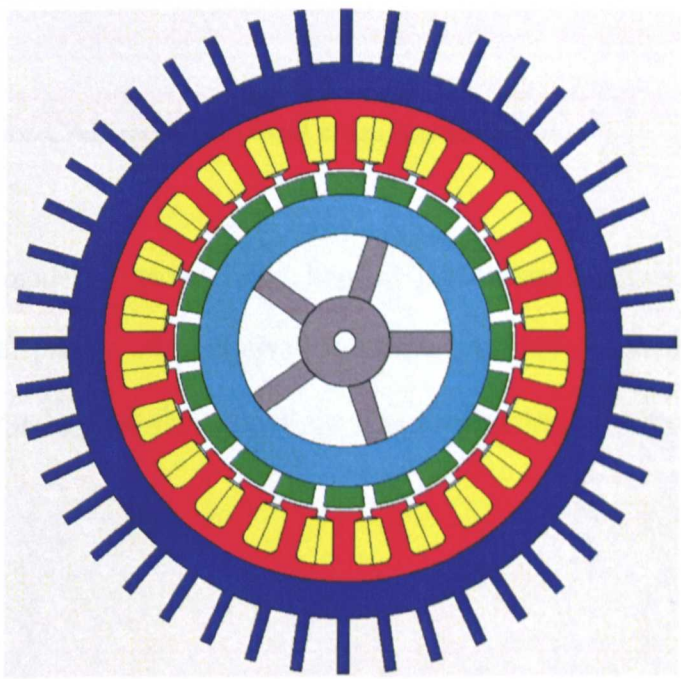

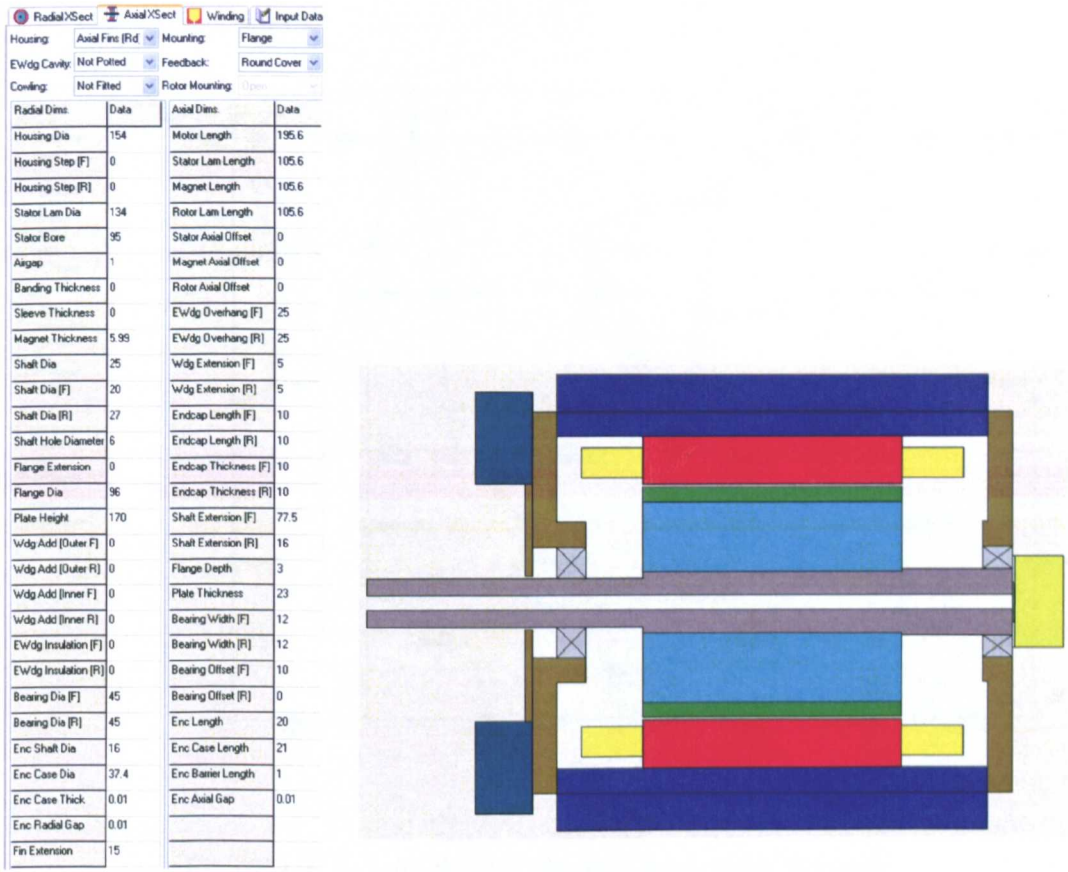

Radial XSect | Axial XSect | Winding | Input Data

Housing:	Axial Fins (Rd	Mounting:	Flange
EWdg Cavity:	Not Potted	Feedback:	Round Cover
Cowling:	Not Fitted	Rotor Mounting:	

Radial Dims:	Data
Housing Dia	154
Housing Step [F]	0
Housing Step [R]	0
Stator Lam Dia	134
Stator Bore	95
Airgap	1
Banding Thickness	0
Sleeve Thickness	0
Magnet Thickness	5.99
Shaft Dia	25
Shaft Dia [F]	20
Shaft Dia [R]	27
Shaft Hole Diameter	6
Flange Extension	0
Flange Dia	96
Plate Height	170
Wdg Add [Outer F]	0
Wdg Add [Outer R]	0
Wdg Add [Inner F]	0
Wdg Add [Inner R]	0
EWdg Insulation [F]	0
EWdg Insulation [R]	0
Bearing Dia [F]	45
Bearing Dia [R]	45
Enc Shaft Dia	16
Enc Case Dia	37.4
Enc Case Thick	0.01
Enc Radial Gap	0.01
Fin Extension	15

Axial Dims:	Data
Motor Length	195.6
Stator Lam Length	105.6
Magnet Length	105.6
Rotor Lam Length	105.6
Stator Axial Offset	0
Magnet Axial Offset	0
Rotor Axial Offset	0
EWdg Overhang [F]	25
EWdg Overhang [R]	25
Wdg Extension [F]	5
Wdg Extension [R]	5
Endcap Length [F]	10
Endcap Length [R]	10
Endcap Thickness [F]	10
Endcap Thickness [R]	10
Shaft Extension [F]	77.5
Shaft Extension [R]	16
Flange Depth	3
Plate Thickness	23
Bearing Width [F]	12
Bearing Width [R]	12
Bearing Offset [F]	10
Bearing Offset [R]	0
Enc Length	20
Enc Case Length	21
Enc Barrier Length	1
Enc Axial Gap	0.01

Figure 4-6: Motor-CAD radial and axial cross section editor

The Motor-CAD thermal model is based upon lumped parameters analysis. It represents the thermal problems by using equivalent thermal resistance networks which shows a detailed thermal circuit showing all the heat flow paths in the motor as shown in Figure 4-7.

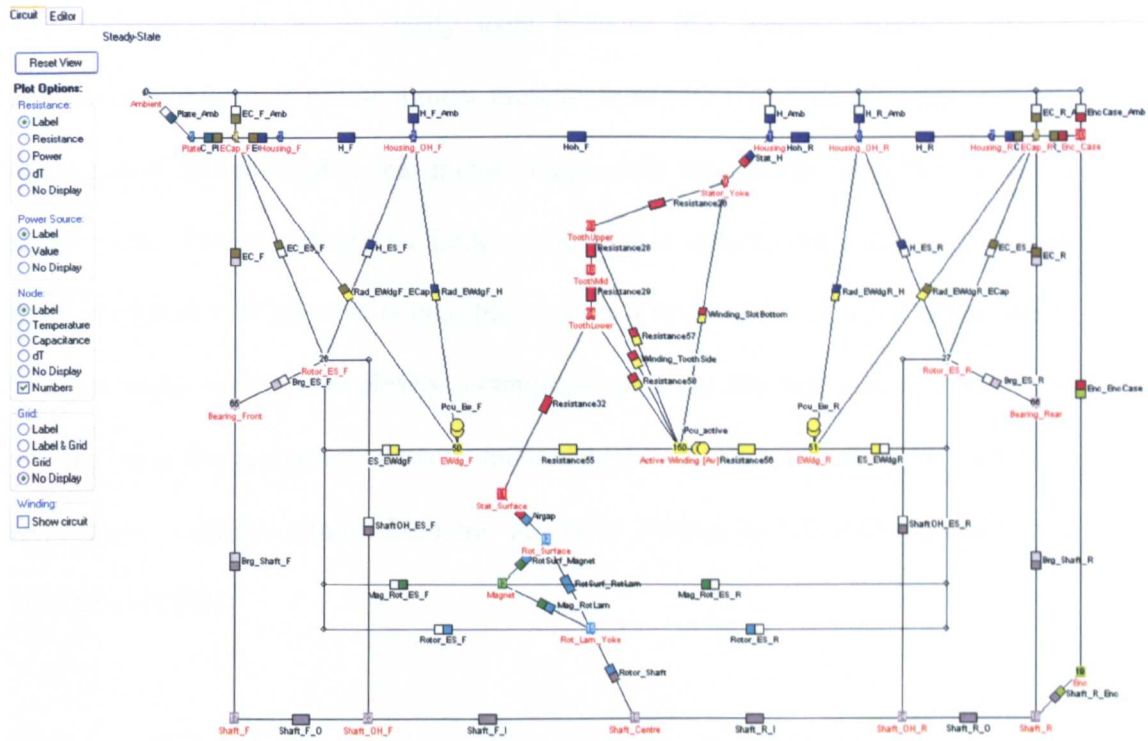

Figure 4-7: Schematic of a Thermal Resistance Network

Briefly in this technique the electrical machine is divided geometrically into a number of lumped components and each component represents a node which will have a bulk thermal storage and heat generation. The lumped parameters are derived from entirely dimensional information, the thermal properties of the materials used in the design and constant heat transfer coefficients. The thermal circuit in the steady state consists of thermal resistances and heat sources such as winding, bearing, windage, etc. are connected between motor component nodes to represent heat pathways. For transient analysis, the heat/thermal capacitances are used in representing thermal inertia. By representing the entire motor as a lumped thermal circuit, it is possible to evaluate the significant temperatures to a reasonable degree of accuracy.

The resistance network is vastly used because this method requires minimal computing power thus giving almost immediate results (for a simple analysis). The drawback of this method is that motor components are usually modelled by only a single node. To have achieved better simulated accuracy, one must increase the number of nodes. While this is possible, one must be aware of this procedure due to the increasing system complexity, computational time and processing power. The alternative to the resistance network method is the utilization of more sophisticated techniques, namely: Finite Element Analysis (FEA) and Computational Fluid Dynamics (CFD).

FEA can only be used to model conduction heat transfer in solid components, while CFD is able to model all heat transfer mechanisms (conduction, convection and radiation). CFD is primarily used in the thermal design of motors since it has the capability to predict complex flow regimes as well as heat transfer [39, 44-45]. CFD techniques solve a set of coupled, second order, non linear partial differential equations which satisfy the momentum, energy and continuity equations. On the contrary to the resistance network, CFD techniques demand far greater computing power, and are much more time consuming. Thus, it is common practice to model particular regions of a machine rather than model the entire motor. The data obtained from these analyses can then be used as input data for a lumped parameters analysis of the machine as a whole [39].

4.7 Thermal Analysis Set-up

The objective of the conducted experiments is to be able to determine not only all of the interesting temperatures, both of the rotor (Shaft, Rotor, Magnet) and of the stator components (Housing, End Winding, End Space, Flange) of the motor, but also to compare with the results provided by the dedicated software named MotorCAD. Temperature acquisition is obtained by means of thermocouples and a rotating data logger which will capture the identified components' temperature while the motor is rotating.

There isn't any problem in obtaining the temperatures for the stationary parts of the motor but some design and modification required for measuring the temperatures on the rotating parts. For that reason, an additional system (logger casing and end plate) was later attached to the motor shaft. A miniature 4 - channel data logger was purchased from OMEGA and inserted into a cylindrical casing. Three K - Type thermocouples were then attached to the internal rotating surfaces by means of a thermally-conductive, but electrically-insulated adhesive and then passed through the hollow motor shaft and attached to the data logger. An end plate was also machined so as to align the logger casing with the torquemeter coupling. However, this required to re-balance the motor due to the asymmetry of the introduced system. The images below explain better how the system capturing the data of the rotating parts was implemented.

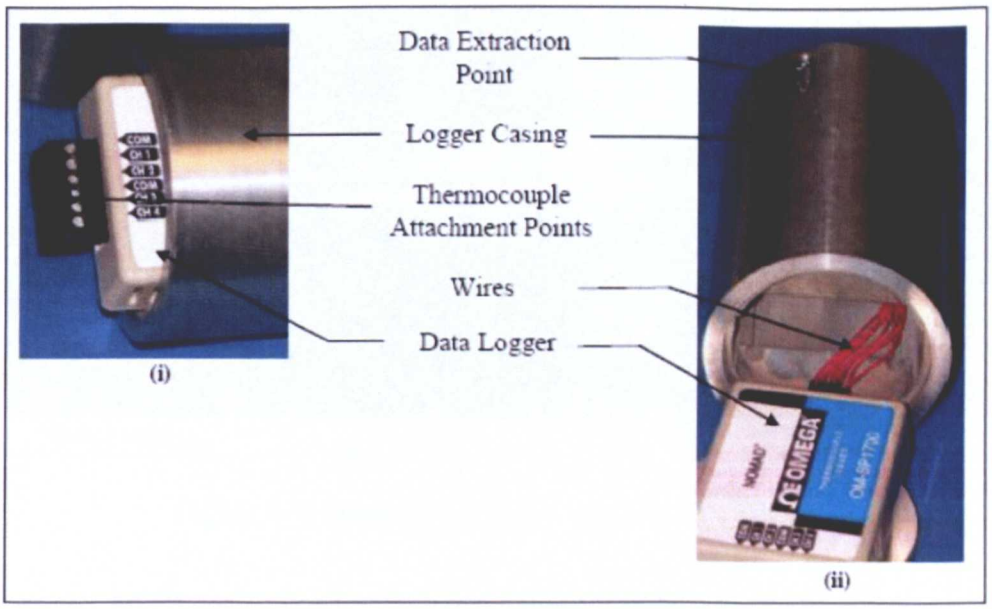

Figure 4-8 (i) 4 – Channel OMEGA Data Logger together with a Casing (ii) Data Logger showing port extension

For ease of data acquisition, the connection point on the data logger is reproduced and extended to the cylindrical surface of the logger casing as shown in Figure 4-8. This meant that after each test, the data is obtained by attaching the cable to the plug on the outside, rather than dismantling the entire system to obtain the original logger connection point. Thus, by setting up the apparatus in this manner, a lot of time was saved and furthermore loss of accuracy was avoided (since no dismantling of the entire system is required after each run).

The Figure 4-9 below represents the geometrical location of each of the three thermocouples. While Thermocouple 1 leads directly into the centre of the magnet, Thermocouples 2 and 3 are affixed to the rotor at a shallow grove and a rotor spoke respectively.

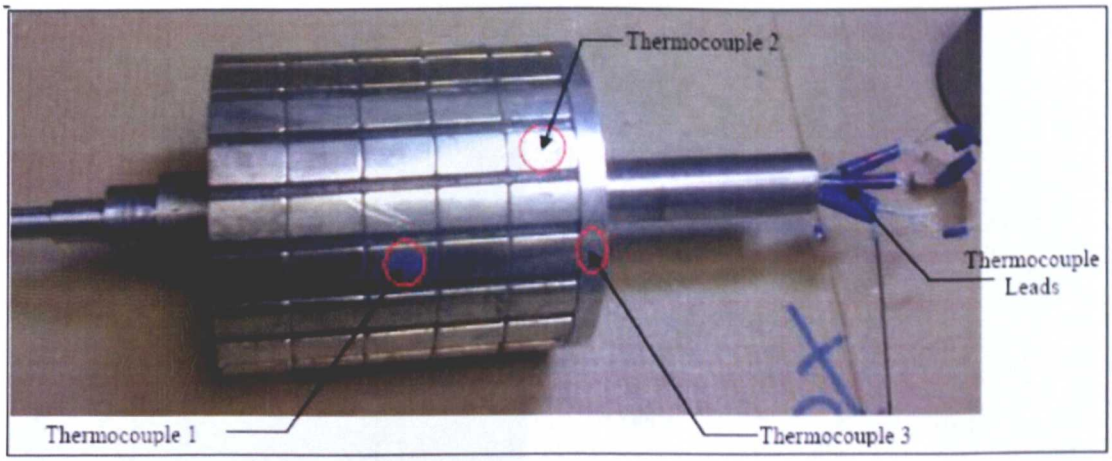

Figure 4-9: Permanent Magnets affixed to PMSM's rotor

The reason for the above thermocouple set up is simply to ascertain whether a temperature gradient exists in the radial direction of the rotor. The reasoning behind this thought is because the rotor is spoke-shaped as shown in Figure 5-6 and thus, it is possibly that there will be a greater heat flow across the spoke rather than in the rotor space. Thus the difference between the measurements logged by Thermocouples 2 and 3 will give the temperature gradient, and by comparing the respective values, and could conclude if the temperature gradient across the rotor is significant. As mentioned earlier, in MotorCAD, the individual motor components are represented by a single node. Thus by the above thermocouple setup, we can further deduce how far off the results supplied by MotorCAD are from the actual experimental data.

As mentioned earlier, for the stator a stationary 8 - channel high resolution Comark data logger is used to capture temperature readings of the end winding as well as for different locations on the housing namely front, middle, rear as well as fin tip as shown in Figure 4-10.

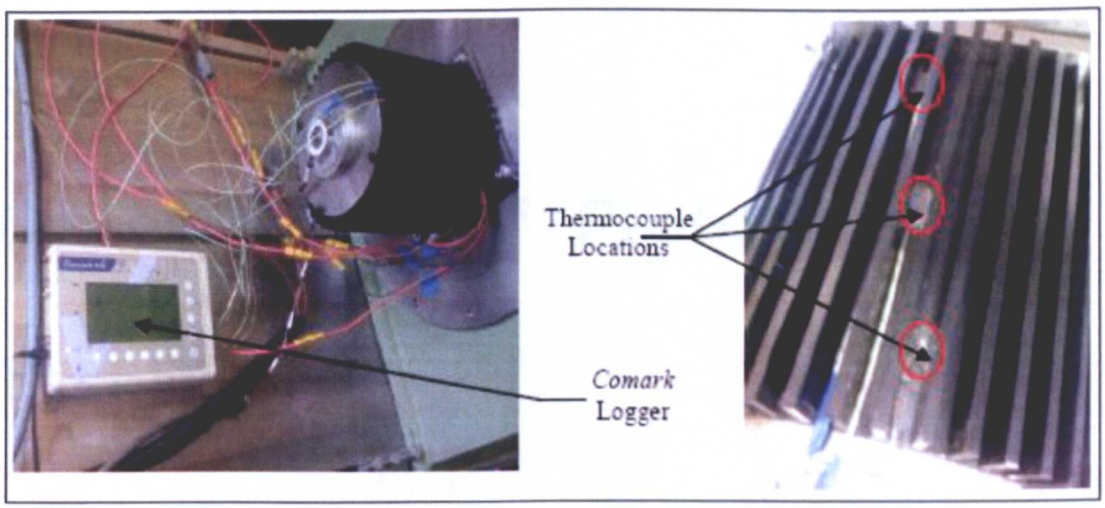

Figure 4-10: (i) 8 - Channel Data Logger, and (ii) Housing Thermocouple Locations

Chapter 5

Construction of Prototype and Test Rig

The structure of the permanent magnet motor consists of a three-phase winding (called the armature) hosted in the stator core and permanent magnets attached to the rotor core as shown in Figure 5-1. The machine is generally a 3-phase stator winding and can be distributed over a greater space angle than 60° electrical by using a double layer winding (two coil sides per slot, and not necessarily of the same phase).

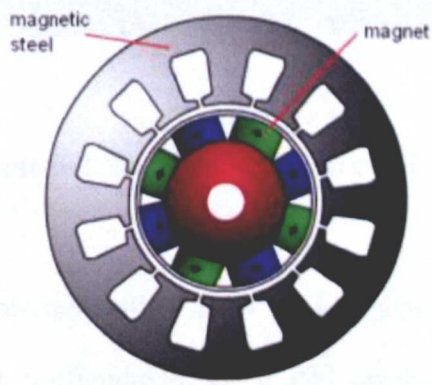

Figure 5-1: Structure of permanent magnet motor [43]

5.1 Stator Construction

The stator core of a PM machine consist of a stacked pack of steel laminations with windings placed in the slots that are axially cut along the inner periphery as shown in Figure 5-2. A 106 mm stator stack with 24 slots was constructed from 0.35 mm low loss electrical steel laminations plus 0.01 oxide coating.

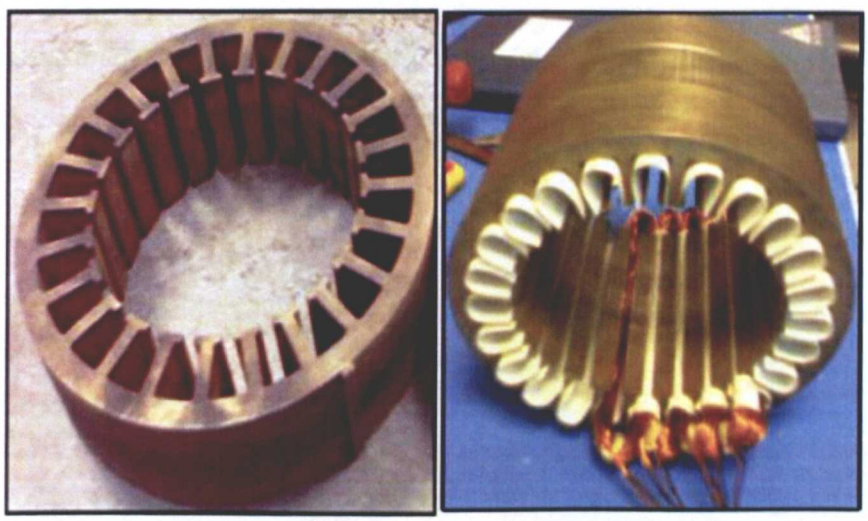

Figure 5-2: Stator construction of BLDC

Traditionally, the stator resembles that of an induction motor but the windings are distributed in a different configuration. Most PM machines have three windings which are connected in wye or star fashion. Each of these windings is constructed with numerous interconnected coils. One or more coils are placed in each slot and they are interconnected to make a winding. Each of these windings is distributed over the stator periphery to form an even numbers of poles. Trapezoidal and

sinusoidal motors have different types of stator windings as to produce the required waveform of back EMF.

5.2 Rotor Construction

The rotor is composed of an iron core and permanent magnets that can vary from two to various pole pairs with alternate North (N) and South (S) magnet directions. There are two configurations of permanent magnet rotor design: interior or surface mounted magnet design. Some books also classify the interior magnets solution as flux concentration magnets, inset magnet rotor and interior/buried magnet rotor. Figure 5-3 shows cross sections of different arrangements of the rotor configurations.

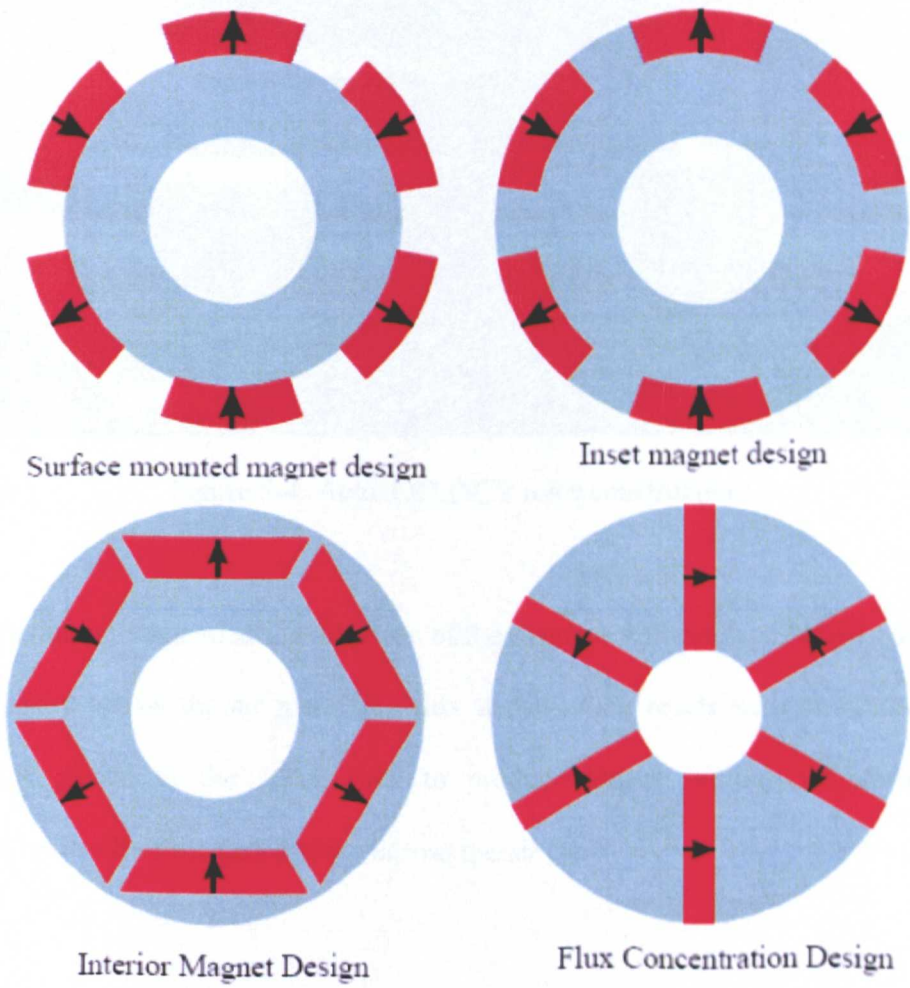

Figure 5-3: Configuration of rotor design [47]

In this thesis, the surface mounted magnet design is chosen due to its simplicity of construction and control since the reluctance torque could be neglected as the inductances are almost independent on the rotor position [48]. When the permeability of magnets is about equal to air, the direct and quadrature axis inductances of the surface-mounted PM machines are then approximately equal. This is because the length of the air gap is equal throughout the magnet, Figure 5-4 shows the actual rotor construction with alternating permanent magnet poles on the surface along the tangential direction.

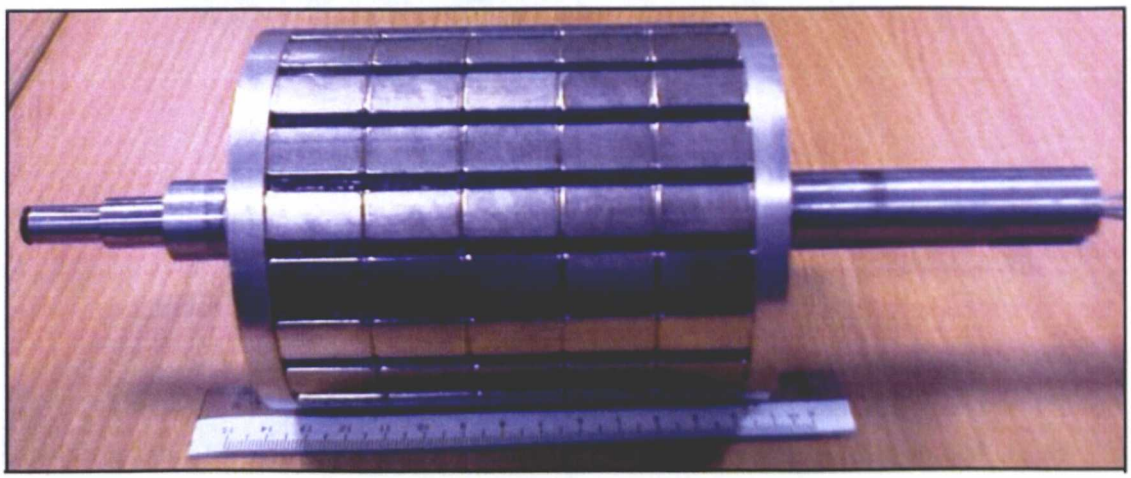

Figure 5-4: Actual BLDC's rotor construction

This alternating magnetization direction of the magnets will produce radially directed flux density across the air gap. This flux density then reacts with currents in the windings placed in the stator slots to produce torque. Figure 5-5 shows the simulation result of the flux density across the air gap.

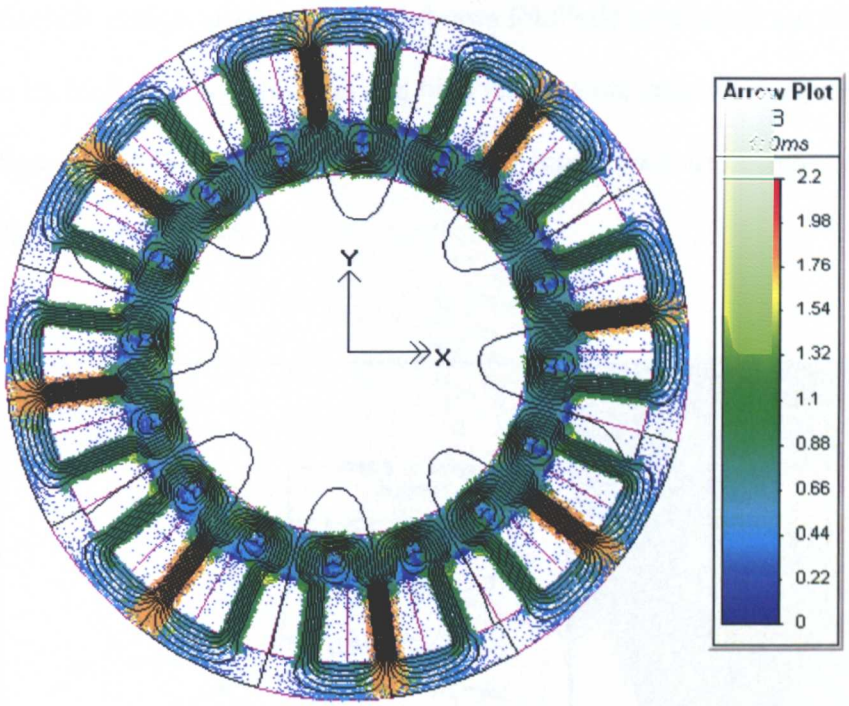

Figure 5-5: Flux density map

5.3 Permanent Magnet

There are three types of magnetic materials that are commonly used. For permanent magnets, an alloy such as AlNico has been used since 1930s and has a high residual flux density but lower coercive force [49]. Hard ferrites are an inexpensive but less magnetically powerful alternative frequently used. As the technology advance, new types of permanent magnets known as rare earth were developed and gained popularity. The combination of the rare earth elements such as neodymium and samarium with alloys materials such as iron, nickel and cobalt could produce a higher residual flux density and coercive force [49]. As a result, the rare earth magnets such as samarium-cobalt ($SmCo_2$) and neodymium-iron-boron (NdFeB) feature much higher specific energy and with respect to ferrite magnets. In this

machine design, neodymium-iron-boron (NdFeB) permanent magnet is selected due to its highest energy product and high temperature resistance capability as shown in Appendix F [50]. The magnet layout and actual placement onto the rotor surface is shown in Figure 5-6.

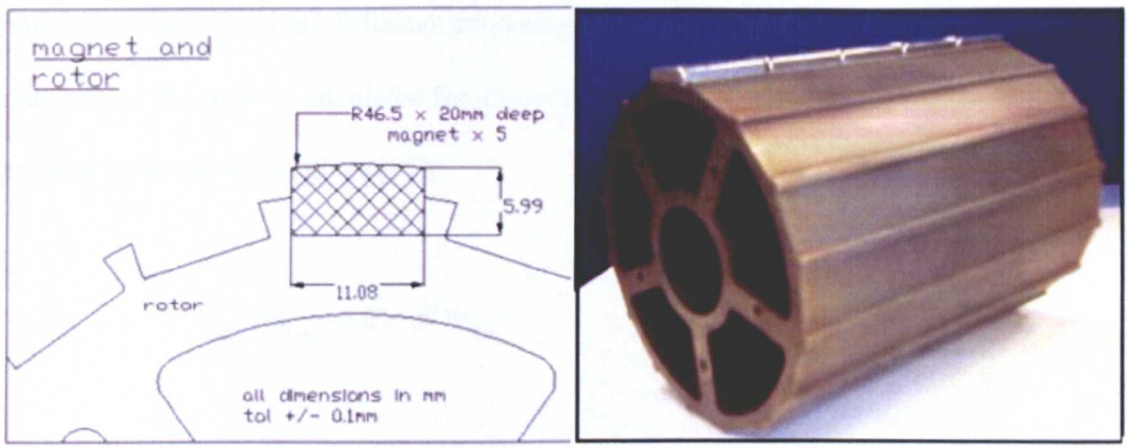

Figure 5-6: Magnet layout and placement of BLDC

5.4 Magnet Retaining Methods

There are several methods in retaining the permanent magnets on the surface of the rotor core such as rotor banding and adhesives the details of the selected method will be discussed below. The surface permanent magnet machine is influenced by mechanical restrictions of the fixation of the rotor magnets when high speed operation is required [51]. In fact, when the magnets are exposed to high centrifugal and mechanical stress, a holding device is required in order to withstand these forces.

5.5 Magnet Bonding Adhesives

One of a possible solution is to use structural magnet bonding adhesives. These adhesives should feature high temperature resistance, high impact and shear strength and high thermal conductivity in order to keep face with high temperature working condition and vibration. Schatzer recommended that the centrifugal force of the magnets on the rotor is calculated for an over-speed of 250% the nominal mechanical angular velocity, which gives [51]:

$$F_{mag} = m_{mag} \times 6.25 \times \omega^2 \times r_{mag} \qquad (5.1)$$

Where, m_{mag} is the mass of the magnet material, r_{mag} is the average radius of the magnets and ω is the nominal mechanical angular velocity in rad/s. The pressure of the magnets, P_{mag}, is defined as the ratio of the centrifugal force to the cross section area of the magnet. The residual pressure is calculated as the difference between the peel strength of the adhesive and the pressure of the magnet. In order to ensure that the magnets are fixed onto the rotor surface and the adhesive is sufficiently strong, the residual pressure must be larger than zero.

$$P_{res} = P_{adh} - P_{mag} > 0 \frac{N}{mm^2} \qquad (5.2)$$

Below is the tensile test result for the two types of adhesives used in this project as shown in Figure 5-7. The detail specifications of the adhesives are enclosed in Appendix G.

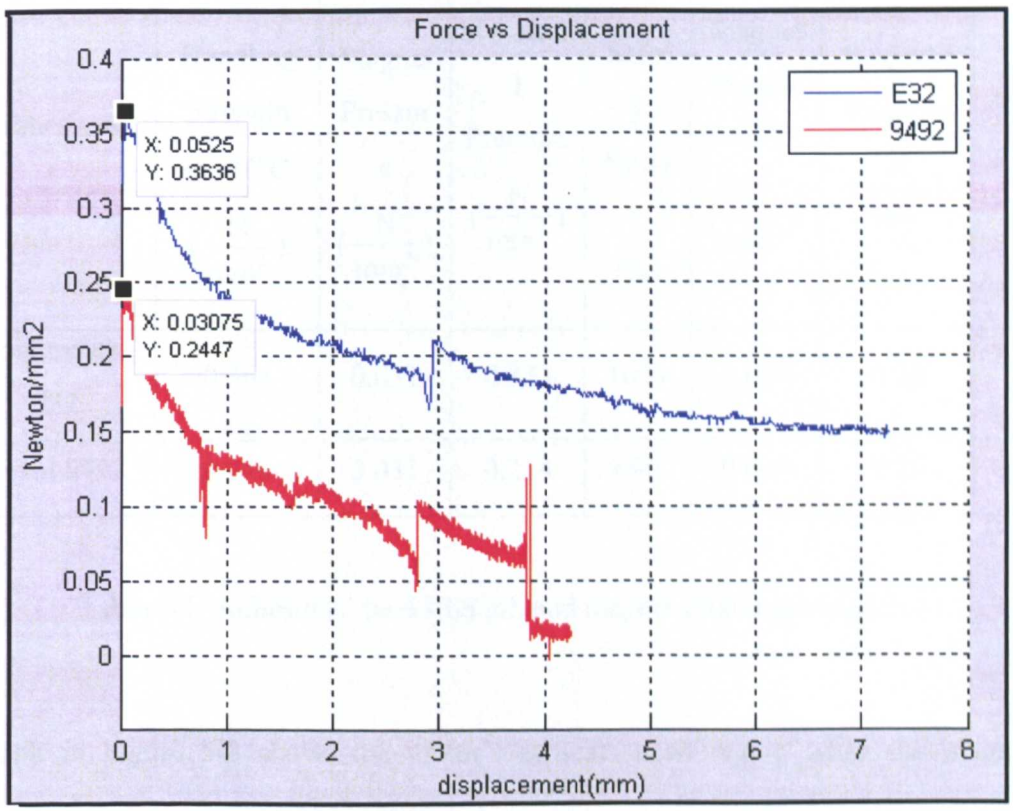

Figure 5-7: Tensile test result of the adhesives

The peel strength is determined by dividing the breaking force of the adhesives with the surface area of the magnet onto the substrate metal. The substrates are initially heated up to 120°C in order to have the actual operating temperature condition of the permanent magnet motor and to analyse the adhesives' temperature resistance property. The safety factor of the adhesives' peel strength at 120°C for rated and 1.2 times of the rated speed is shown in the Table 5-1 below. Basically the adhesive is

quite important in providing the sufficient contact pressure in order to withstand the centrifugal forces due to the magnet.

Adhesives	Speed	1200rpm (rated)			1440 rpm(1.2 x rated)		
	Handling Strength at 120°C ($\frac{N}{mm^2}$)	Magnet Pressure ($\frac{N}{mm^2}$)	Residual Pressure ($\frac{N}{mm^2}$)	Safety Factor (%)	Magnet Pressure ($\frac{N}{mm^2}$)	Residual Pressure ($\frac{N}{mm^2}$)	Safety Factor (%)
Bondmaster E32	0.364	0.031	0.333	1074	0.044	0.32	727
Hysol 9492	0.245	0.031	0.214	690	0.044	0.20	454

Table 5-1: Adhesives' peel strength and magnet retaining capability

Graph in Figure 5-8 shows the motor's critical speed region when the magnet pressure is equal to the peel strength capability of the selected glue. In another word, any further increase of the speed above 4140 rpm, the glue might peel off from the rotor magnets due to high speed operation with catastrophic effects.

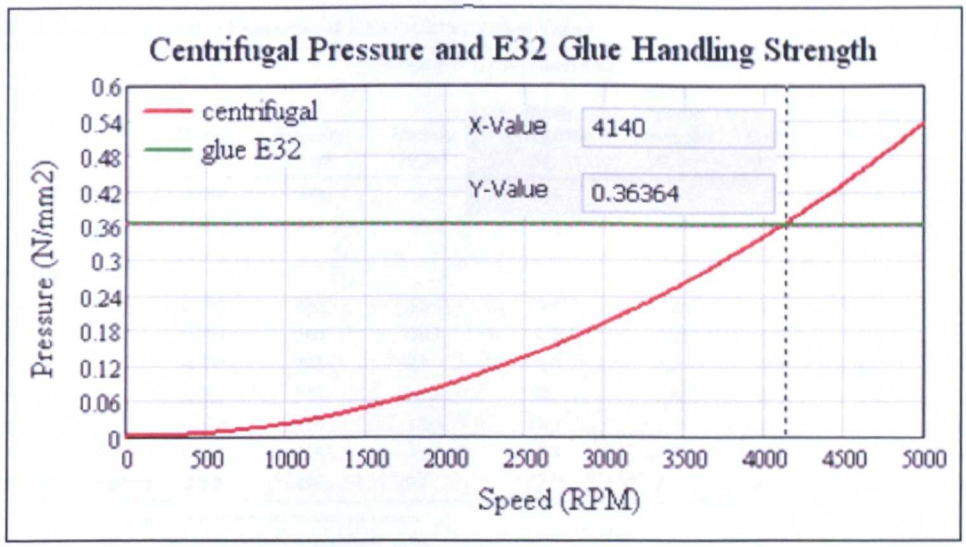

Figure 5-8: Critical speed region for E32 Glue

5.6 Magnet Banding

Another method in retaining the magnets is by using a sleeve or banding on the outer surface of the magnets. A composite sleeve like carbon or glass-fibre shall be used in order to withstand these high centrifugal and mechanical stresses due to high speed operation. Another possible solution is to use a non-magnetic steel cylinder to cover the magnets. The steel cylinder is very strong but flux variations will cause eddy currents resulting in larger losses compared to the composite sleeve [52].

The modulus of elasticity in tension, also known as Young's modulus E, is the ratio of stress to strain on the loading plane along the loading direction. The minimum Young's modulus of several type composite sleeves is shown in Table 5-2 below [53].

TABLE II-2. Comparative Properties of KEVLAR® vs. Other Yarns

	"Customary" (inch-pound) Units							
	Specific Density lb/in.³	Tenacity 10^3 psi	Modulus 10^6 psi	Break Elongation %	Specific Tensile Strength* 10^6 in.	CTE** 10^{-6}/°F	Decomposition Temperature °F	(°C)
KEVLAR 29	0.052	424	10.2	3.6	8.15	-2.2	800-900	(427-482)
KEVLAR 49	0.052	435	16.3	2.4	8.37	-2.7	800-900	(427-482)
Other Yarns								
S-Glass	0.090	665	12.4	5.4	7.40	+1.7	1,562†	(850)
E-Glass	0.092	500	10.5	4.8	5.43	+1.6	1,346	(730)
Steel Wire	0.280	285	29	2.0	1.0	+3.7	2,732†	(1,500)
Nylon-66	0.042	143	0.8	18.3	3.40	—	490	(254)
Polyester	0.050	168	2.0	14.5	3.36	—	493†	(256)
HS Polyethylene	0.035	375	17	3.5	10.7	—	300	(149)
High-Tenacity Carbon	0.065	450	32	1.4	6.93	-0.1	6,332	(3,500)

*Specific tensile strength is obtained by dividing the tenacity by the density.
**CTE is the coefficient of thermal expansion (in the longitudinal direction).
†Melt temperature.

Table 5-2: The modulus of elasticity of various composite

Normally, the inner diameter of the prefabricated fibre sleeve cylinder has a bit smaller dimension than the rotor outer diameter d, by the value ΔD. The sleeve assembly is done on the rotor by either axial pressing or cold shrinking methods and the initial tangential tension within the sleeve is given by [52]:

$$\sigma = \frac{\Delta D}{d} \times E \tag{5.3}$$

The pressure of the sleeve on the magnets with h_b as the sleeve thickness can be written as:

$$P_{bm} = \frac{2\sigma h_b}{d + h_b} \tag{5.4}$$

The centrifugal pressure of the magnets on the sleeve is calculated for an over-speed of 120% the nominal mechanical angular velocity, which gives [48]:

$$P_{mb} = \rho_m (1.2 \times N \times \frac{\pi d}{60})^2 \times \frac{h_m}{r_m} \qquad (5.5)$$

ρ_m is the mass density of the magnet material, r_m is the average radius of the magnets, N is the rated speed in rpm and h_m is the height of the magnets. The centrifugal pressure of the sleeve is calculated using the above equation by replacing the average radius, the mass density and the height related to the sleeve respectively.

$$P_{bb} = \rho_b (1.2 \times N \times \frac{\pi d}{60})^2 \times \frac{h_b}{r_b} \qquad (5.6)$$

The residual pressure is calculated as the difference between the pressure of the sleeve and the sum of the centrifugal pressure of the magnets and the sleeve. In order to ensure that the magnets are fixed on to the rotor surface and the sleeve is sufficiently strong, the residual pressure must be larger than zero.

$$P_{res} = P_{bm} - P_{mb} - P_{bb} > 0 \frac{N}{mm^2} \qquad (5.7)$$

Figure 5-10 shows some results simulated in ***MathCad*** software on the minimum undersize sleeve dimension for several types of composite fibres at various speeds. The actual damage occurred onto the rotor if the above considerations are neglected

is visible in Figure 5-9. This was due to wrong sizing of the sleeve dimension which consequently providing insufficient residual pressure in ensuring the rotor magnets stayed stationary on the rotor surface. As a result, the rotor magnets pushed the sleeve up due to its' centrifugal force and touched the surface of the stator. Basically the undersized dimension of the sleeve is quite important in providing the sufficient contact pressure in order to withstand the centrifugal forces due to the magnet and the sleeve itself.

Figure 5-9: The PMSM's rotor and the damaged sleeve

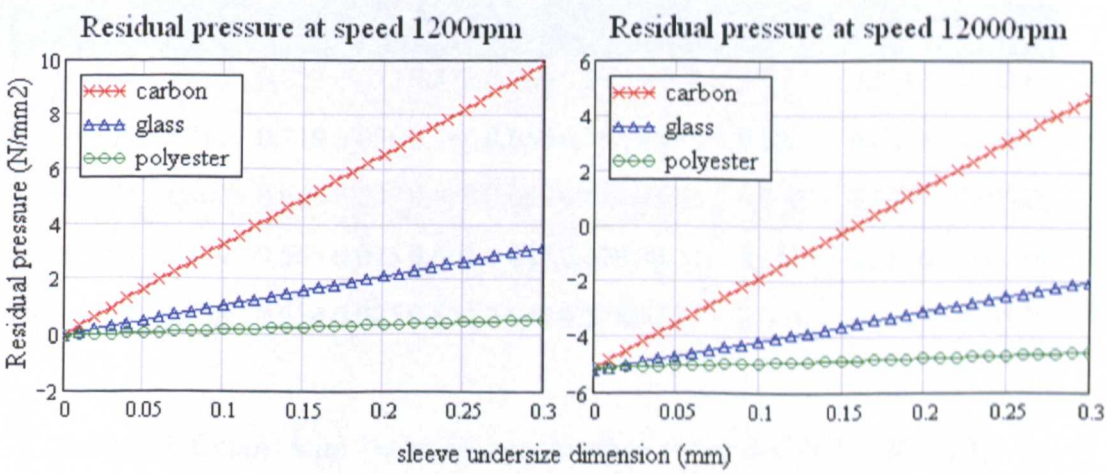

Figure 5-10: Minimum undersize sleeve dimension for respective composite fibers

5.7 Stator Winding

A three-phase winding is installed in the stator using high temperature duty grade copper wire. In Table 5-3, the detail specifications of various copper wires are reported and the selected wire is highlighted.

				Grade -1		Grade -2		Grade - 3			
	Conductor Dia			Min.	Max.	Min.	Max.	Min.	Max.	Resistance at 20 deg.C	
Size	Min.	Nominal	Max.	Inc.	O.D	Inc.	O.D	Inc.	O.D Ohms per	Ohms per metre	
SWG	mm	mm	mm	mm	mm	mm	mm	mm	mm	min.	Max.
15	1.810	1.829	1.848	0.040	1.903	0.075	1.941	0.113	1.977	0.0063	0.0067
16	1.607	1.626	1.643	0.039	1.698	0.073	1.735	0.110	1.770	0.0080	0.0085
17	1.407	1.422	1.437	0.038	1.492	0.071	1.528	0.107	1.562	0.0105	0.0111
18	1.206	1.219	1.232	0.035	1.285	0.067	1.318	0.100	1.350	0.0142	0.0151
19	1.005	1.016	1.027	0.034	1.080	0.065	1.113	0.098	1.144	0.0205	0.0217
20	0.904	0.914	0.924	0.034	0.976	0.063	1.008	0.095	1.038	0.0253	0.0269
21	0.804	0.813	0.822	0.032	0.872	0.060	0.902	0.090	0.931	0.0319	0.0340
22	0.703	0.711	0.719	0.030	0.766	0.056	0.795	0.085	0.822	0.0418	0.0444
23	0.604	0.61	0.616	0.027	0.659	0.050	0.684	0.075	0.708	0.0569	0.0602
24	0.553	0.559	0.565	0.025	0.605	0.047	0.629	0.071	0.652	0.0676	0.0718
25	0.502	0.508	0.514	0.025	0.554	0.047	0.578	0.071	0.601	0.0816	0.0871

Table 5-3: Copper wire Technical Specification as per IEC-60317-0-1 [53]

The windings are similar in design and function to those used in a conventional induction or synchronous motor. When connected to an appropriate symmetrical power source, the currents in the windings produce a rotating magnetic field, which interacts with the rotor and produce a rotational torque on shaft. Figure 5-11 shows the winding configuration and an actual layout for PM machine.

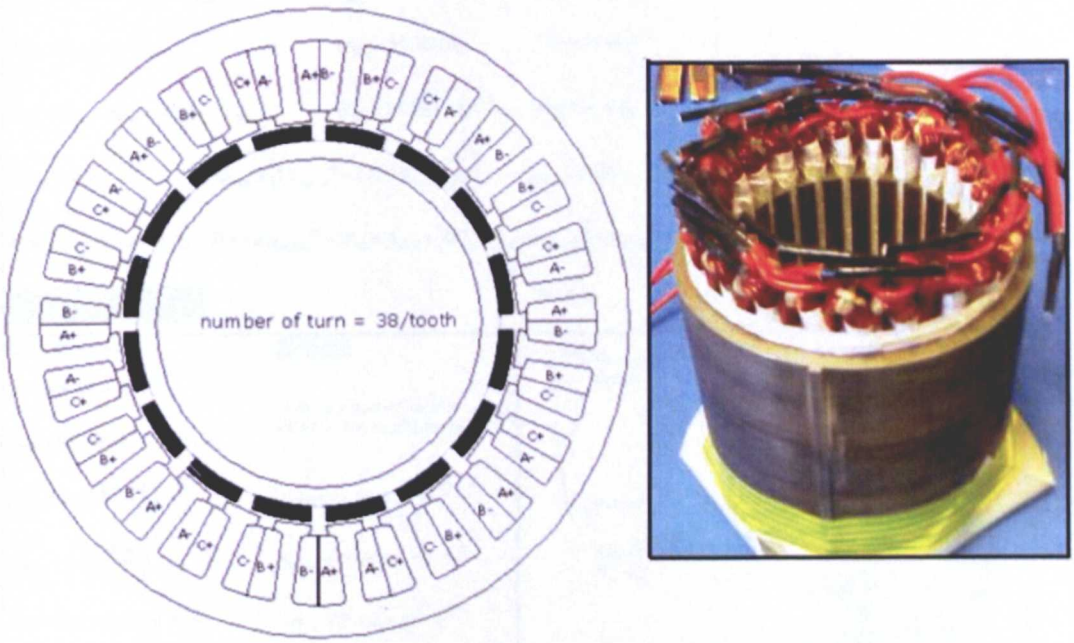

Figure 5-11: BLDC's winding configuration and layout

The winding wire specification is dependent on the slot opening, the wire size to be used, the compatibility of the selected tooling and the slot liners. The slot liners is an insulating material to be put onto the inner slot surface in order to avoid any abrasion and possible electrical shorts between the windings and the stator. The larger the slot opening, the greater the versatility in wire size selection and the number of strands to be used. A simple mathematical program is used to analyse and select the appropriate winding wire for the motor as shown in the following screenshots of the ***MathCAD***

software program created for the determination of the required parameters, such as: copper area, slot area, slot fill factor and approximation of the winding resistance.

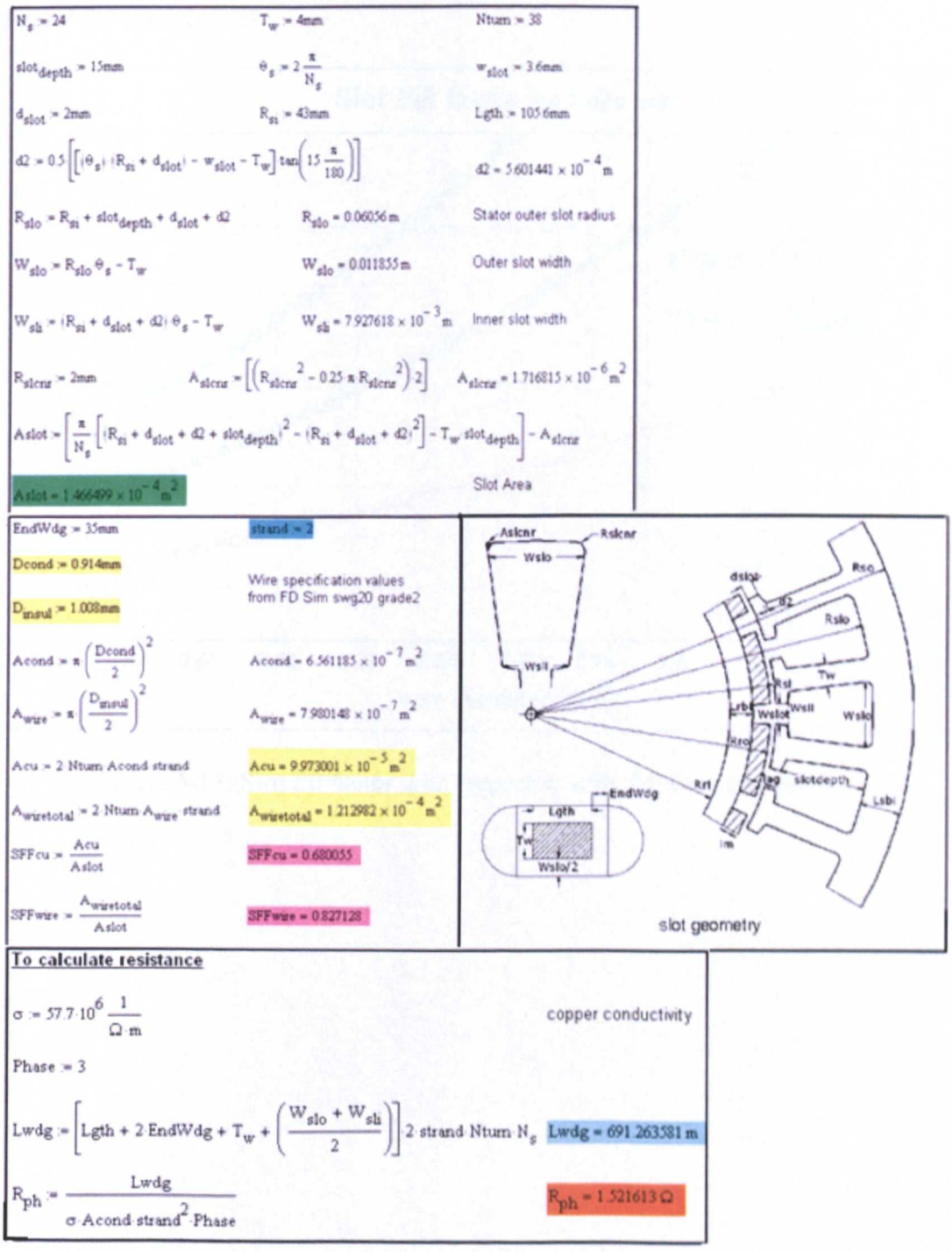

Figure 5-12: Screenshots of the ***MathCAD*** Program for BLDC winding determination

The slot opening versus wire size selection which reflects the slot fill factor and winding resistance can be best explained by the charts shown in Figure 5-13 and Figure 5-14 respectively.

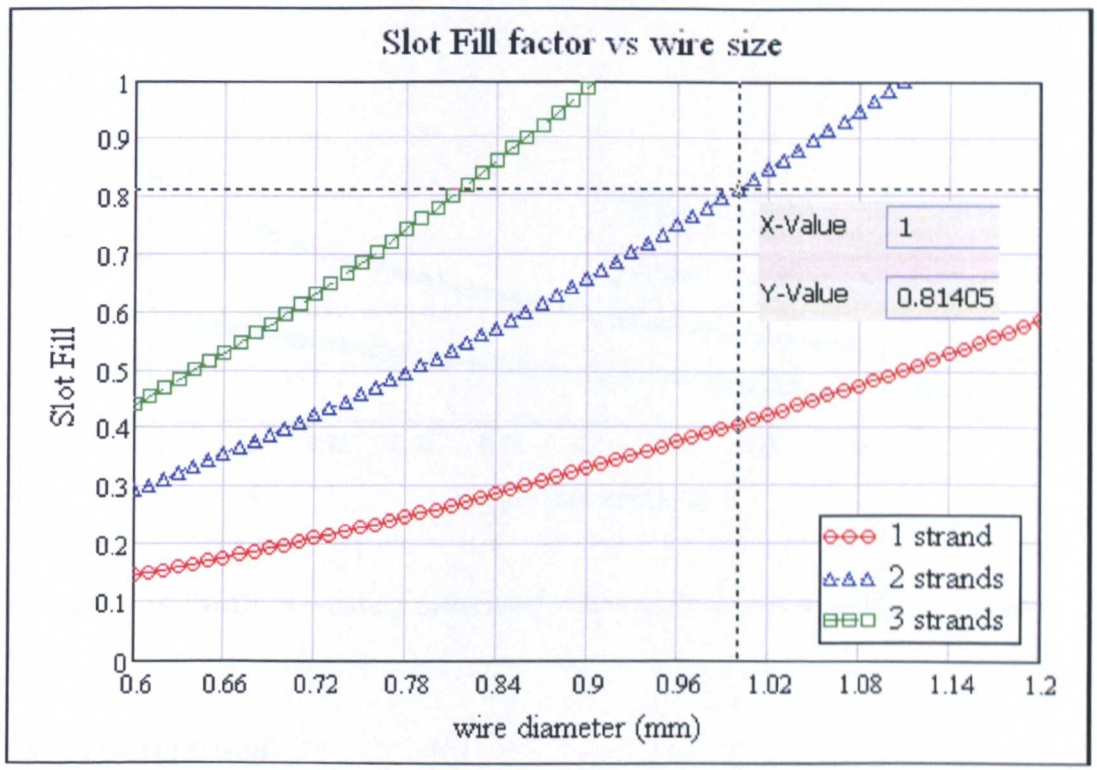

Figure 5-13: Slot fill factor with respect to wire diameter and strand

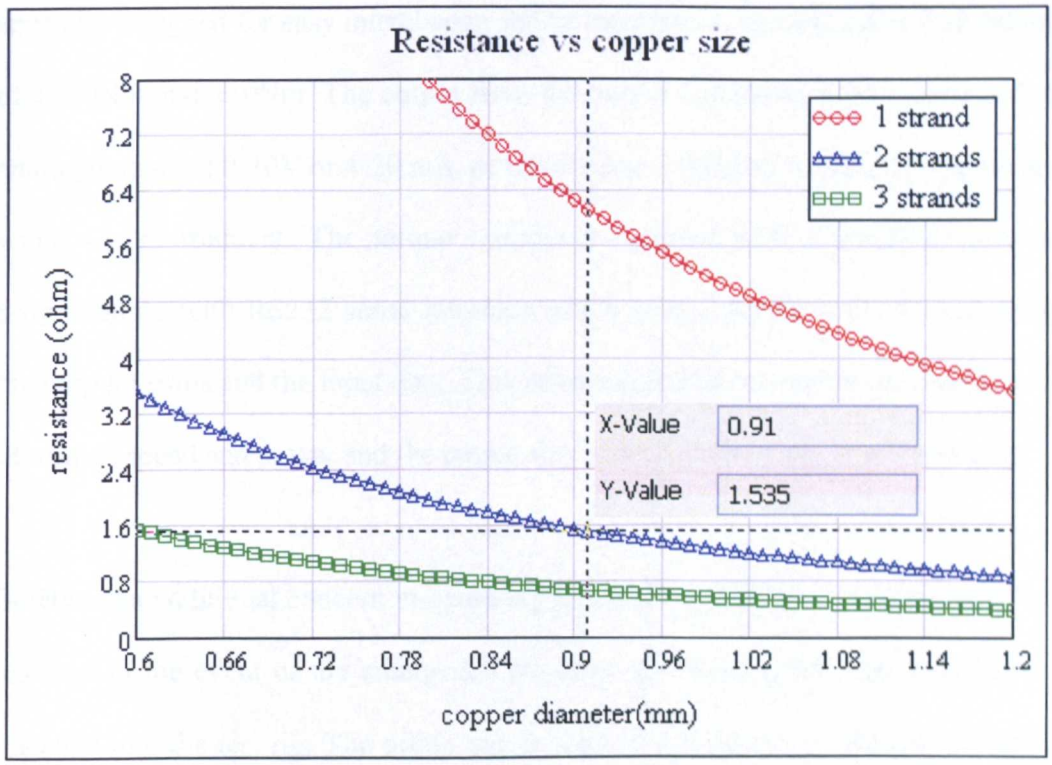

Figure 5-14: BLDC's winding resistance with respect to wire diameter and strand

5.8 Test rig set-up

The prototype motor is tested on the 'Electric Motor High Speed Test Rig' supplied by Torquemeters Ltd,. Figure 5-15 shows the test rig and equipment used in this research. This test rig is a four-quadrant rig and designed to drive and absorb power from the test machine using a 40kW (nominal) variable speed AC motor as a prime mover with a maximum speed of 20000rpm [54]. The prime mover is connected to the rig components using flexible element couplings with final drive to the test machine through a splined quill shaft [54].

The system torque is measured using an in-line pedestal torque transducer model with a maximum rating of ±100Nm. The standard model torquemeter has been

specially designed for easy interchange ability between the torsion shafts with ratings of ±100Nm and ±10Nm. The output from the torque transducer can be measured as analog outputs of 0-10V or 4-20 mA, or readily converted into the digital outputs in a windows environment. The torque transducer is fitted with a standard software programming with RS232 serial interface which give a simple way of configuring the output results and the input data. This software gives a constantly updated display of torque, speed and power and the output data can be periodically saved into a file.

Safety is an additional concern in operating this test rig. To stop the operation of the test bed in the event of the emergency situation, few emergency stop switches are installed into the test rig. The prime mover's drive will decelerate the test rig at the maximum possible rate to zero speed and then disable the system. In addition, in order to protect the user, a large transparent enclosure is built that can be placed over the test machine when the system is running.

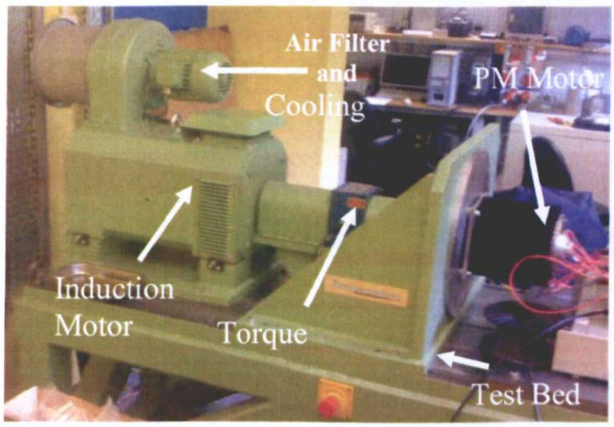

(i)

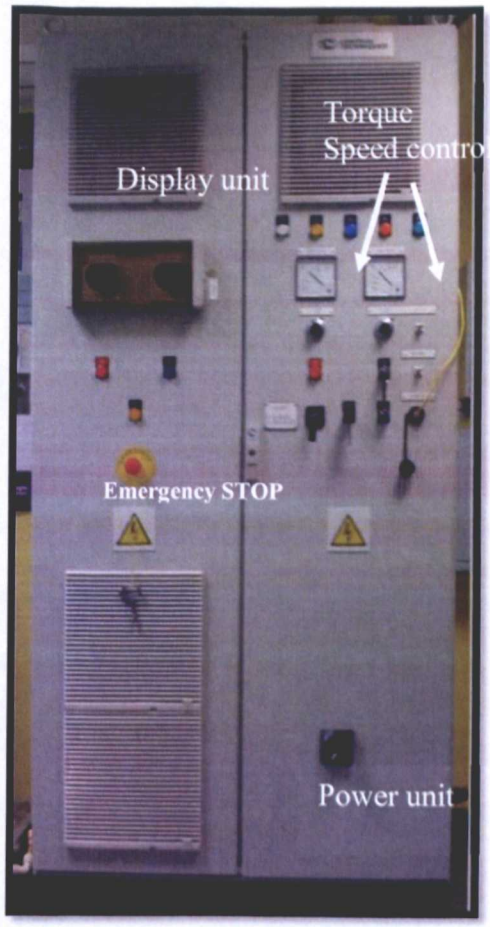

(iii)

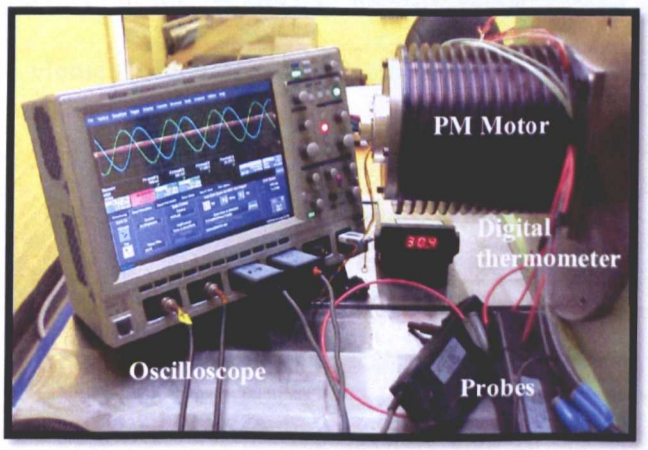

(ii)

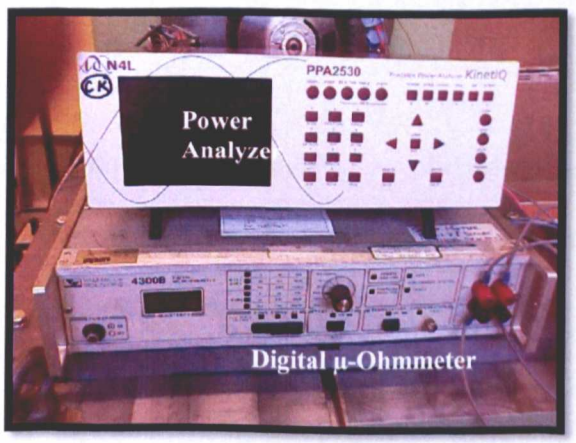

(iv)

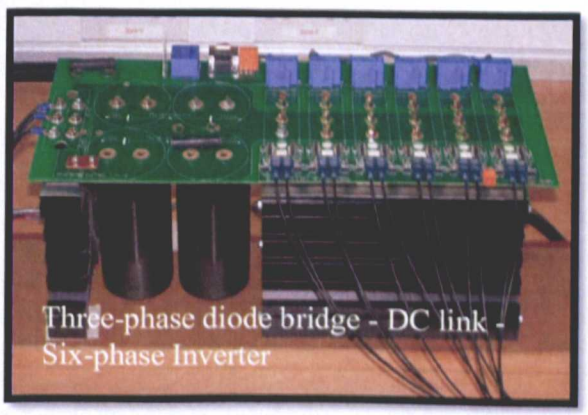

(v)

Figure 5-15: Test rig set-up (i) High speed test bed (ii) Measurement equipment (iii) High speed test bed control panel (iv) Measurement equipment (v) Power Converter

Chapter 6

Simulation Versus Experimental Results Comparison

Once all the parameters have been determined, the motor is simulated in the finite element software, Magnet, in order to predict the induced back EMF, phase currents and the produced loading torque. The motor used in this experiment is radial flux BLAC of 24 slots and 20 poles with double layer winding configuration. The motor performance is then tested under four major conditions and the results will be evaluated and compared with the simulated and analytical models respectively which are defined in chapter 1.

6.1 Condition 1: No Load

The no load test is carried out assuming that the motor is mounted on the test rig and rotated at certain speed. In this experiment the prototyped motor Q24P20 is rotated at 585rpm and the induced back EMF for every phase is measured. Figure 6-1 and Table 6-1 below show the detail of the back EMF results and the comparison of the results respectively.

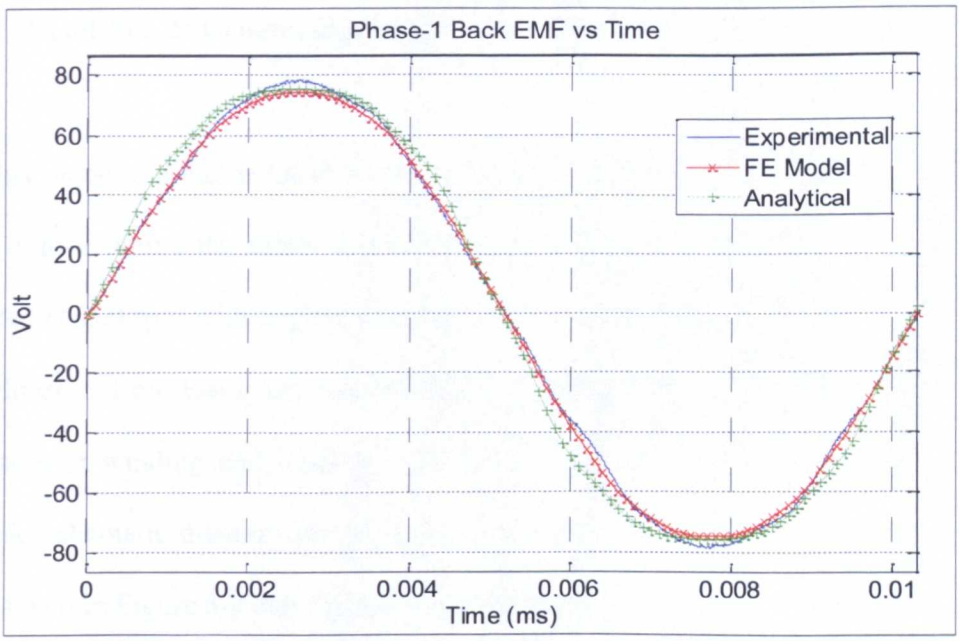

Figure 6-1: Back EMF results

BEMF	Volt_rms			Difference	
	Actual	FE model	Analytical	FE model	Analytical
Phase 1	54.55	53.47	56.93	-1.98%	4.36-%
Phase 2	54.74	54.05	56.93	-1.26%	4.00%
Phase 3	53.80	54.02	56.93	0.41%	5.82%

Table 6-1: Back EMF comparison

Based on the above results, the waveforms are similar and differences between actual, finite element model and analytical are small.

6.2 Condition 2: Generating Mode

In this mode, the motor Q24P20 is undergoing a test in the generating mode. This test is to examine the motor capability when it acts as a generator. The motor is rotated at 200 rpm with applied resistive loads about 5.1 ohms each. Both the motor windings and the loads are connected in star configuration. The both output phase voltages at winding and loads as well as the developed torque are measured. A simple schematic diagram for FE model simulation and actual experimental set-up are shown in Figure 6-2 and Figure 6-3 respectively.

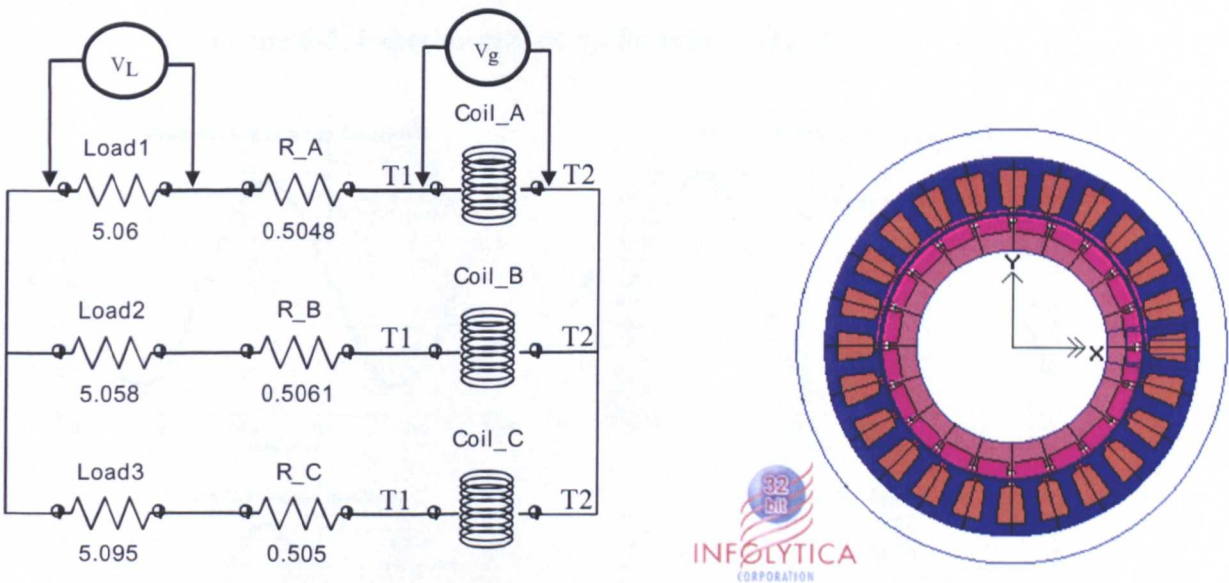

Figure 6-2: Generating mode schematic diagram and FE model

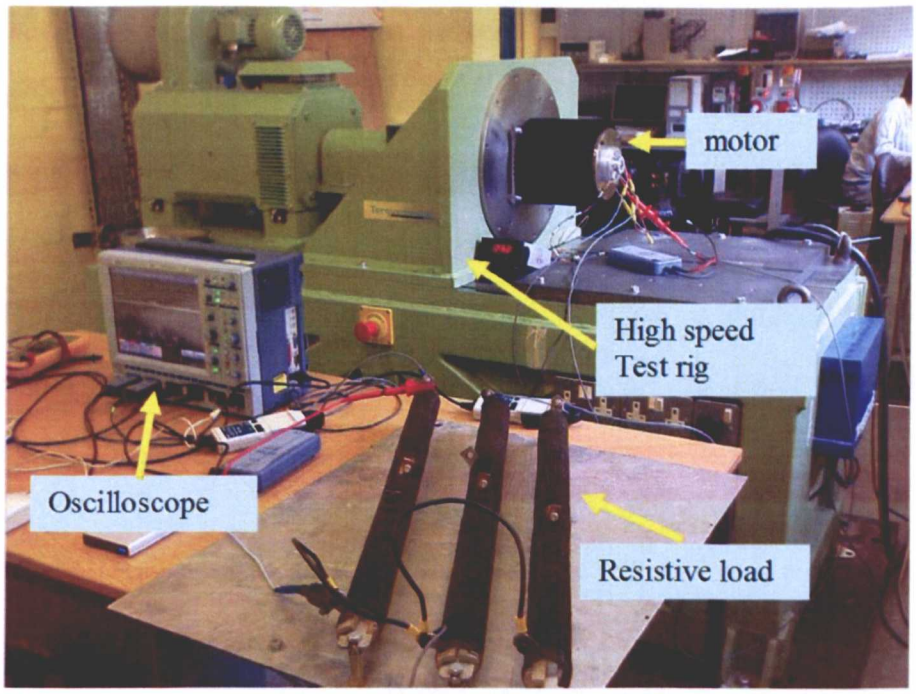

Figure 6-3: Experimental set-up for Generating Mode

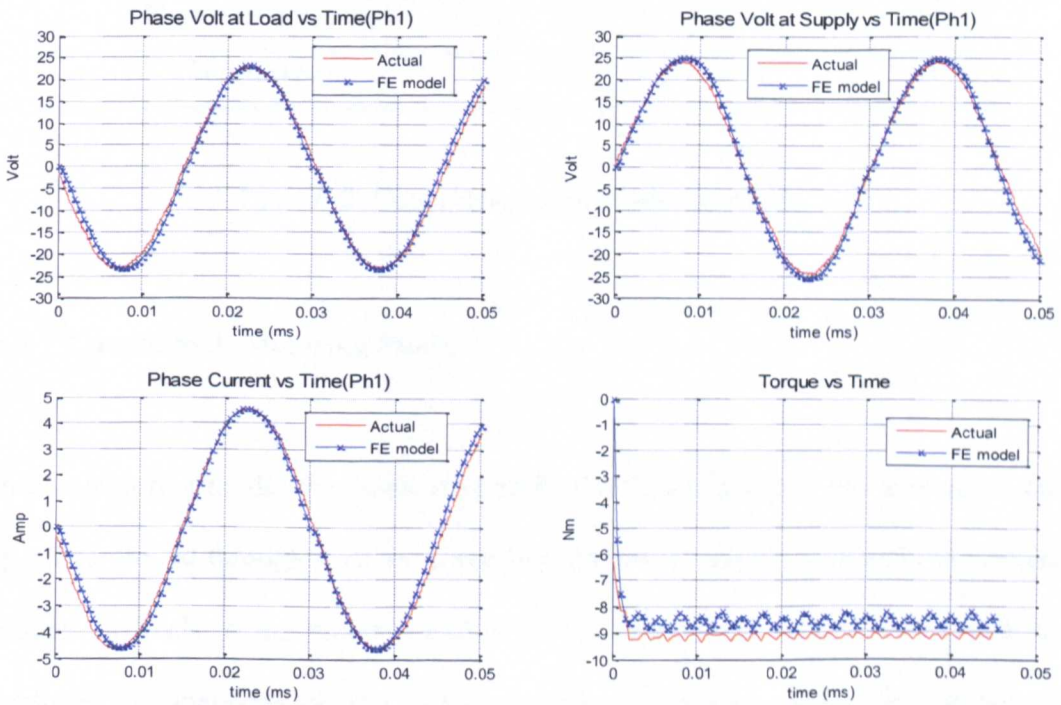

Figure 6-4: Generating mode result

The Figure 6-4 above shows the comparison of results between the FE model and the actual experimental results in the generating mode. The output phase voltages waveforms at the windings and loads are reasonably match well the FE model. In general, the predicted torque produced in FE model is close to the experiment. There is a slight voltage drop between the phase voltage at windings and loads due to winding resistances. Below is the summary of the results and the percentage different between predicted and actual results.

Parameters	RMS values		Different
	Actual	FE Model	
Phase voltage at load (V_L)	16.44	16.34	-0.58%
Phase voltage at winding (V_g)	16.83	18.00	6.95%
Phase current (amp)	3.30	3.23	-1.96%
Torque (Nm)	-9.12	-8.55	-6.27%

Table 6-2: Generating mode comparison result

6.3 Condition 3: Motoring Mode

In this motoring mode, the motor is controlled with a 6-phase power converter and speed controlled through a vector controlled system. A test rig provided the various torques or loads to the motor under test. The performance of the motor will be evaluated by analyzing all the output waveforms that are captured by the power analyzers. Below are the results when the motor is examined at various speeds from 200 rpm to 1150 rpm (200 radian-per-second (rps) to 1200rps electrical speed for 10 pair poles machine) and various torques from 10 Nm to 40 Nm. Most of the results

are quite close to the predicted values in the simulated FE model. The torque constant Kt reduces as expected with load due to iron saturation. It was also observed that it reduced as a function of speed. This could be due to the increase in iron losses components.

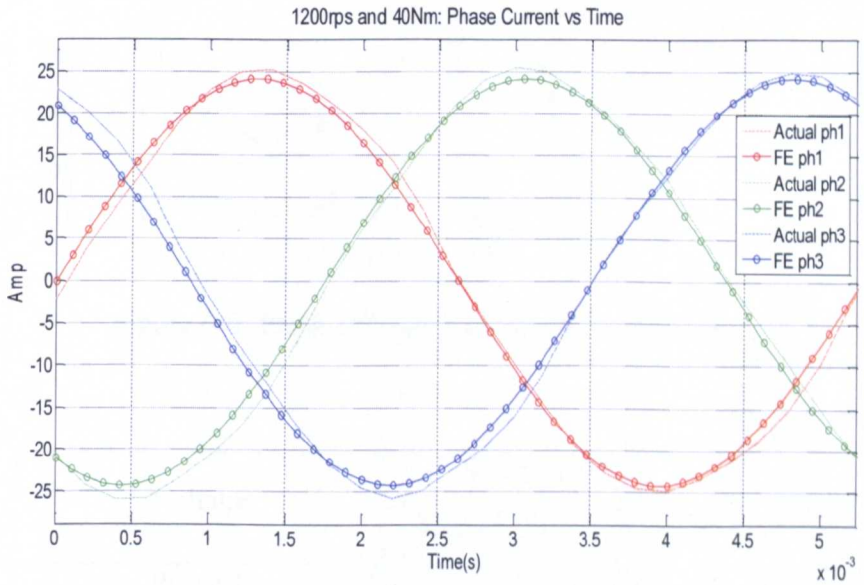

Figure 6-5: Phase current waveforms in motoring mode

Current	RMS values		Different
	Actual	FE Model	
Phase1	17.57	16.65	-5.25%
Phase 2	17.58	17.44	-0.79%
Phase 3	17.60	17.24	-2.04%

Table 6-3: Phase current comparison

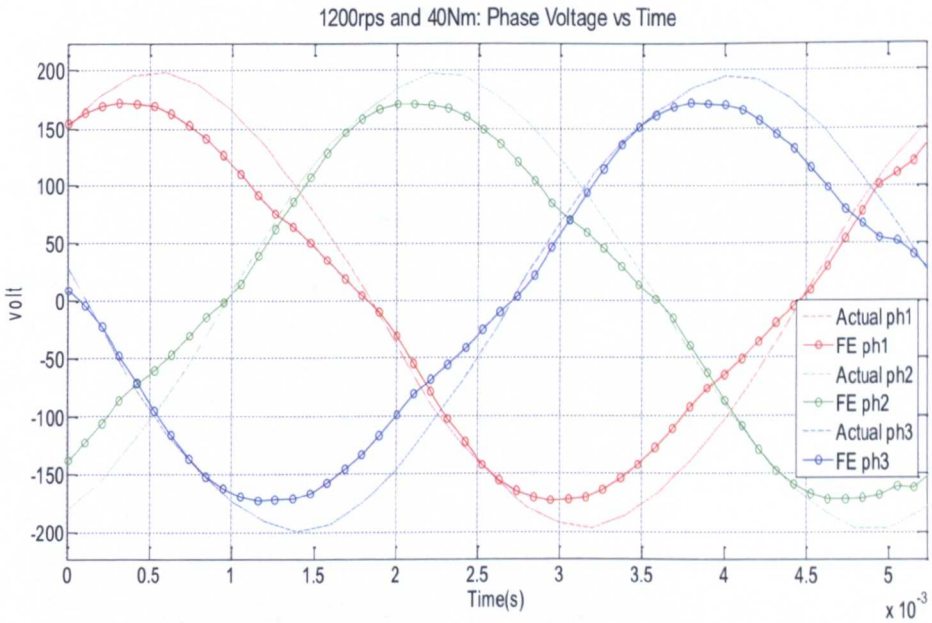

Figure 6-6: Phase voltage waveforms in motoring mode

Voltage	RMS values		Different
	Actual	FE Model	
Phase 1	137.60	119.18	-13.4%
Phase 2	137.40	118.87	-13.5%
Phase 3	137.50	114.28	-16.9%

Table 6-4: Phase voltage comparison

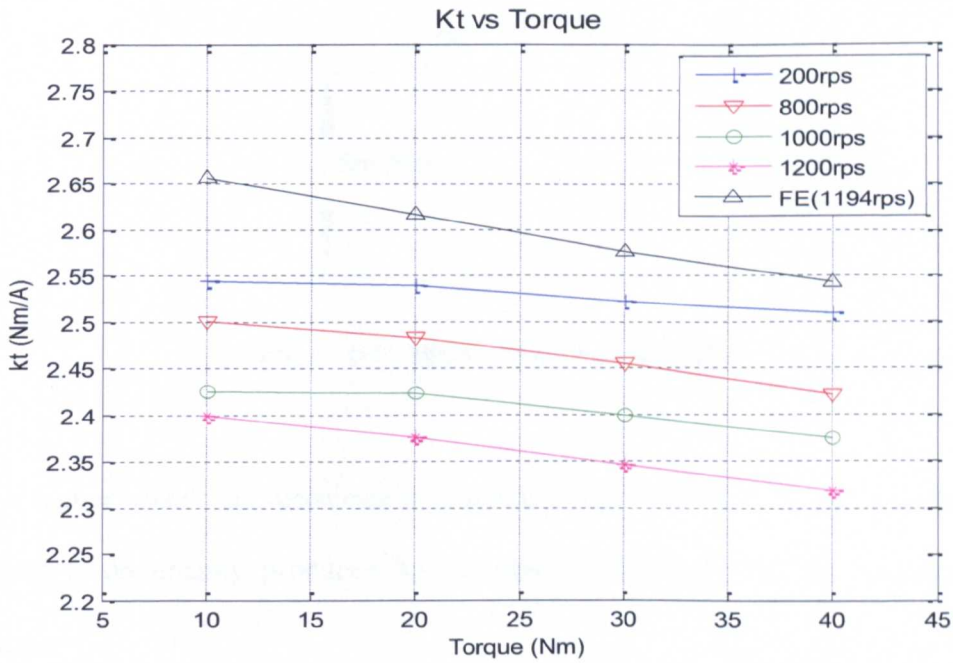

Figure 6-7: Torque constant Kt at various speeds and torques

6.4 Condition 4: Fault Mode

A number of fault conditions are also analysed. It is a fact that any fault occurrences in a motor may cause the total failure of the entire system. There are two main electrical faults that can possibly occur in an electric motor: a short circuit and an open circuit faults.

6.4.1 Short Circuit

A short circuit fault happens when all the phases are shorted together at the terminal connection. In the event of a short circuit, the current which flows is limited by the phase resistance and inductance. This short circuit fault can be depicted by the following diagram in Figure 6-8.

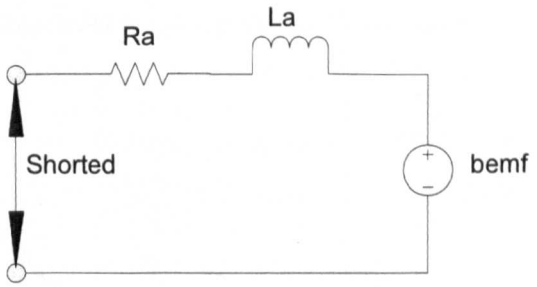

Figure 6-8: Short circuit fault diagram

At a higher speed, the resistance is generally very small and in practice the fault current is dominantly produced by the phase back EMF and the inductance as follows.

$$i_{sc} = \frac{bemf}{R_{ph} + j\omega L_{ph}} \qquad (6.1)$$

The braking torque as a function of speed is estimated as:

$$T_{sc} = \frac{3 \cdot i_{sc}^{\ 2} \cdot R_{ph}}{\omega} \qquad (6.2)$$

An experimental investigation is carried out to obtain both the Torque - Speed characteristics of the motor as well as the current flow during the short circuit condition. These experimental results will be later compared to both the predicted finite element analysis and analytical results. The analytical result is obtained by analysing the actual machine parameters with linear assumption as described in equations (6.1) and (6.2) using standard analysis program software as shown in Appendix H.

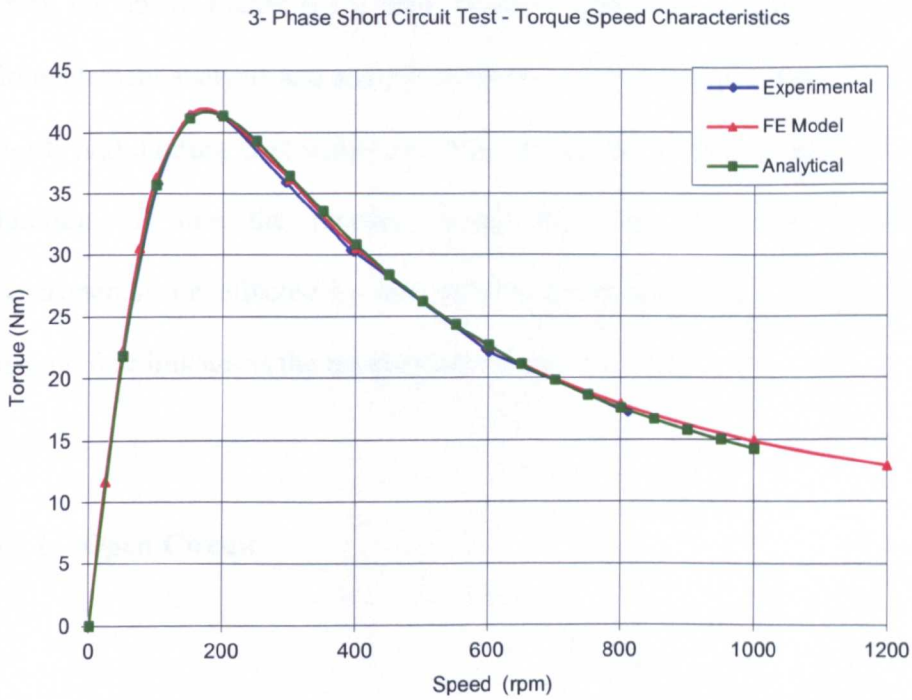

Figure 6-9: Braking torque during 3-phase short circuit fault

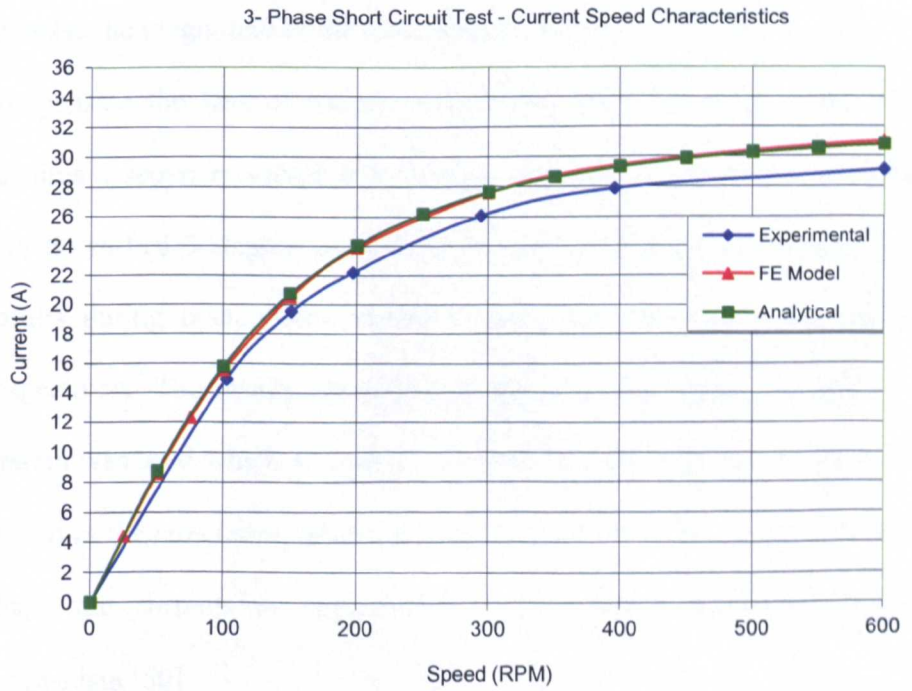

Figure 6-10: Short circuit phase current during 3-phase short circuit fault

From the above Figure 6-10, there is close agreement between both the predicted finite element analysis and analytical results with the actual experimental results. It is worth highlighting that whilst the tests in the lab were not done for a very long duration of time the machine temperature did vary and consequently the experimental are affected by this, mainly increased winding resistance and lower magnet flux linkage as the temperature increases.

6.4.2 **Open Circuit**

An open circuit fault in a motor occurs when one of the phases is interrupted and leaving the other two phases in healthy condition. The motor can still operate by applying the fault tolerant control strategy as presented in [55]. This strategy will increase the magnitude of the remaining healthy phases by factor of 1.732 in order to compensate the loss of torque contribution from the faulty phase. This strategy requires a separate converter to control each phase and the healthy phases current will be shifted 30degree away from the phasor of the faulty phase. Below are the results during open circuit operation for both simulated and experimental tests respectively. The results are different due to the voltage controlled experimental system was used which as a result the current values did not settle to the ideal case shown in the simulation results. A way forward could be to use hysteresis control to shape the currents as required or else to add a feed-forward compensation mechanism [56].

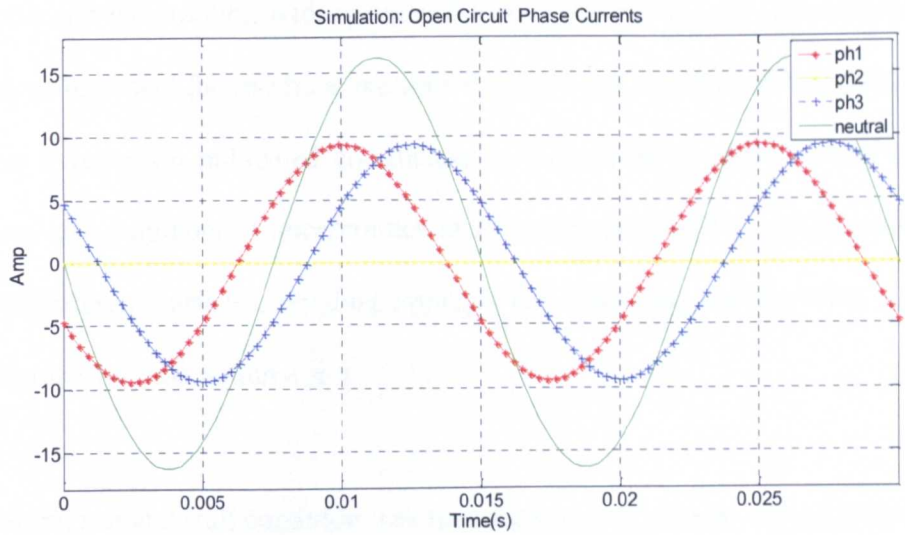

Figure 6-11: Simulated phase currents during open circuit fault

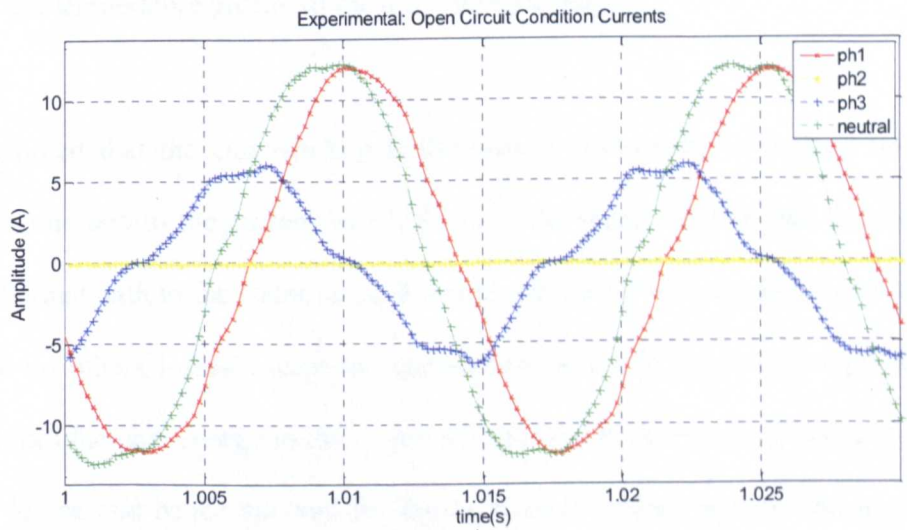

Figure 6-12: Experimental phase currents during open circuit fault

6.5 Thermal Results

A range of thermal tests were done to better understand the motor's capability and limitations. ***MotorCAD*** was used to investigate the temperature distribution within

the motor and its variation with speed and load. ***MotorCAD*** uses lumped-resistance network to represent the machine and thus it is very fast in terms of evaluation times however it relies on published correlations to determine convective heat transfer. There are also a number of uncertainties in such a model, namely contact resistances between different surfaces, winding impregnation goodness and the distribution of the individual strands within a slot.

The thermal test at a stall condition was first done and the results utilised primarily to calibrate the ***MotorCAD*** software. Several experiments were performed for the 20 poles motor at various torque values such as 5Nm, 10Nm, 15Nm and 20Nm as to obtain the temperature profile of the motor components.

It was noted that the end winding is the critical component as it heats up at the greatest rate due to the current which flows in the stator winding and the lack of a good thermal path to the stator stack. Knowing the fact that in a stall condition, there will be no others losses except the copper loss which is the only component that contributes the heat energy to the motor this allowed to have a good certainty on the motor losses and hence allowed for the calibration of the thermal circuit. A great amount of time was spent in calibrating the thermal parameters' of the model so as to bring down the over-predicted ***MotorCAD*** temperature contours to the experimental results obtained. It is worth mentioning about the meaning of 'calibration'. In this context, 'calibration' refers to modifying certain default parameters in ***MotorCAD***, which were unknown. These parameters included, and were not limited to;

i) component clearances

ii) natural convection coefficient for fins

iii) stator stacking factor

iv) impregnation material properties

The thermal results obtained, both from the experiment as well as from MotorCAD were analysed and a comparative study was undertaken. The combined results obtained for a 20Nm stalled motor operating condition on temperature plotting and percentage difference table are shown in

Figure 6-13 and Table 6-6 respectively, thus giving a clearer picture of the ensuing results.

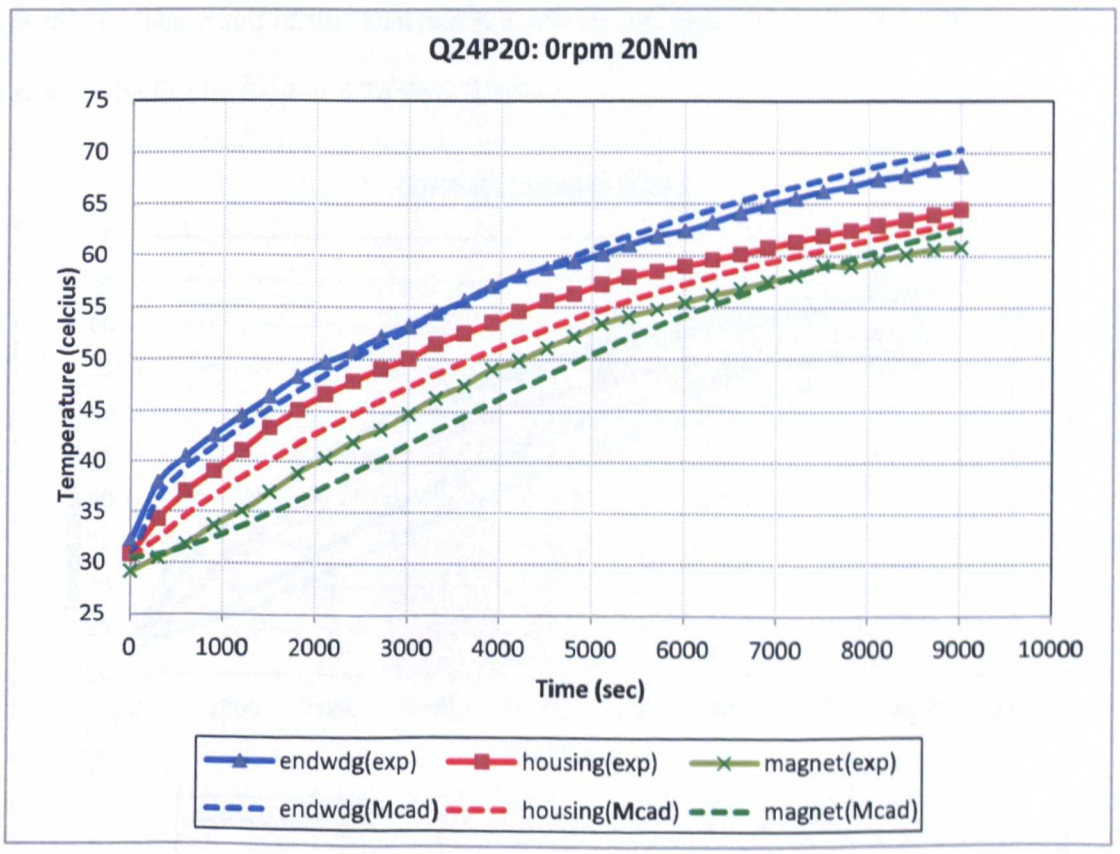

Figure 6-13: MotorCAD model calibrated with the 20Nm Experimental Result

Additional tests at various speeds and torques were also carried out. This was primarily done as an additional check in ensuring the correct calibration of ***MotorCAD*** and to check the motor thermal capability level. This is because as mentioned earlier, in a stall case, only copper losses exist. However, running the motor at a particular speed (other than zero speed) yields additional losses, such as: bearing, windage, hysteresis and iron loss. Such losses and the predicted FEA magnetic losses were then inputted into ***MotorCAD*** so that the temperature profiles of various load cases could be obtained and compared with the experimental results. Therefore, the agreement of the experimental data to that predicted by ***MotorCAD*** would inherently mean that the losses defined in the above section were segregated correctly. The result of this analysis at speed of 200 rpm and torque at 20 Nm can be seen in the Figure 6-14 and Table 6-7 below:

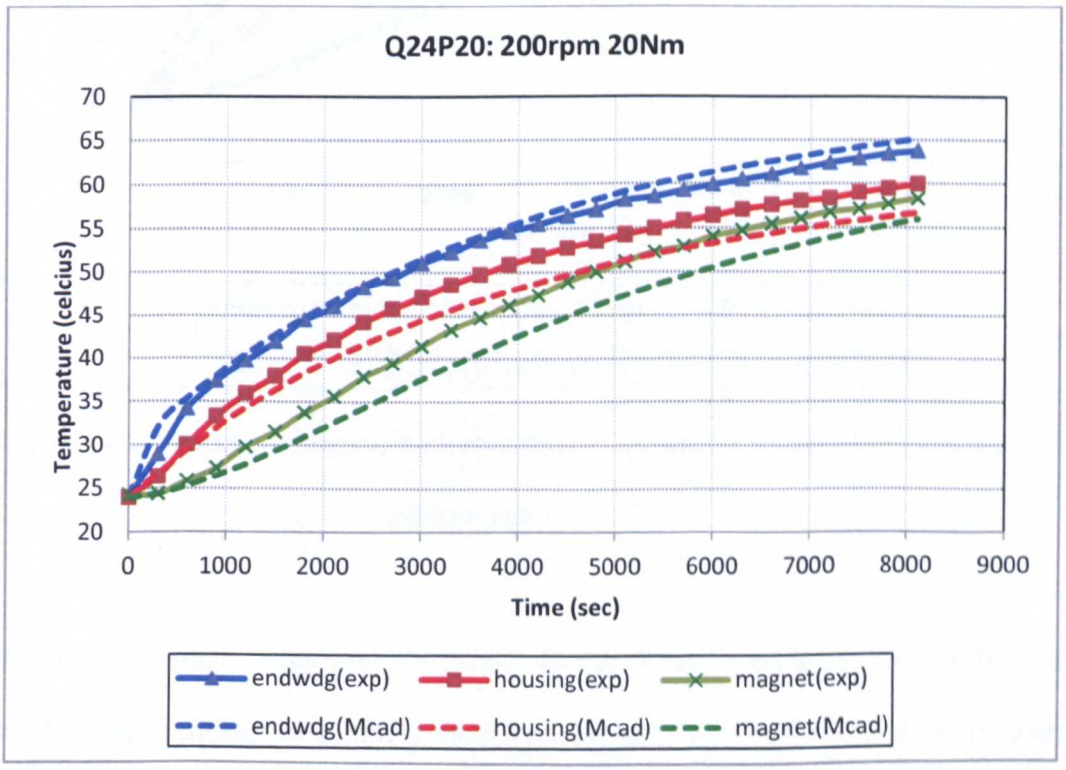

Figure 6-14: Direct comparison between MotorCAD and experimental result at speed 200rpm and torque 20Nm

The model was said to be correctly calibrated due to the fact that both the gradient (thermal capacitance) as well as the steady state temperatures has been well matched for several separate scenarios – 10Nm, 15Nm and 20Nm stall. The model was also calibrated for two additional scenarios – a 200rpm 20Nm and a 200rpm 35Nm. These were to ensure that the loss data was correctly being predicted through FEA method.

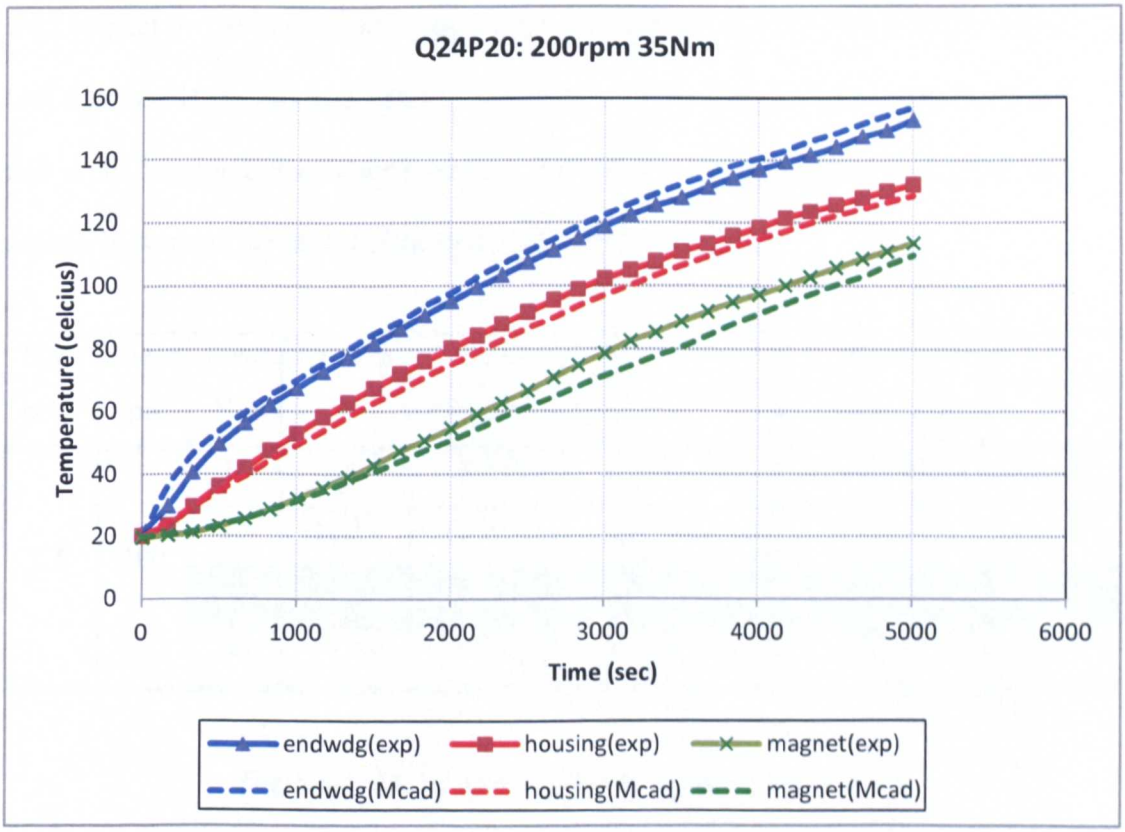

Figure 6-15: Direct comparison between MotorCAD and experimental result at speed 200rpm and torque 35N

Therefore, through these three distinct scenarios, it was concluded that the thermal model was sufficient to simulate the actual motor. This was desirable, since great time saving was accomplished, since experimental tests were no longer required, as the thermal model could efficiently predict the motor temperatures. The result in

Table 6-5 clearly indicates the motors torque against thermal capability. However, there are certain considerations to be taken in examining the thermal capability of the motor. The motor was simulated at various loads level for 2.5 hours continuously and the final temperature of the critical components such as winding and magnet were measured. The percentage shown in table below represents the predicted temperature of the mentioned components at the end of the simulation duration at various loads with respect to the maximum rating of the winding and magnet which are at 180°C (453K)(class H rating) and 180°C respectively. It can be observed from Table 6-5 that at 40 Nm load, the motor's winding has reached its' maximum rating and will definitely damage the motor if the operation is still on.

Time hour	Speed rpm	Load Nm	Current A	Winding degC(Kelvin)	Percentage	Magnet degC(Kelvin)	Percentage
2.5	200	20	7.87	65(338)	74.61%	57(330)	72.85%
		30	11.81	128(401)	88.52%	104(377)	83.22%
		35	13.78	147(420)	92.72%	118(391)	86.31%
		40	15.75	189(462)	101.99%	150(423)	93.38%

Table 6-5: Thermal capability level of the motor

Location	Experimental Data (Kelvin)				MotorCAD Data (Kelvin)				Percentage Different			
	t =0.5hr	t =1hr	t =1.5hrs	t =2hrs	t =0.5hr	t =1hrs	t =1.5hrs	t =2hrs	t =0.5hr	t =1hr	t =1.5hrs	t =2hrs
End Winding	321.45	328.85	334.25	338.75	320.05	328.68	335.11	339.9	0.44%	0.05%	0.26%	0.34%
Housing	318.25	325.65	331.05	334.55	314.86	322.89	328.79	333.16	1.07%	0.85%	0.68%	0.42%
Magnet	312.05	320.65	327.25	331.65	309.36	317.68	325.19	331.22	0.86%	0.93%	0.63%	0.13%

Table 6-6: Direct Comparison between Experimental and Simulated Results for a 20Nm Stalled Motor

Location	Experimental Data (Kelvin)				MotorCAD Data (Kelvin)				Percentage Different			
	t =0.5hr	t =1hr	t =1.5hrs	t =2hrs	t =0.5hr	t =1hr	t =1.5hrs	t =2hrs	t =0.5hr	t =1hr	t =1.5hrs	t =2hrs
End Winding	317.75	326.85	331.75	335.65	318.06	327.35	333.11	336.89	0.10%	0.15%	0.41%	0.37%
Housing	313.75	322.95	328.15	331.55	311.53	320.02	325.21	328.6	0.71%	0.91%	0.90%	0.89%
Magnet	306.95	317.95	325.45	329.95	304.21	313.94	321.69	327.13	0.89%	1.26%	1.16%	0.85%

Table 6-7: Direct comparison between MotorCAD and experimental result at speed 200rpm and torque 20Nm

Location	Experimental Data (Kelvin)				MotorCAD Data (Kelvin)				Percentage Different			
	t =0.25hr	t =0.5hr	t =1hr	t =1.25hr	t =0.25hr	t =0.5hr	t =1hr	t =1.25hr	t =0.25hr	t =0.5hr	t =1hr	t =1.25hr
End Winding	335.27	364.02	404.66	417.6	338.56	367.16	408.65	421.9	0.98%	0.86%	0.99%	1.03%
Housing	320.68	349.22	386.66	399.04	317.69	344.26	382.57	395.55	0.93%	1.42%	1.06%	0.87%
Magnet	302.05	324.05	365.25	378.95	302.05	320.77	357.62	373.75	0.00%	1.01%	2.09%	1.37%

Table 6-8: Direct comparison between MotorCAD and experimental result at speed 200rpm and torque 35Nm

Chapter 7

Conclusion and Further Work

7.1 Conclusion

The purpose with this thesis was to design and optimize a permanent magnet synchronous motor for an aircraft actuator application. Some choices have been made in order to restrict the extension of the work. A BLDC motor with a concentrated winding was expected to fulfil the requirements. An extensive comparison between BLDC and BLAC motors for the specific application has been made.

During the design stage, all the parameters have been analytically determined and the motor models were verified through simulation in the finite element software, ***Magnet***, in order to predict the induced back EMF and the produced loading torque. According to the used analytical models, the suggested machine design fulfils the requirements. This was also confirmed with finite element method (FEM) simulations and experimental results. Thus, the results showed acceptable correlation between the three methods; analytical, simulation and experimental.

Models for the different losses in the machine have been developed and implemented into the design stage. In addition to the copper losses, iron losses as well as bearing losses and windage losses are also considered. Special attention was given to analyse

a thermal model used in order to predict temperatures in different parts of the motor and to determine the motor capability.

Attention was also given to the calculation of the mechanical stress on the magnets, leading to requirements of the bandage or adhesive application. Calculations on mechanical stress and centrifugal forces due to high rotational speed deem necessary before selecting an appropriate method to retain the magnets. The initial glass-fibre bandage failed to withstand these forces due to improper selection of the undersized dimension of the sleeve. The structural magnet bonding adhesive had been replaced as the retaining method and its tensile strength was capable to uphold the speed more than 345% of the rated speed.

Basic drive systems for the both type of motor have been described and possible requirements on torque and speed controls were also considered. Detailed Simulink models for a PMSM and BLDC drive systems with vector current and hysteresis current controller respectively have been developed and operation on rated requirement have been studied. Simulink has been chosen due to its flexibility and mathematical models or even a model from FEM software can be easily incorporated in the simulation and the presence of numerous tool boxes and support guides simplifies the simulation of large system. A speed controller has been designed successfully for closed loop operation for both PMSM and BLDC drive systems so that the motor runs at the commanded or reference speed. The simulated system has a fast response with practically zero steady state error thus validating the design method of the speed controller.

A comparative study has been made of those two current controller schemes in terms of switching frequency, speed error and current control ability. This study proves that vector current controllers are better than hysteresis current controllers because of having constant switching frequency and lower THD of the current waveforms. The error between the speed command and the actual speed is also greatly reduced. Hysteresis current controllers have a variable switching frequency that depends of the hysteresis band and if the bandwidth is very small it may affect the device switching capability. However, the simulation with hysteresis current controller allows faster simulations with reduced time and computational resources and at the same time generates torque ripple.

The design and construction of the prototype been carried out and is described in Chapter 5. It is specifically built to study the performance of the proposed motor. The motor drives for PMSM have been constructed and the performance of the system with the proposed testing condition is analyzed in Chapter 6 above.

From the comparison between the practical and simulation work, it can be concluded that the experimental results are in good agreement with the simulation. The motor shows excellent performance and able to satisfy the required specification. However, there were slight errors between experimental and simulated results probably due to certain losses which are not included in the simulation model such as thermal losses and imperfection on the prototype especially on the lamination steels.

7.2 Suggestions for Further Work

An important element of tests which has not been performed is the evaluation of BLDC real performance. It is advisable to carry out such tests in order to confirm and verify the predicted performance data. For these experiments the hysteresis current controller drive should be constructed and implemented especially in aiming for a considerably simpler and cheaper drive.

Furthermore, the implementation of fault tolerance test setup would be interesting as the machine is expected to be capable of operating over fault condition. This had been successfully carried out for PMSM and to test the full capability of the developed system with BLDC should also be considered.

When examining the machine thermal capability, a suitable constructed motor with corresponding measurement devices should be implemented as to monitor the motor condition while running. A more sophisticated and high-resolution monitoring devices can be implemented on each part of the targeted motor components.

References

[1] George Ellis, "Advances in Brushless DC Motor Technology,Control, and Manufacture",Kollmorgen Corporation, Radford, Virginia, USA, 1996

[2] Ward Brown, "Brushless DC Motor Control Made Easy", Microchip Technology Incorporated, 2002

[3] "Modern Electric Motors", ThinGap Corporation, 2001-2004

[4] T.J.E Miller, "Electronic Control of Switched Reluctance Machines," Newnws, 2001

[5] T.J.E Miller, "Brushless Permanent-Magnet and Reluctance Motor Drives," Oxford Science Publication, 1989

[6] Magnussen F., Sadarangani C., "Winding factors and Joule losses of permanent magnet machines with concentrated windings", Proc. IEEE International Electric Machines and Drives Conference, Madison, USA, June 1-4, 2003

[7] Magnussen F., Thelin P., Sadarangani C., "Performance evaluation of permanent magnet synchronous machines with concentrated and distributed windings including the effect of field-weakening", Proc. IEEE International Conference on Power Electronics, Machines and Drives,Edinburgh, UK, March 31-April 2, 2004

[8] Jabbar, M.A.; Yeo, S.W., "A new architecture of design software for electric motors", Electrical and Computer Engineering, 2000 Canadian Conference, March 7-10, 2000

[9] Cros, J.Viarouge P., "Synthesis of high performance PM motors with concentrated windings", Energy Conversion, IEEE Transactions onVolume 17, Issue 2, June 2002

[10] Cros, J.,Viarouge, P. "Synthesis of high performance PM motors with concentrated windings", Electric Machines and Drives, 1999. International Conference IEMD '99, May 9-12, 1999

[11] George Ellis, "Advances in Brushless DC Motor Technology,Control, and Manufacture",Kollmorgen Corporation, Radford, Virginia, USA, 1996

[12] Prof G.M. Asher, "Module of Induction Motor Drives H5DIMD, University of Nottingham. http://hermes.eee.nott.ac.uk/cal/h54IMD.

[13] Pillay, P., Krishnan, R., "Application characteristics of permanent magnet synchronous and brushless DC motors for servo drives" Industry Applications, IEEE Transactions Volume 27, Issue 5, Sept.-Oct. 1991.

[14] Keith Bradley, "Module of Special Drive H5DSPD", University of Nottingham

[15] A Moussi, A Torki, "An Improved Efficiency Permanent Magnet Brushless DC Motor PV Pumping System", LARHYSS Journal, 2002

[16] S.E. Lyshevski, "Electromechanical System And Devices", CRC Press, 2008.

[17] P. L. Chapman, "The Power Electronics Handbook", CRC Press LLC, 2002

[18] C. Gerada, "Permanent Magnet Synchronous machines for Saliency-based, Self-Sensored Motion Control", The 33rd Annual Conference of the IEEE Industrial Electronics Society (IECON), Nov. 5-8, 2007, Taipei, Taiwan

[19] Arshad, W.M., Chin, Y.K., Soulard, J., Bäckström, T.,Östlund, S., Sadarangani, C., On Finding Compact Motor Solutions for Transient Applications,IEMDC'2001, Cambridge, MA USA.

[20] Chandur Sadarangani, Electrical machines – Design and Analysis of Induction and Permanent MagnetMotors, KTH 2000

[21] T.J.E Miller, "Brushless Permanent-Magnet and Reluctance Motor Drives," Oxford Science Publication, 1989

[22] Duane C. Hanselman, "Brushless Permanent Magnet Motor Design"The Writers' Collective, 2006

[23] T. Li and G. Slemon, "Reduction of cogging torque in permanent magnet motors," IEEE Trans. Magn., vol. 24, pp. 2901–2903, Nov. 1988.

[24] C. Mi and G. Slemon, "Modeling of Iron Losses of Permanent-Magnet Synchronous Motors" IEEE Transactions on Industry Applications, vol. 39, No. 3, May/June 2003.

[25] J.F. Gieras, Mitchell Wang, "Permanent Magnet Technology – Design and Application" Second Edition, Marcel Dekker, Inc, 2002

[26] T. Ishikawa and G. Slemon, "A method to reduce ripple torque in permanent magnet motors without skewing," IEEE Trans. Magn., vol. 29, pp. 2028-2031, Mar. 1993.

[27] N. Bianchi, M. Dai Pr´e, G. Grezzani, and S.Bolognani, " Magnetic loading of fractional-slot three–phase PM motors with non-overlapped coils" Industry Applications Conference, 2006. 41st IAS Annual Meeting, 2006

[28] N. Bianchi and M. Dai Pr´e. "Use of the star of slots in designing fractional–slot single–layer synchronous motors." IEE Proc. – Electr.Power Appl., 2006.

[29] Z.Q Zhu, "Notes on Development of Novel Fractional Slot PM Motors" University of Sheffield.

[30] P.C. Sen, "Principles of Electric Machines And Power Electronic", Second Edition, Wiley, 1997

[31] Z. Q. Zhu, D. Howe, E. Bolte, and B. Ackermann, "Instantaneous magnetic field distribution in brushless permanent magnet dc motors—part I: open-circuit field", IEEE Trans. Magnetics, vol. 29, no. 1, pp. 124–136, 1993.

[32] Z. Q. Zhu and D. Howe, "Instantaneous magnetic field distribution in brushless permanent magnet dc motors—part II: armature reaction field", IEEE Trans. Magnetics, vol. 29, no. 1, pp. 136–142, 1993.

[33] J. Wang, Z. P. Xia, and D. Howe, "Three-Phase Modular Permanent Magnet Brushless Machine for Torque Boosting on a Downsized ICE Vehicle", IEEE transactions on vehicular technology, vol. 54, no. 3, pp. 809-816, 2005

[34] F. Caricchi, T.A Lipo "Innovative Inverter Topology For Concentrated Winding PM Motor Drives", Electrical Engineering Dept, University of Rome, 1992

[35] C. Mejuto, A. Mebarki, D. Staton, N. Al-Khayat, and M. Mueller, "Thermal modelling of TEFC alternators," in IEEE Industrial Electronics, IECON 2006 - 32nd Annual Conference.

[36] D. G. Dorrell, D. A. Staton, J. Kahout, D. Hawkins, and M. I. McGilp, "Linked Electromagnetic and Thermal Modelling of a Permanent Magnet Motor," Univerity of Glasgow, Glasgow, UK.

[37] A. Tassi, G. Zanocchi, and D. Staton, "FEM and Lumped Circuit Thermal Analysis of External Rotor Motor," in IEEE Industrial Electronics, IECON 2006 - 32nd Annual Conference.

[38] D. A. Staton and A. Cavagnino, "Convection Heat Transfer and Flow Calculations Suitable for Analytical Modelling of Electric Machines," IEEE, 2006.

[39] D. Staton, S. Pickering, and Desmond Lampard, University of Nottingham, "Recent Advancement in the Thermal Design of Electric Motors," SMMA 2001 Fall Technical Conference "Emerging Technologies for Electric Motion Industry", Durham, North Carolina, USA, pp. 3-5 Oct 2001.

[40] P. H. Mellor, D. Roberts, and D. R. Turner, "Lumped parameter thermal model for electrical machines of TEFC design," IEE Proceedings - B, vol. 138, September 1991.

[41] A. Boglietti, A. Cavagnino, and D. A. Staton, "TEFC Induction Motors Thermal Models: A Parameter Sensitivity Analysis," IEEE Transactions on Industry Applications, vol. 41, May/June 2005.

[42] A. Boglietti, A. Cavagnino, and D. Staton, "Determination of Critical Parameters in Electrical Machine Thermal Models," in 42nd Annual Meeting of the IEEE-Industry-Applications-Society, New Orleans, LA, 2007, pp. 1150-1159.

[43] H.P. Liu, V. Lelos, and C.S. Hearn, Center for Electromechanics, The University of Texas at Austin, "Transient 3-D Thermal Analysis for an Air-Cooled Induction Motor," IEEE., 2005.

[44] C. Micallef, S. J. Pickering, K. A. Simmons, and K. J. Bradley, "An Alternative Cooling Arrangement for the End Region of a Totally Enclosed Fan Cooled (TEFC) Induction Motor," in Power Electronics, Machines and Drives, 2008. PEMD 2008. 4th IET Conference.

[45] A. Boglietti, A. Cavagnino, D. Staton, M. Shanel, M. Mueller, and C. Mejuto, "Evolution and Modern Approaches for Thermal Analysis of Electrical Machines," IEEE Transactions on Industrial Electronics, vol. 56, March 2009.

[46] J. Mugglestone, D. Lampard, and S. J. Pickering, "Effects of end winding porosity upon the flow field and ventilation losses in the end region of TEFC induction machines," IEE Proc.-Electr. Power Appl., vol. 145, September 1998.

[47] Keith Bradley, "Module of Special Drive H5DSPD", University of Nottingham.

[48] P. L. Chapman, "The Power Electronics Handbook", CRC Press LLC, 2002.

[49] P.C. Sen, "Principles of Electric Machines And Power Electronic", Second Edition, Wiley, 1997

[50] "Neodymium-Iron-Boron Permanent Magnets", http://www.arnoldmagnetics.com/Content1.aspx?id=5062

[51] Ch. Schatzer, A. Binder.; "Design optimization of a high-speed permanent magnet machine with the VEKOPT algorithm", Industry Applications Conference, 2000.

[52] "Kevlar® Aramid Fiber Technical Guide."http://www2.dupont.com

[53] http://www.fdsims.com/Polyester200RoundWire.htm

[54] "Operating Manual Electric Motor High Speed Test Rig", Torquemeters Ltd, 2007

[55] C. Gerada, K. Bradley, "Integrated PM Machine Design for an AircraftEMA," IEEE Trans. on Ind. Elec., vol.55, No.9, pp.3300 - 3306, September 2008.

[56] O. Jasim, C. Gerada, M. Sumner, and J. Arellano-Padilla,"Investigation of Induction Machine Phase Open Circuit Faults Using a Simplified Equivalent Circuit Model," The International Conference on Electrical Machines, ICEM2008, Vilamoura, Portugal, 2008.

Appendix A **Flow of Design Procedure**

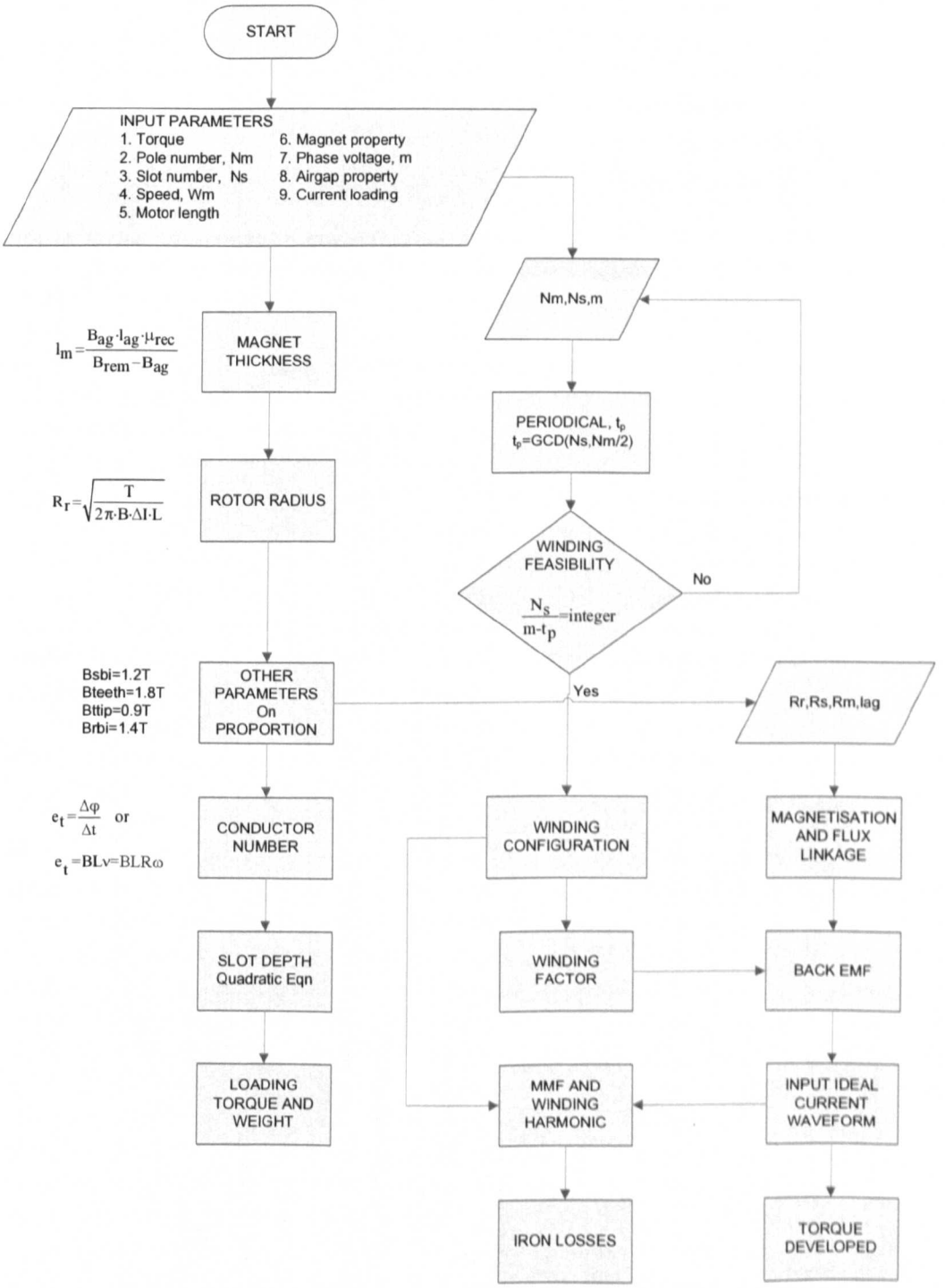

Appendix B **Parameters Calculation**

Appendix B: Parameters Calculation

The parameters are given for the STAR connected BLDC motor are as below

$\phi_{shaft} := 0.0635$ Shaft diameter

$T := 40$ Torque in N-m

$N_m := 800$ motor speed in rpm

$B_{rem} := 1.04$ Magnet remenance Tesla

$H_c := 755 \cdot 10^{3}$ Magnet Coercivity A/m

$\mu_o := 4\pi \cdot 10^{-7}$ Air permeability

$\mu_m := \frac{B_{rem}}{H_c}$ $\mu_m = 0$

$\mu_{rec} := \frac{\mu_m}{\mu_o}$ $\mu_{rec} = 1.0962$ Magnet permeability

$B_{ag} := 0.7$ Required Air gap field density

$l_{ag} := 0.001$ Air gap length

$l_R := 0.1$ Motor radial length

$d_{slot} := 0.002$ Tooth tip thickness

$w_{slot} := 0.0036$ slot openning

$k_{ff} := 0.68$ Fill factor

$N_{mag} := 16$ Number of magnet poles

$N_s := 24$ Number of slots

$E_{ph} := 145$ The back-EMF of the motor

TRV := 80 Design torque rotor volume in kN/m^3

ΔI := 50 Current loading in kAmps/m

Calculation method

Use Hmlm + Haglag =0 assume Bag=Bm i.e Aag=Am

Hmlm + Bm/ μo lag =0 Hm = -lag/lm * Bm/ μo

Bm = Brem + μmHm Bm = Brem - lag/lm * μm/μo * Bm

Bm = Brem/ (1 + lag/lm * μm/μo) Bm = Brem/ (1 + lag/lm * μrecoil* μo /μo)

Rephrase lm = Bm * lag * μrecoil / (Brem - Bm)

To calculate magnet thickness

$$l_{mcalc} := \frac{B_{ag} \cdot l_{ag} \cdot \mu_{rec}}{B_{rem} - B_{ag}}$$

$l_{mcalc} = 0.0023$ magnet thickness in m

let $l_m := 0.003$

To determine rotor radius

$$R_{si} := \sqrt{\frac{T}{\Delta I \cdot B_{ag} \cdot 2\pi \cdot l_R \cdot 1000}}$$

$R_{si} = 0.04265$ Inner stator radius

$R_{si} := 0.043$

$R_{ro} := R_{si} - l_{ag}$ $R_{ro} = 0.042$ Outer rotor radius

$\theta_p := 2\frac{\pi}{N_{mag}}$	$\theta_p = 0.3927$	pole pitch in radian
$\theta_s := 2\frac{\pi}{N_s}$	$\theta_s = 0.2618$	slot pitch in radian
$\lambda_p := \theta_p \cdot R_{ro}$	$\lambda_p = 0.0165$	pole span in m
$\lambda_s := \theta_s \cdot R_{ro}$	$\lambda_s = 0.011$	slot span in m
$T_{tw} := \theta_s \cdot R_{si} - w_{slot}$	$T_{tw} = 0.0077$	Tooth tip width

To determine the tooth and back iron sizes are based on the following proportion

$B_{teeth} := 1.3$		Back iron density
$B_{ttip} := 0.7$		Teeth tip Flux density
$B_{sbi} := 1.4$		Stator back iron flux density
$B_{rbi} := 1.2$		Rotor back iron flux density
$T_w := \frac{B_{ttip}}{B_{teeth}} \cdot T_{tw}$	$T_w = 0.00412$	Tooth width in m
	$T_w := 0.004$	Actual Tooth width in m
$L_{sbi} := \frac{B_{teeth}}{B_{sbi}} \cdot T_w$	$L_{sbi} = 0.0037$	Stator back iron length
$L_{sbi} := 0.007$		To adjust to Chris's motor
$L_{rbi} := \frac{B_{teeth}}{B_{rbi}} \cdot T_w$	$L_{rbi} = 0.0043$	Rotor back iron length

To calculate the motor power and phase current

$\omega_m := N_m \cdot 2\frac{\pi}{60}$	$\omega_m = 83.7758$	Speed in rad/s
$P := T \cdot \omega_m$	$P = 3351.0322$	motor power
$i_{ph} := T \cdot \frac{\omega_m}{2 \cdot E_{ph}}$	$I_{ph} = 11.5553$	phase current in Amp
$Ipk := \sqrt{\frac{3}{2}} \cdot i_{ph}$	$Ipk = 14.1523$	RMS current

To determine number of conductor

$\Delta\Phi_{tooth} := B_{ag} \cdot \lambda_s \cdot l_R$	$\Delta\Phi_{tooth} = 0.0008$	Flux at a tooth in wb
$\Delta t := \frac{60}{N_m \cdot N_s}$	$\Delta t = 0.0031$	time/tooth in s
$volt_{cond} := \frac{\Delta\Phi_{tooth}}{\Delta t}$	$volt_{cond} = 0.2463$	volt per conductor
$e_t := B_{ag} \cdot l_R \cdot \omega_m \cdot R_{ro}$	$e_t = 0.2463$	volt per conductor based on TJ Miller equation
$Z_{ph} := \left(\frac{E_{ph}}{volt_{cond}}\right)$	$Z_{ph} = 588.7109$	number of conductor per phase
$Zt := \left(3 \cdot \frac{Z_{ph}}{N_s}\right)$	$Zt = 73.5889$	One phase occupy one third of total number of slots. Number o conductor per tooth

$$P_{poles} := \frac{T}{2 \cdot Zt \cdot (B_{ag} \cdot l_R \cdot R_{ro}) \cdot i_{ph}} \qquad P_{poles} = 8$$

To determine the slot depth

Try to limit the current density per slot at 12Arms/mm^2

$\Delta_i := 12$ current density per slot A/mm^2

$A_{cond} := \frac{i_{ph}}{\Delta_i}$ $A_{cond} = 0.9629$ copper area for a single conductor in mm^2

$A_{cu} := A_{cond} \cdot Zt$ $A_{cu} = 70.8617$ Required copper area of slot

$A_{slot} := \frac{A_{cu}}{k_{ff}}$ $A_{slot} = 104.2084$ Slot area with the slot fill factor

Calculation of slot height by quadratic

$A := \frac{\pi}{N_s}$ $B := \frac{1000\left[2\pi(R_{si} + d_{slot}) - T_w \cdot N_s\right]}{N_s}$ $C := -A_{slot}$

$A = 0.1309$ $B = 7.781$ $C = -104.2084$

$slot_{depth1} := \frac{-B + \sqrt{B^2 - 4 \cdot A \cdot C}}{2 \cdot A}$ $slot_{depth1} = 11.2598$

$slot_{depth1} := 15$ Actual slot depth

+

$slot_{depth2} := \frac{-B - \sqrt{B^2 - 4 \cdot A \cdot C}}{2 \cdot A}$ $slot_{depth2} = -70.7021$

$$Ratio := \frac{A_{slot}}{T_w \cdot slot_{depth1} \cdot 10^3}$$ Ratio = 1.7368

To determine others parameters

$R_{so} := R_{si} + slot_{depth1} \cdot 10^{-3} + L_{sbi} + d_{slot}$ $R_{so} = 0.067$ Stator outer radius

$R_{slo} := R_{so} - L_{sbi}$ $R_{slo} = 0.06$ Stator outer slot radius

$W_{slo} := R_{slo} \cdot \theta_s - T_w \cdot 10^{-3}$ $W_{slo} = 0.0157$ Outer slot width

$R_{ri} := R_{ro} - l_m - L_{rbi}$ $R_{ri} = 0.0347$ Inner rotor radius

To find torque density per volume

$V_{motor} := \pi R_{ro}^2 \cdot l_R$ $V_{motor} = 0.0006$ Motor volume in m^3

$\Delta_{torque} := \frac{T}{V_{motor}}$ $\Delta_{torque} = 72179.1125$ Torque density in N/m^3

To calculate resistance

$\sigma := 57.7 \cdot 10^6$

$z_{turn} := 2 \cdot \pi \cdot \frac{R_{slo}}{N_s}$ $z_{turn} = 0.0157$

$l_{cu} := Zt \cdot (\pi \cdot z_{turn} + l_R) \cdot 8$ $l_{cu} = 87.9228$

$Rph := \frac{l_{cu}}{\sigma \cdot A_{cond} \cdot 10^{-6}}$ $Rph = 1.5824$

$P_{loss} := 2 i_{ph}^2 \cdot Rph$ $P_{loss} = 422.5884$

Result of the parameters

$R_{ri} = 0.0347$	$L_{rbi} = 0.0043$	$T_{tw} = 0.0077$	$W_{slo} = 0.0157$
$R_{ro} = 0.042$	$l_m = 0.003$	$T_w = 0.004$	$slot_{depth1} =$ ▮
$R_{si} = 0.043$	$l_{ag} = 0.001$	$\lambda_p = 0.0165$	
$R_{so} = 0.067$	$L_{sbi} = 0.007$	$\lambda_s = 0.011$	

Appendix C Slot Area and Winding Resistance Determination

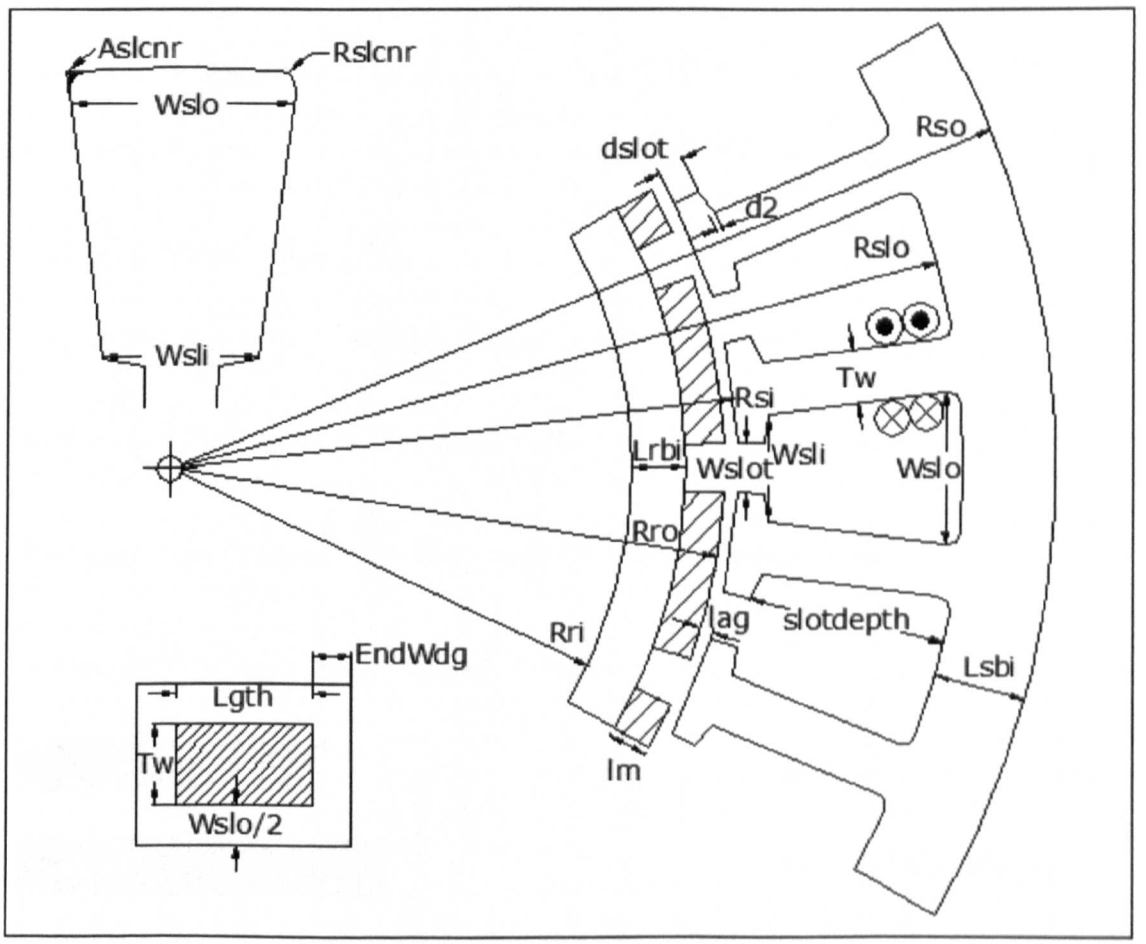

$N_s := 24$ $T_w := 4mm$ $Nturn := 38$

$slot_{depth} := 15mm$ $\theta_s := 2\frac{\pi}{N_s}$ $w_{slot} := 3.6mm$

$d_{slot} := 2mm$ $R_{si} := 43mm$ $Lgth := 105.6mm$

$$d2 := 0.5\left[\left[\left(\theta_s\right)\cdot\left(R_{si} + d_{slot}\right) - w_{slot} - T_w\right]\cdot\tan\left(15\frac{\pi}{180}\right)\right] \qquad d2 = 5.601441\times 10^{-4}\,m$$

$R_{slo} := R_{si} + slot_{depth} + d_{slot} + d2$ $R_{slo} = 0.06056m$ Stator outer slot radius

$W_{slo} := R_{slo}\cdot\theta_s - T_w$ $W_{slo} = 0.011855m$ Outer slot width

$W_{sli} := \left(R_{si} + d_{slot} + d2\right)\cdot\theta_s - T_w$ $W_{sli} = 7.927618\times 10^{-3}\,m$ Inner slot width

$R_{slcnr} := 2mm$ $A_{slcnr} := \left[\left(R_{slcnr}^{\,2} - 0.25\pi\cdot R_{slcnr}^{\,2}\right)\cdot 2\right]$ $A_{slcnr} = 1.716815\times 10^{-6}\,m^2$

$$Aslot := \left[\frac{\pi}{N_s}\cdot\left[\left(R_{si} + d_{slot} + d2 + slot_{depth}\right)^2 - \left(R_{si} + d_{slot} + d2\right)^2\right] - T_w\cdot slot_{depth}\right] - A_{slcnr}$$

$$Aslot_{quadr} := \frac{\pi}{N_s}\cdot slot_{depth}^{\,2} + \left[\frac{2\pi}{N_s}\cdot\left(R_{si} + d_{slot} + d2\right) - T_w\right]\cdot slot_{depth} - A_{slcnr}$$

$$Aslot_{trapz} := \left[0.5\cdot\left(W_{slo} + W_{sli}\right)\cdot\left(slot_{depth}\right)\right] - A_{slcnr}$$

$Aslot = 1.466499\times 10^{-4}\,m^2$ Slot Area

$Aslot_{quadr} = 1.466499\times 10^{-4}\,m^2$ Slot Area Quadratic Eqn

$Aslot_{trapz} = 1.466499\times 10^{-4}\,m^2$ Slot Area Trapezoidal Eqn

$EndWdg := 35mm$

$strand := 2$

$Dcond := 0.914mm$

Wire specification values from FD

$D_{insul} := 1.008mm$

Sim swg20 grade2

$Acond := \pi \cdot \left(\frac{Dcond}{2}\right)^2$ $\quad Acond = 6.561185 \times 10^{-7} m^2$

$A_{wire} := \pi \cdot \left(\frac{D_{insul}}{2}\right)^2$ $\quad A_{wire} = 7.980148 \times 10^{-7} m^2$

$Acu := 2 \cdot Nturn \cdot Acond \cdot strand$ $\quad Acu = 9.973001 \times 10^{-5} m^2$

$A_{wiretotal} := 2 \cdot Nturn \cdot A_{wire} \cdot strand$ $\quad A_{wiretotal} = 1.212982 \times 10^{-4} m^2$

$SFFcu := \frac{Acu}{Aslot}$ $\quad SFFcu = 0.680055$

$SFFwire := \frac{A_{wiretotal}}{Aslot}$ $\quad SFFwire = 0.827128$

To calculate resistance

$\sigma := 57.7 \cdot 10^6 \frac{1}{\Omega \cdot m}$ copper conductivity

$Phase := 3$

$Lwdg := \left[Lgth + 2 \cdot EndWdg + T_w + \left(\frac{W_{slo} + W_{sli}}{2}\right)\right] \cdot 2 \cdot strand \cdot Nturn \cdot N_s$ $\quad Lwdg = 691.263581m$

$R_{ph} := \frac{Lwdg}{\sigma \cdot Acond \cdot strand^2 \cdot Phase}$ $\quad R_{ph} = 1.521613\Omega$

$Rph := \frac{Lwdg \cdot 0.0269}{strand \cdot Phase \cdot 2}$ $\quad Rph = 1.549583m$

Appendix D Open Circuit Magnetic Field Analysis for Q24P20

$Br := 1.140$	$Brm := 1.18 - 1.2$	Magnet remenance Tesla (Chris)
$H_c := 81197$	$Hcm := 86000$	Magnet Coercivity A/m(Chris)
$\mu_o := 4\pi \cdot 10^{-7}$		Permeability of free space
$\mu_m := \frac{Br}{H_c}$	$\mu_m = 1.405 \times 10^{-6}$	Magnet recoil
$\mu_r := \frac{\mu_m}{\mu_o}$	$\mu_r = 1.118$	Magnet permeability
$N_s := 24$		no of slot
$p := 20$	$P := \frac{p}{2}$	no of pole
$m := 3$		no of phase
$N_c := N_s$		no of coil equals to no of slot for double layer winding
$N_p := \frac{N_c}{3}$		no of coil per phase
$Pitch := 1$		coil pitch
$N_m := 585$		motor speed
$\omega_m := N_m \cdot 2\frac{\pi}{60}$	$\omega_m = 61.261$	Speed in rad/s
$f := \frac{N_m \cdot P}{60}$	$f = 97.5$	frequency
$I_m := 14.15$	$\frac{5}{f} = 0.051282$	Phase peak current
$Nt := 18$		number of conductor

NICOLA METHOD

GCD program:

$$GCD(x,y) := \begin{cases} y & \text{if } x = 0 \\ GCD(\text{mod}(y,x),x) & \text{otherwise} \end{cases}$$

Here is the greatest common divisor: $GCD(N_s, p) = 4$

$t_p := GCD\left(N_s, \frac{p}{2}\right)$ $\quad t_p = 2$ Periodical

$S_s := \frac{N_s}{t_p}$ $\quad S_s = 12$ Star of slot or no of spokes

$\alpha_{pole} := 2\frac{\pi}{p}$ $\quad \alpha_{pole} = 0.314$ Pole angle in degree

$\alpha_{pole} = 18\text{deg}$

$\alpha_{epole} := \left(\frac{p}{2}\right)\cdot\alpha_{pole}$ $\quad \alpha_{epole} = 180\text{deg}$ 1 pole electrical degree

$\alpha_m := 2\frac{\pi}{N_s}$ $\quad \alpha_m = 0.262$ Slot angle in mech. deg

$\alpha_m = 15\text{deg}$

$\alpha_e := \left(\frac{p}{2}\right)\cdot\alpha_m$ $\quad \alpha_e = 2.618$ Slot angle in elec. deg

$\alpha_e = 150\text{deg}$

$\alpha_{ph} := t_p\cdot\alpha_m$ $\quad \alpha_{ph} = 0.524$ Angle between 2 adjacent phase

$\alpha_{ph} = 30\text{deg}$

$Wdg_{ok} := \frac{N_s}{m\cdot t_p}$ $\quad Wdg_{ok} = 4$ Must be integer

$n := 1,3..500$

$\alpha_p := \alpha_{pole} - \alpha_m$ $\quad \alpha_{p2}(n) := n\cdot\frac{\alpha_m\cdot\pi}{\alpha_{pole}\cdot 2}$ $\quad \alpha_{p2}(1) = 1.309$

$K_p(n) := \cos\left(\frac{n\cdot p\cdot\alpha_p}{2\cdot 2}\right)$ $\quad K_{p2}(n) := \sin(\alpha_{p2}(n))$

$$K_d(n) := \begin{cases} \dfrac{\sin\left(Wdg_{ok}\cdot\frac{n\cdot\alpha_{ph}}{4}\right)}{\frac{Wdg_{ok}}{2}\cdot\sin\left(\frac{n\cdot\alpha_{ph}}{2}\right)} & \text{if } \operatorname{mod}(Wdg_{ok},2) = 0 \\ \dfrac{\sin\left(Wdg_{ok}\cdot\frac{n\cdot\alpha_{ph}}{4}\right)}{Wdg_{ok}\cdot\sin\left(\frac{n\cdot\alpha_{ph}}{4}\right)} & \text{if } \operatorname{mod}(Wdg_{ok},2) \neq 0 \end{cases}$$

$$K_w(n) := K_d(n)\cdot K_p(n)$$

ZHU METHOD

$t := 0, 0.0001 .. \frac{5}{f}$ $\theta := -0.105, 0.001 .. \frac{\pi}{10}$

$\alpha_{mag} := 140$ magnet span

$$\alpha_{pr} := \frac{\alpha_{mag}}{180}$$

$Rr := 0.04$ Rotor radius $l := 0.1$ length

$Rs := 0.047$ Inner stator $Rm := 0.046$ Magnet radius

$$c1 := 2\frac{Br}{\mu_o}\alpha_{pr} \qquad c2 := \frac{\pi\cdot\alpha_{pr}}{2} \qquad Rrs := \frac{Rr}{Rs} \qquad Rms := \frac{Rm}{Rs} \qquad Rrm := \frac{Rr}{Rm}$$

$$p\mu r := \frac{\mu_r + 1}{\mu_r} \qquad n\mu r := \frac{\mu_r - 1}{\mu_r}$$

$$M(n) := c1\cdot\frac{\sin(n\cdot c2)}{n\cdot c2}$$

$p = 20$

$P = 10$

$$a(n) := \frac{2\cdot\mu_o\cdot M(n)}{\mu_r}\cdot\frac{n\cdot P}{(n\cdot P)^2 - 1}\cdot Rms^{n\cdot P+1}$$

$$nn(n) := (n\cdot P - 1) + 2\cdot Rm^{n\cdot P+1} - (n\cdot P + 1)\cdot Rm^{2\cdot n\cdot P}$$

$$d(n) := p\mu r\cdot\left(1 - Rrs^{2\cdot n\cdot P}\right) - n\mu r\cdot\left(Rms^{2\cdot n\cdot P} - Rm^{2\cdot n\cdot P}\right)$$

$$K_b(n) := \frac{\mu_o\cdot M(n)}{\mu_r}\cdot\frac{n\cdot P}{(n\cdot P)^2 - 1}\cdot\left[\frac{(n\cdot P - 1) + 2\cdot\left(\frac{Rr}{Rm}\right)^{n\cdot P+1} - (n\cdot P + 1)\cdot\left(\frac{Rr}{Rm}\right)^{2\cdot n\cdot P}}{\frac{\mu_r + 1}{\mu_r}\cdot\left[1 - \left(\frac{Rr}{Rs}\right)^{2\cdot n\cdot P}\right] - \frac{\mu_r - 1}{\mu_r}\cdot\left[\left(\frac{Rm}{Rs}\right)^{2\cdot n\cdot P} - \left(\frac{Rr}{Rm}\right)^{2\cdot n\cdot P}\right]}\right]$$

$$kb(n) := a(n)\cdot\left(\frac{nn(n)}{d(n)}\right)$$

$$vt(\theta) := \sum_n \left(kb(n)\cdot\cos\left(n\cdot P\cdot\theta\right)\right)$$

$$r := Rs$$

$$f_{br}(n) := \left(\frac{r}{Rs}\right)^{n\cdot P-1}\cdot\left(\frac{Rm}{Rs}\right)^{n\cdot P+1} + \left(\frac{Rm}{r}\right)^{n\cdot P+1}$$

$$f_{b\theta}(n) := -\left(\frac{r}{Rs}\right)^{n\cdot P-1}\cdot\left(\frac{Rm}{Rs}\right)^{n\cdot P+1} + \left(\frac{Rm}{r}\right)^{n\cdot P+1}$$

$$B_r(\theta) := \sum_n \left(K_b(n)\cdot f_{br}(n)\cdot\cos\left(n\cdot P\cdot\theta\right)\right) \qquad B_\theta(\theta) := \sum_n \left(K_b(n)\cdot f_{b\theta}(n)\cdot\sin\left(n\cdot P\cdot\theta\right)\right)$$

$\beta_s := 2\frac{\pi}{N_s}$ $\beta_s = 0.262$ $\beta_s = 15\text{deg}$ slot pitch angle

$\beta_p := 2\frac{\pi}{p}$ $\beta_p = 0.314$ $\beta_p = 18\text{deg}$ pole pitch angle

$\beta_{s2} := 2\cdot\frac{P\cdot\beta_p}{N_s}$ $\beta_{s2} = 0.262$

$N_{cp} := \frac{N_s}{m}$ $N_{cp} = 8$ No of conductor per phase

$N_{sp} := \frac{N_s}{m\cdot GCD\left(N_s, p\right)}$ $N_{sp} = 2$ No of spokes per phase

$\theta_d := \left|\frac{\left(\beta_p - \beta_s\right)\cdot\pi}{\beta_p}\right|$ $\theta_d = 0.524$ $\theta_d = 30\text{deg}$ angle displacement of 2 adjacent coils

$$K_{rn}(n) := K_b(n) \cdot f_{br}(n)$$

$$K_{pn}(n) := \sin\left(\frac{n \cdot P \cdot \beta_s}{2}\right)$$ pitch factor

$$K_{dn}(n) := \frac{\sin\left(\frac{n \cdot N_{sp} \cdot \theta_d}{2}\right)}{N_{sp} \cdot \sin\left(\frac{n \cdot \theta_d}{2}\right)}$$ distribution factor

$$K_{wn}(n) := K_{pn}(n) \cdot K_{dn}(n)$$ winding factor

$$\psi_c(t) := 2 \cdot Rs \cdot l \cdot Nt \cdot \left[\sum_n \left[K_{rn}(n) \frac{1}{n \cdot P} K_{pn}(n) \cos\left[n \cdot \left(P \cdot \omega_m \cdot t\right)\right]\right]\right]$$ flux linkage

$$e_{c1}(t) := 2 \cdot Rs \cdot l \cdot Nt \cdot \omega_m \cdot \left[\sum_n \left[K_{rn}(n)\, K_{pn}(n) \sin\left[n \cdot \left(P \cdot \omega_m \cdot t\right)\right]\right]\right]$$ back emf per coil per phase

$$e_{p1}(t) := 2 \cdot Rs \cdot l \cdot Nt \cdot N_{cp} \cdot \omega_m \cdot \left[\sum_n \left[K_{rn}(n)\, K_{pn}(n)\, K_{dn}(n) \cdot \sin\left[\left[n \cdot \left(P \cdot \omega_m \cdot t\right)\right] + n \cdot \left(N_{sp} - 1\right) \cdot \frac{\theta_d}{2}\right]\right]\right]$$

$$e_{p2}(t) := 2 \cdot Rs \cdot l \cdot Nt \cdot N_{cp} \cdot \omega_m \cdot \left[\sum_n \left[K_{rn}(n) \cdot K_{pn}(n) \cdot K_{dn}(n) \cdot \sin\left[\left[n \cdot \left(P \cdot \omega_m \cdot t - \frac{2 \cdot \pi}{3}\right)\right] + n \cdot \left(N_{sp} - 1\right) \cdot \frac{\theta_d}{2}\right]\right]\right]$$

$$e_{p3}(t) := 2 \cdot Rs \cdot l \cdot Nt \cdot N_{cp} \cdot \omega_m \cdot \left[\sum_n \left[K_{rn}(n) \cdot K_{pn}(n) \cdot K_{dn}(n) \cdot \sin\left[\left[n \cdot \left(P \cdot \omega_m \cdot t + \frac{2 \cdot \pi}{3}\right)\right] + n \cdot \left(N_{sp} - 1\right) \cdot \frac{\theta_d}{2}\right]\right]\right]$$

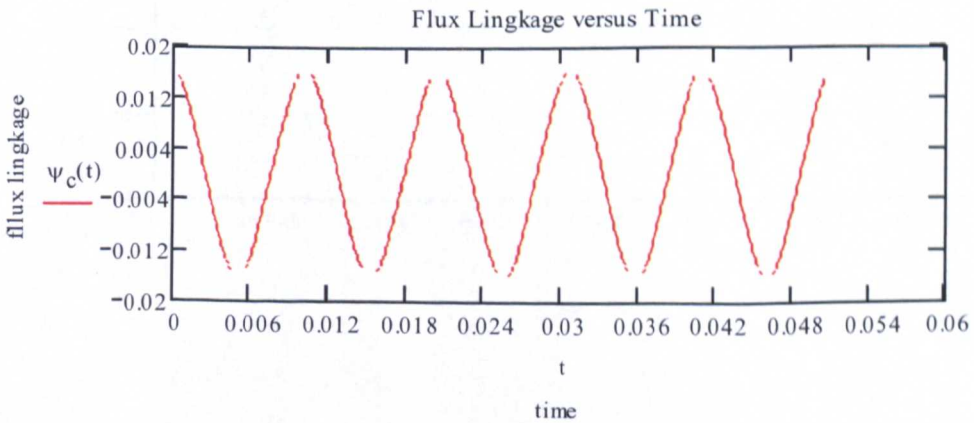

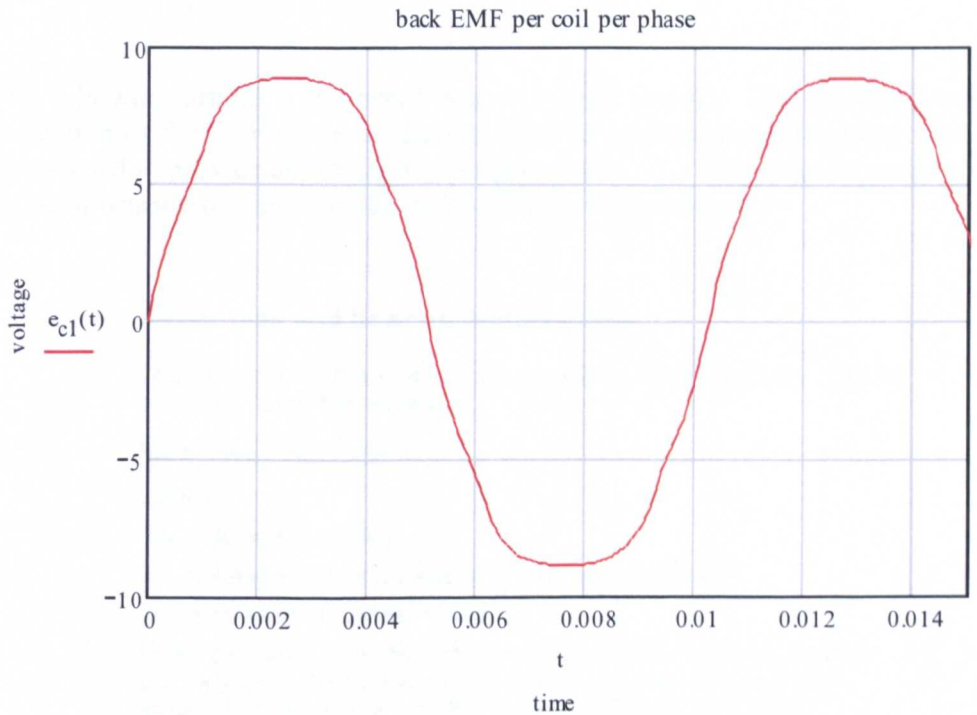
back EMF per coil per phase
10
5
0
−5
−10
voltage
$e_{c1}(t)$
0
0.002
0.004
0.006
0.008
0.01
0.012
0.014
t
time

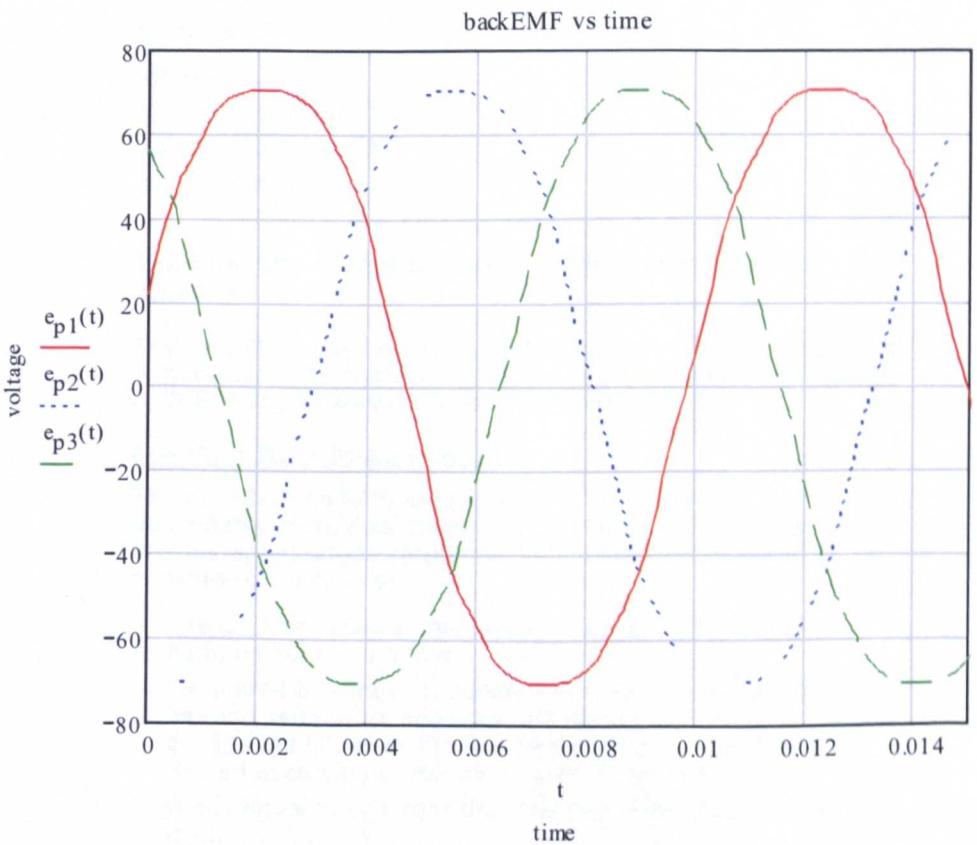
backEMF vs time
80
60
40
20
0
−20
−40
−60
−80
voltage
$e_{p1}(t)$
$e_{p2}(t)$
$e_{p3}(t)$
0
0.002
0.004
0.006
0.008
0.01
0.012
0.014
t
time

Appendix E SKF Model of Bearing Losses Determination

The following article is extracted from the SKF website. The bearing power loss prediction of the SKF model is derived from an advanced computational model and is designed to provide approximate reference values. The power loss in a bearing as a result of bearing friction is obtained by the following relation:

Power loss and bearing temperature

The power loss in a bearing as a result of bearing friction can be obtained using the equation

$N_R = 1{,}05 \times 10^{-4} Mn$

where

N_R = power loss [W]

M = total frictional moment of the bearing [Nmm]

n = rotational speed [r/min

If the cooling factor (the heat to be removed from the bearing per degree of temperature difference between bearing and ambient) is known, a rough estimate of the temperature increase in bearing can be obtained using

$\Delta T = N_R / W_s$

where

ΔT = temperature increase [°C]

N_R = power loss [W]

W_s = cooling factor [W/°C]

The new SKF model for calculation of the frictional moment

The new SKF model for calculating the frictional moment enables a more accurate calculation of the frictional moment generated in SKF rolling bearings according to the equation

$M = M_{rr} + M_{sl} + M_{seal} + M_{drag}$

The new SKF model is derived from more advanced computational models developed by SKF and is designed to provide approximate reference values, under the following application conditions:

- Grease lubrication or normal methods of oil lubrication: oil bath, oil-spot and oil jet.
- For paired bearings, calculate the frictional moment for each bearing separately and then add them up. The radial load is divided equally over the two bearings; the axial load is shared according to the bearing arrangement.
- Loads equal to or larger than the recommended minimum load.
- Constant loads in magnitude and direction.
- Normal operational clearance.

Deep groove ball bearings, single row, low-friction seal on both sides

Product information

Tolerances , see also text
Radial internal clearance , see also text
Recommended fits
Shaft and housing tolerances

Principal dimensions			Basic load ratings		Fatigue load limit	Speed ratings		Mass	Designation
			dynamic	static		Reference speed	Limiting speed		
d	D	B	C	C_0	P_u				* - SKF Explorer bearing
mm			kN		kN	r/min		kg	-
20	42	12	9,95	5	0,212	38000	19000	0,069	**6004-2RSL** *

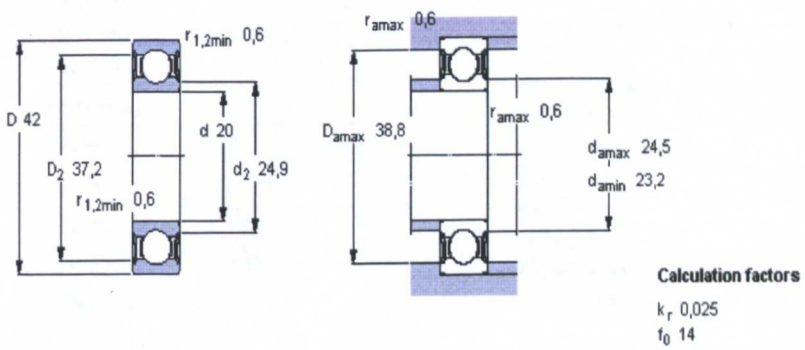

Figure 1: Datasheet of bearings used for the prototyped motor (6004-2RSL)

Table 2: Technical specifications of SKF greases for sealed deep groove ball bearings of carbon chromium steel

Technical specification	SKF greases LHT23	LT10	MT47	MT33	GXN	GWB	LT20	GJN
Thickener	Lithium soap	Lithium soap	Lithium soap	Lithium soap	Polyurea soap	Polyurea soap	Lithium soap	Polyurea soap
Base oil type	Ester oil	Diester oil	Mineral oil	Mineral oil	Mineral oil	Ester oil	Diester oil	Mineral oil
NLGI consistency class	2	2	2	3	2	2 - 3	2	2
Temperature range, °C[1]	-50 to +140	-50 to +90	-30 to +110	-30 to +120	-40 to +150	-40 to +160	-55 to +110	-30 to +150
Base oil viscosity, mm^2/s								
at 40 °C	26	12	70	98	96	70	15	115
at 100 °C	5,1	3,3	7,3	9,4	10,5	9,4	3,7	12,2
Designation suffix	- (LHT23 if not standard)	- (LT10 if not standard)	- (MT47 if not standard)	- (MT33 if not standard)	HT	WT	LT	GJN

Table 1: Technical specifications of SKF greases

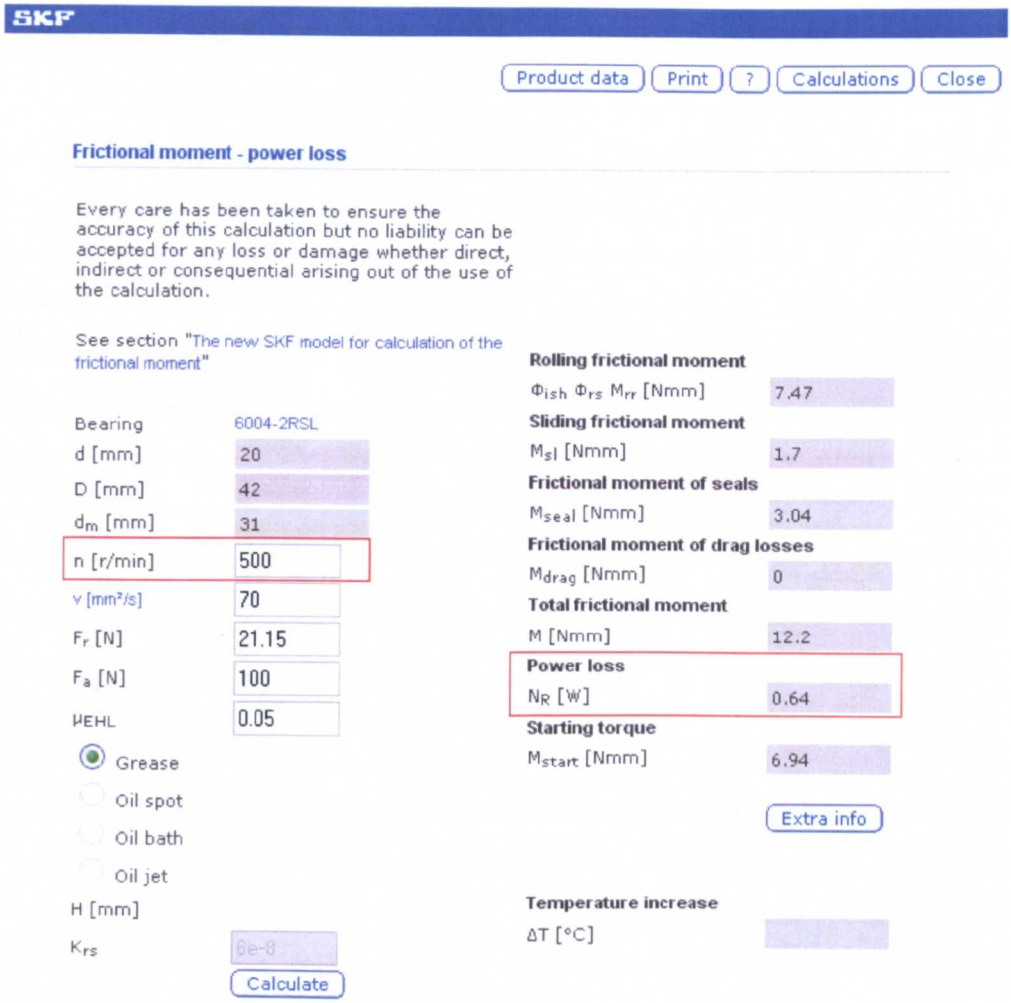

Figure 2: An example which data were input into the SKF Model to give the required bearing frictional loss at a specified speed.

w (rpm)	w (rad/s)	P loss (single bearing)	Total Bearing Loss (W)
0	0.00	0.00	0.00
50	5.24	0.05	0.09
100	10.47	0.10	0.20
150	15.71	0.16	0.31
200	20.94	0.22	0.43
250	26.18	0.28	0.56
300	31.42	0.35	0.69
350	36.65	0.41	0.83
400	41.89	0.49	0.97
450	47.12	0.56	1.12
500	52.36	0.64	1.28
550	57.60	0.72	1.44
585	61.26	0.78	1.56
600	62.83	0.81	1.61
650	68.07	0.90	1.79
700	73.30	0.99	1.97
750	78.54	1.08	2.16
800	83.78	1.18	2.36
850	89.01	1.28	2.56
900	94.25	1.38	2.76
950	99.48	1.48	2.96
1000	104.72	1.59	3.18
1050	109.96	1.70	3.40
1100	115.19	1.81	3.62
1140	119.38	1.90	3.80
1150	120.43	1.92	3.84
1200	125.66	2.04	4.08

Table 2: A tabulation of friction loss at various speeds

Appendix F Neodymium-Iron-Boron Permanent Magnets Datasheet

NEODYMIUM-IRON-BORON

Abbreviated Product Information Sheet

Typical Magnetic and Physical Characteristics

Material	Residual Induction Br				Coercivity Hcb		Intrinsic Coercivity Hcj		Maximum Energy Product BHmax				Temperature Coefficients		Curie Temp.	Max. Working Temp.
	kG		T		kOe	kA/m	kOe	kA/m	MGOe		KJ/m^3		α (Br)	β (iHc)	Tc	
Grade	Min.	Max.	Min.	Max.	Min.	Min.	Min.	Min.	Min.	Max.	Min.	Max.	%/°C	%/°C	°C	°C
N35	11.7	12.2	1.17	1.22	10.8	860	12	955	33	36	265	285	-0.12	-0.65	310	80
N38	12.2	12.6	1.22	1.26	11.2	890	12	955	36	40	285	320	-0.12	-0.65	310	80
N40	12.5	12.9	1.25	1.29	11.4	905	12	955	38	42	300	335	-0.12	-0.65	310	80
N42	12.8	13.2	1.28	1.32	11.5	915	12	955	39	44	310	350	-0.12	-0.65	310	80
N45	13.2	13.8	1.32	1.38	11.6	925	12	955	42	46	335	365	-0.12	-0.65	310	80
N48	13.7	14.3	1.37	1.43	11.6	925	11	955	45	50	360	400	-0.12	-0.65	310	70
N50	14.0	14.6	1.40	1.46	10.0	795	11	955	47	51	375	405	-0.12	-0.65	310	60
N35 M	11.7	12.2	1.17	1.22	10.8	860	14	1115	33	36	265	285	-0.12	-0.60	310-320	100
N38 M	12.2	12.6	1.22	1.26	11.2	890	14	1115	36	40	285	320	-0.12	-0.60	310-320	100
N40 M	12.5	12.9	1.25	1.29	11.5	915	14	1115	38	42	300	335	-0.12	-0.60	310-320	100
N42 M	12.8	13.2	1.28	1.33	11.8	835	14	1115	40	44	320	335	-0.12	-0.60	310-320	100
N45 M	13.2	13.8	1.32	1.38	12.2	970	14	1115	42	46	335	365	-0.12	-0.60	310-320	100
N48 M	13.6	14.3	1.36	1.43	12.8	1020	14	1115	45	49	360	390	-0.12	-0.60	310-320	100
N33 H	11.3	11.7	1.13	1.17	10.5	835	17	1355	31	35	245	280	-0.11	-0.58	320-330	120
N35 H	11.7	12.2	1.17	1.22	10.8	860	17	1355	33	37	265	295	-0.11	-0.58	320-330	120
N38 H	12.2	12.6	1.22	1.26	11.2	890	17	1355	36	40	285	320	-0.11	-0.58	320-330	120
N40 H	12.5	12.9	1.25	1.29	11.5	915	17	1355	38	42	300	335	-0.11	-0.58	320-330	120
N42 H	12.8	13.2	1.28	1.32	11.8	940	17	1355	40	44	320	350	-0.11	-0.58	320-330	120
N45 H	13.0	13.8	1.30	1.38	12.0	955	17	1355	42	46	335	365	-0.11	-0.58	320-330	120
N48 H	13.6	14.3	1.36	1.43	12.5	995	16	1275	45	49	360	390	-0.11	-0.58	320-330	110
N30 SH	10.8	11.4	1.08	1.14	10.0	795	20	1590	28	32	225	255	-0.11	-0.55	330-340	150
N33 SH	11.3	11.7	1.13	1.17	10.5	835	20	1590	31	35	245	280	-0.11	-0.55	330-340	150
N35 SH	11.7	12.2	1.17	1.22	10.8	860	20	1590	33	36	265	285	-0.11	-0.55	330-340	150
N38 SH	12.2	12.6	1.22	1.26	11.3	900	20	1590	36	40	285	320	-0.11	-0.55	330-340	150
N40 SH	12.5	12.9	1.25	1.29	11.6	925	20	1590	38	42	300	335	-0.11	-0.55	330-340	150
N42 SH	12.8	13.2	1.28	1.32	11.9	945	20	1590	40	44	320	350	-0.11	-0.55	330-340	150
N28 UH	10.2	10.8	1.02	1.08	9.4	750	25	1990	26	30	205	240	-0.11	-0.51	340-380	180
N30 UH	10.8	11.3	1.08	1.13	10.0	795	25	1990	28	32	225	255	-0.11	-0.51	340-380	180
N33 UH	11.3	11.7	1.13	1.17	10.5	835	25	1990	31	35	245	280	-0.11	-0.51	340-380	180
N35 UH	11.8	12.2	1.18	1.22	10.8	860	25	1990	33	36	265	285	-0.11	-0.51	340-380	180
N38 UH	12.2	12.6	1.22	1.26	11.3	900	25	1990	36	40	285	320	-0.11	-0.51	340-380	180
N40 UH	12.5	12.9	1.25	1.29	11.6	925	25	1990	38	42	300	335	-0.11	-0.51	340-380	180
N28 EH	10.4	10.9	1.04	1.09	9.8	780	30	2385	26	30	205	240	-0.11	-0.51	340-380	200
N30 EH	10.8	11.3	1.08	1.13	10.2	810	30	2385	28	32	225	255	-0.11	-0.51	340-380	200
N33 EH	11.2	11.7	1.12	1.17	10.5	835	30	2385	31	35	245	280	-0.11	-0.51	340-380	200
N35 EH	11.7	12.2	1.17	1.22	11.0	875	30	2385	33	36	265	285	-0.11	-0.51	340-380	200
N38 EH	12.2	12.6	1.22	1.26	11.3	900	30	2385	36	40	285	320	-0.11	-0.51	340-380	200

Notes:

- Properties listed here are typical and will vary depending upon size and shape of the magnet.
- Additional grades with enhanced high temperature performance are available.
- For additional information, please contact Arnold at the location below or speak with your local Arnold Salesperson.

ARNOLD® MAGNETIC TECHNOLOGIES

770 Linden Avenue, Rochester, NY 14625-2764 USA
Phone: (+1) 585-385-9010 • Toll free: 800-593-9127
Fax: (+1) 585-385-9017

Appendix G **Adhesives Datasheet**

Bondmaster E32
Two Part Epoxy Resin
Technical Information Sheet

Bondmaster
A National Adhesives Business
Woodside Road, Eastleigh
Hampshire SO50 4EX
Tel: 023 8061 9822
Fax: 023 8065 2270

Description:

Bondmaster E32 has remarkable resistance to both static and dynamic loading, and bonds to a wide variety of materials including metals, composites, ceramics and wood. E32 has been selected for many industrial assemblies where structural integrity is required. Applications extending back over 20 years confirm its excellent environmental durability. Accurately metered and mixed material can be applied direct to the workpiece by using E32 in the 'EDS' cartridge pack.

Physical Properties:	Part A - Resin	Part B - Hardener	Mixed
Colour	White	Black	Grey
Viscosity (mPa.s)	Soft Paste	Soft Paste	80,000 Soft Paste
Specific Gravity	1.38	1.06	1.22
Mix Ratio - By Weight	100:80	Gap Fill (on a vertical surface)	~1 mm
Mix Ratio - By Volume	1:1		

Generally the recommended service temperature range for this product is -55 to +80°C. However experience has shown that higher temperatures, of around 200°C, may be endured for short periods providing the adhesive is not unduly stressed.

Typical Performance:

Cure Speed	Usable Life	Handling Strength	Working Strength	Full Strength	
- at 23°C	2 hrs.	8 hrs.	24 hrs.	72 hrs.	The cure speed of 2 part epoxy resins is generally affected by the ambient temperature. A fall of 8°C will roughly double the cure time; a rise of 8°C will tend to halve it.
- at 60°C	—	—	30 mins.	1 hr.	
Lap Shear Strength EN1465:1995		26 (Steel)	On **Composites** this adhesive is capable of strengths similar to that achieved on steel but in most cases delamination on the composite will occur before this load is reached. On **Aluminium** & **Copper** alloys the modulus and thickness of the metal will define the ultimate bond strength achieved.		

Storage :

When stored in the original unopened containers at 5-25°C, the shelf life of this product is 24 months from the date of despatch from Bondmaster.

Handling:

Full information can be obtained from the Material Safety Data Sheet (M.S.D.S.). Users are reminded that all materials, whether innocuous or not, should be handled according to the principles of good industrial hygiene.

Directions for Use:

Thoroughly mix Resin (A) and Hardener(B)in the correct proportion. Do not mix more material than can be applied during the 'usable life' of the product. Surfaces should be clean, dry and grease free before applying the adhesive. Where maximum strength is required then the surfaces should be shot blasted, or lightly abraded, in the presence of Bondmaster SIP.
Ideally Bondmaster E32 should be cured at temperatures above 15°C. Lower temperatures result in lower strength.
The unmixed material should not be refrigerated.
Bondmaster E32 is approved to the Waters Byelaws Scheme as being suitable for contact with potable (drinking) water.

Technical Data Sheet

Hysol® 9492™

November 2007

PRODUCT DESCRIPTION

Hysol® 9492™ provides the following product characteristics:

Technology	Epoxy
Chemical Type (Resin)	Epoxy
Chemical Type (Hardener)	Modified Amine
Appearance (Resin)	White opaque paste
Appearance (Hardener)	Grey, opaque liquid
Appearance (Mixed)	White opaque paste
Components	Two part - Resin & Hardener
Mix Ratio, by volume - Resin : Hardener	2 : 1
Mix Ratio, by weight - Resin : Hardener	100 : 50
Cure	Room temperature cure after mixing
Application	Bonding
Specific Benefit	• Very low outgassing • High temperature resistance • Excellent solvent resistance

Hysol® 9492™ is a high temperature resistant, two component epoxy adhesive. It is a lower viscosity version of Hysol 9491 and retains the high performance features of this product. It is a general purpose adhesive that bonds and repairs a wide variety of materials. Fully cured Hysol® 9492™ bonds offer superior thermal shock resistance, mechanical, electrical and impact resistant properties.

TYPICAL PROPERTIES OF UNCURED MATERIAL

Resin Properties

Specific Gravity @ 25 °C	1.51
Viscosity, Brookfield - RVT, 25 °C, mPa·s (cP):	
Spindle 6, speed 5 rpm	50,000 to 120,000
Viscosity, DIN 54453, mPa·s (cP):	
Shear rate 10 s^{-1}	46,000
Shear rate 100 s^{-1}	34,000
Flash Point - See MSDS	

Hardener Properties

Specific Gravity @ 25 °C	1.52
Viscosity, Brookfield - RVT, 25 °C, mPa·s (cP):	
Spindle 7, speed 50 rpm	20,000 to 60,000
Viscosity, DIN 54453, mPa·s (cP):	
Shear rate 10 s^{-1}	27,000
Shear rate 100 s^{-1}	20,000
Flash Point - See MSDS	

Mixed Properties

Pot Life @ 22 °C, minutes:	
100 g mass	15

TYPICAL CURING PERFORMANCE

Fixture Time

Fixture time is defined as the time to develop a shear strength of 0.1 N/mm^2.

Fixture Time, mixed, @ 22 °C, minutes	75

Cure Speed vs. Time/Temperature

Hysol® 9492™ develops complete cure within 3 days at room temperature. Elevated temperatures may be used to accelerate the cure. The following graph indicates development of shear strength on mild steel (grit blasted) lapshears as a function of time and temperature tested according to ISO 4587.

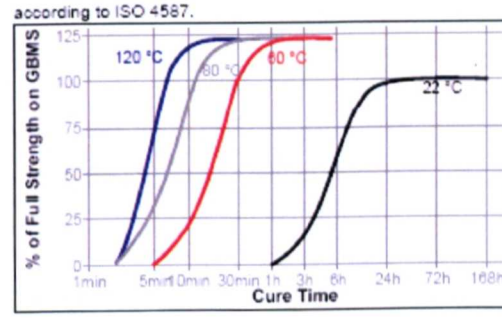

TYPICAL PROPERTIES OF CURED MATERIAL

Cured for 7 days @ 22 °C, 1.2 mm thick samples

Physical Properties

Coefficient of Thermal Expansion ISO 11359-2, K^{-1}:		
Temperature Range: -40 °C to 80 °C		63×10^{-6}
Coefficient of Thermal Conductivity, ISO 8302, W/(m·K)		0.3
Shore Hardness, ISO 868, Durometer D		80
Elongation , ISO 527-3,%		0.8
Tensile Strength, ISO 527-3	N/mm^2 (psi)	31 (4,500)
Tensile Modulus , ISO 527-3	N/mm^2 (psi)	6,700 (970,000)
Compressive Strength, ISO 604	N/mm^2 (psi)	80 (12,000)

Appendix H **Short Circuit Analysis**

Parameters

$P_{poles} := 10$ $Rph := 0.5$ $L_{phase} := 2.7 \cdot 10^{-3}$ resistance and inductance

$N_m := 0, 50 .. 1000$ $\omega_m(N_m) := N_m \cdot 2 \cdot \frac{\pi}{60}$ $\omega_e(N_m) := P_{poles} \cdot \omega_m(N_m)$ mechanical and electrical speeds

$kt := 2.6$ $bemf(N_m) := \omega_m(N_m) \cdot \frac{kt}{3}$

To calculate motor impedance, current and torques

$$Z(N_m) := \left| j \cdot \omega_e(N_m) \cdot L_{phase} + Rph \right| \qquad i_{ph}(N_m) := \frac{bemf(N_m)}{j \cdot \omega_e(N_m) \cdot L_{phase} + Rph}$$

$$Preal(N_m) := 3 \left(\left| i_{ph}(N_m) \right| \right)^2 \cdot Rph \qquad Torque(N_m) := \frac{Preal(N_m)}{\omega_m(N_m)}$$